Synthesis and Characterization of Ge nanocrystals prepared by different deposition techniques followed by various annealing processes and swift heavy ion irradiation

Thesis submitted for the degree of

Doctor of Philosophy

by

Nelamarri Srinivasa Rao

School of Physics
University of Hyderabad
Hyderabad – 500 046 India
December 2010

TABLE OF CONTENTS

Chapter – I

Introduction

1.1 Introduction

1.1.1 Introduction to nanoscale materials

Nanoscale materials can be defined as those whose characteristic length scale lies within the nanometric range, i.e in the range between one and several hundreds of nanometers (preferably between 0.1-100 nm). In last few years, nanomaterials have been the focus of research in the field of materials science, which is driven by the expectations concerning the application of nanomaterials as future generation of functional materials in the next few decades. A large amount of knowledge about the synthesis and properties of various nanoparticles and nanocomposites has been accumulated within a short period of recent past, with numerous new insights and techniques emerging with each passing day.

Nanocrystalline materials exhibit various shapes or forms, and possess unique chemical, physical or mechanical properties. Nanomaterials are experiencing a rapid development in recent years due to their existing and/or potential applications in a wide variety of technological areas such as electronics, catalysis, ceramics, magnetic data storage, structural components etc. To meet the technological demands in these areas, the size of the materials should be reduced to the nanometer scale. This size of the objects constitutes part of a larger length scale, varying from micron to nanometer as shown pictorially in Fig.1.1.

Although there is extensive research work going on in functional materials in general, the nanomaterials have attracted more attention from research community. Aircraft and spacecraft components require lightweight materials with high strength and stiffness, among other qualities. Nanocomposites with their superior thermal resistance are also attractive for general electronic gadgets at home and offices. Apart

from the pictorial representation of the size of the objects, materials categorization according to their size has been shown in table 1.

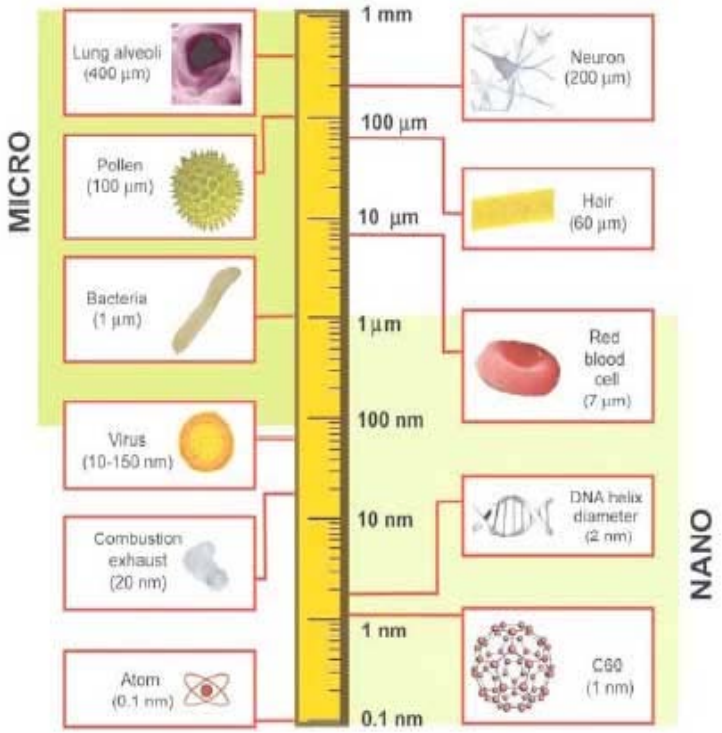

Fig.1.1 Pictorial view of micro to nano dimensional objects

Table.1 Materials categorization according to their size

	Size (approx.)	*Materials*
Nanocrystals and clusters (quantum dots)	1 – 10 nm (diam.)	Metals, semiconductors, magnetic materials
Other nanoparticles	1 – 100 nm (diam.)	Ceramic oxides
Nanowires	1 – 100 nm (diam.)	Metals, semiconductors, oxides, sulfides, nitrides
Nanotubes	1 – 100 nm (diam.)	Carbon, layered metal chalcogenides
Nanoporous solids	0.5 – 10 nm (pore diam.)	Zeolites, phosphates, etc.
2-D arrays (of nanoparticles)	Several nm^2 – μm^2	Metals, semiconductors, magnetic mater.
Surfaces and thin films	1 – 1000 nm (thickness)	A variety of materials
3-D structures (superlattices)	Several nm in the three dimensions	Metals, semiconductors, magnetic materials

1.1.2 Importance of nanomaterials:

Nanoparticles (quantum dots) of semiconductors are made small enough, so that quantum effects come into play limiting the energies at which electrons and holes (the absence of an electron) can exist in these nano-particles. As energy is related to wavelength, this means that the optical properties of the particle can be fine-tuned depending on its size. Thus, particles can be made to emit or absorb specific wavelengths of light, merely by controlling their size. Recently, quantum dots have found applications in composites, solar cells and fluorescent biological labels which use both the small particle size and tunable energy levels. The physical and chemical properties of substances can be significantly altered when they are exhibited on a nanometer-length scale. This happens because the surface to volume ratio enhances dramatically with reduction of particle size. This phenomenon opens up a completely new perspective for materials design that benefits from the introduction of not only particle size, but also particle morphology as new powerful parameter. Quantum confinement effects in such materials will play an essential role in optical absorption and emission processes in semiconductor nanocrystals since the energy band gap increases with decreasing diameter and electronic states become discrete with higher oscillator strength. In semiconductor nanocrystals the excitons are confined in all three spatial dimensions. As a result, they have different properties than those of bulk semiconductors. Besides, surface electronic states will also affect both electronic and optical properties of semiconductor nanocrystals due to large surface-to-volume ratios [1–3]. Such quantum confinement effects come into play when the structure dimensions are comparable with the wavelength of the charge carriers.

Nanoparticles may be synthesized from several routes and these may have different internal structures that would affect the properties of materials. Processing of nanoparticles into fully dense, bulk products or coatings, which retain the original nanometer scale grain size, is rather difficult to achieve in practice. Due to their high specific surface areas, nanoparticles exhibit a high reactivity and strong tendency towards agglomeration. Moreover, rapid grain growth is likely to occur during processing at high temperatures. As unique properties of nanocrystaline materials are derived from their fine grain size, it is of crucial importance to retain the microstructure at a nanometer scale during consolidation to form bulk materials. Due

to their very high surface-to-volume ratio, large fractions of surface atoms together with ultra-fine size and shape effects make nanoparticles exhibit distinctly different properties from the bulk. The evolution of nanoparticles from a vapor or liquid phase involves various fundamental steps like nucleation and growth.

1.1.2.1 Mechanism of nucleation:

Nucleation and growth depend on (i) liquid phase instability, which depends on driving force towards equilibrium and (ii) diffusion of atoms into clusters which is larger for higher temperatures. Nucleation can be either homogeneous, without the influence of foreign particles, or heterogeneous, with the influence of foreign particles. Generally, heterogeneous nucleation takes place much faster since the foreign particles act as a scaffold for the crystal to grow on, thus eliminating the necessity of creating a new surface and the incipient surface energy requirements.

Heterogeneous nucleation can take place by several methods. Some of the most typical are small inclusions, or cuts in the container where the nano-crystal is being grown on. This includes scratches on the sides and bottom of glassware. A common practice in crystal growth is to add a foreign substance, such as a string or a rock, to the solution, thereby providing a nucleation site for the project and thus speeding up the time it will take to grow a crystal.

1.1.2.2 Mechanisms of growth:

The interface between a crystal and its vapor can be molecularly sharp at temperatures well below the melting point. An ideal crystalline surface grows by the spreading of single layers, or equivalently, by the lateral advance of the growth steps bounding the layers. For perceptible growth rates, this mechanism requires a finite driving force (or degree of super cooling) in order to lower the nucleation barrier sufficiently for nucleation to occur by means of thermal fluctuations. In the theory of crystal growth from the melt, Burton and Cabrera have distinguished between two major mechanisms.

- **Non-uniform lateral growth**. The surface advances by the lateral motion of steps, which are one interplanar spacing in height. An element of surface undergoes no change and does not advance normal to itself except during the passage of a step, and then it advances by the step height. It is useful to consider the step as the transition between two adjacent regions of a surface which are parallel to each other and thus identical in configuration — displaced from each other by an integral number of lattice planes. Note here the distinct possibility of a step in a diffuse surface, even though the step height would be much smaller than the thickness of the diffuse surface.

- **Uniform normal growth**. Here, the surface advances normal to itself without the necessity of a stepwise growth mechanism. This means that in the presence of a sufficient thermodynamic driving force, every element of surface is capable of a continuous change contributing to the advancement of the interface. For a sharp or discontinuous surface, this continuous change may be more or less uniform over large areas each successive new layer. For a more diffuse surface, a continuous growth mechanism may require change over several successive layers simultaneously.

1.1.3. Classification of nanostructures:

The reduction in the spatial dimensions or confinement of particles leads to changes in different physical properties of the nanostructured systems. These nano dimensional materials have been classified into three different categories depending on their number of dimensions confined within nanometric range as (a) systems confined in three dimensions, (b) systems confined in two dimensions and (c) systems confined in one dimension. Systems confined in 3-D are called quantum dots (QD) or nanoparticles. A quantum dot (basically a zero dimensional object) is a semiconductor whose excitons are confined in all three spatial dimensions. In Quantum wires the electrons or holes will be confined in two spatial dimensions and allow free propagation in the third. Quantum wells, which confine electrons or holes in one dimension and allow free propagation in two dimensions. In small nanocrystals, the

electronic energy levels are not continuous as in the bulk but are discrete (finite density of states), because of the confinement of the electronic wave function to the physical dimensions of the particles. This phenomenon is called quantum confinement and therefore nanocrystals are also referred to as quantum dots. Those confined in two dimensions are called as nanorods or nanowires. The Density of states per unit volume and energy for a 3-D, 2-D, 1-D and 0-D objects has been shown in fig. 1.2 and table 2.

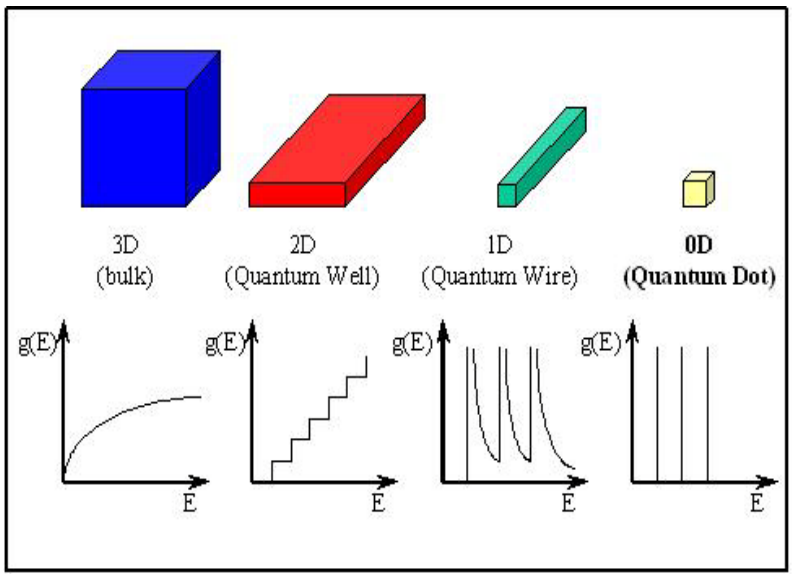

Fig. 1.2 Density of states per unit volume and energy for a 3-D, 2-D, 1-D and 0-D objects

Table .2 Density of states of bulk, quantum well, quantum wire, and quantum dot

Structure	Degree of Confinement	dN/dE
Bulk Material	0D (no confinement)	$\sqrt{E}$
Quantum Well	1D	1
Quantum Wire	2D	$\sqrt{1/E}$
Quantum Dot	3D	$\delta(E)$

1.1.4 Effects of nanometer length scale on various properties:

Here are some examples which show how the properties change as a result of nanoparticle dimensionality:

Chemical: When size of the Au nanoparticle is reduced to 2–10 nm, the catalytic activity of supported gold catalysts can be significantly enhanced [12]. Gadolinium acetylacetonate (GdAcAc), a potential anticancer agent for neutron capture therapy (NCT), has been entrapped in stable nanoparticles. The apparent water solubility of GdAcAc increased more than 2000-fold by such entrapment [4].

Mechanical: The hardness of silicon nanospheres (20–50 nm) has been measured to be four times greater than the expected value for bulk silicon (50 Gpa *cf*. 12 Gpa) [5].

Optical: Nanoparticles, with dimensions less than the wavelength of light (400–700 nm), appear transparent when well dispersed. Moreover, colour and luminescent properties can be significantly altered. For example, the optical properties of gold nanoparticle films have been fabricated with tailored optical responses, both in transmitted and reflected light, and to generate a series of materials with hybrid optical properties – i.e., possessing tunable opacity and reflectivity [6].

Electronic: The electronic structure of a nanocrystal critically depends on its size. For small particles, the electronic energy levels are not continuous (as in bulk materials), but discrete, due to the confinement of the electron wave function as a result of the physical dimensions of the individual nanoparticles. This confinement exhibits quantum size effects influencing properties such as electrical conductivity and magnetic susceptibility. Perhaps the most impressive example of the relationship between size and electronic effects is that of size induced transitions from metal to non-metal in nanocrystals such as Hg, Au, Ag, Pd, Ni and Cu [7].

Magnetic: magnetic properties of nanoparticles of transition metals such as Co, Ni show marked variations with size. In the nanometric domain, the coercivity (a measure of the strength of a magnetic field) of the particles tends to zero and nanocrystals behave as super paramagnets with no associated coercivity or retentivity.

This is somewhat analogous to the metal-insulator transition observed in nanocrystalline metals. The blocking temperature, which marks the onset of this super paramagnetism, also increases with the nanocrystal size. Further, the magnetic moment per atom is seen to increase as the size of a particle decreases [8]. As a particle becomes smaller, it can in principle, physically fit into, be assembled or positioned onto/into or pass through significantly smaller spaces. The implications of this feature are enormous in terms of the potential applications. Perhaps the greatest realized impact of this has been in the functional quality and performance properties of bulk material systems such as polymer nanocomposites and coatings (lighter, stronger, functionally smarter); ceramic composite materials (improved fracture toughness, wear resistance, greater biocompatibility, etc.); data storage and processing systems (greater capacity to store and process at reduced size); dispersions (for chemical mechanical polishing, personal care); sensors and instrumentation, drug delivery systems and enhanced activity in catalytic processes.

1.1.5 Nanomaterials at global market:

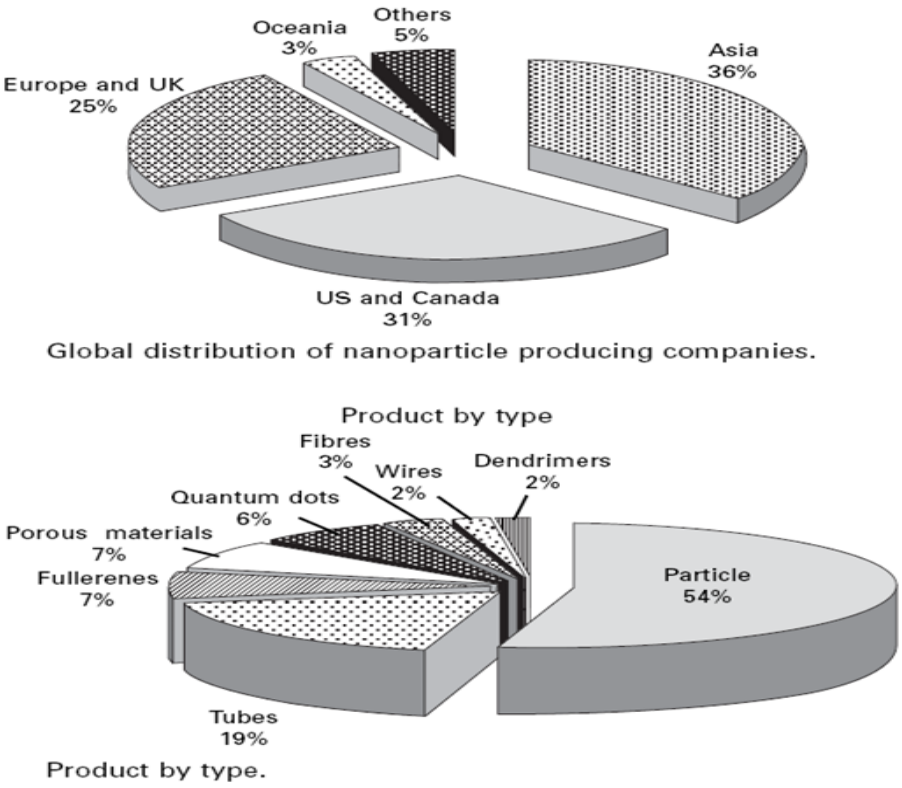

Fig. 1.2.1 Global distribution of nanoparticles producing companies and product by type

Major product groupings are primarily metal and metal oxide powders and carbon nanotubes with mixed metal oxides, non-oxides, semiconductors and silicates secondary. The reasons for this are largely historical as most of these materials are not 'new' materials and find themselves in existing applications. Global distribution of nanoparticles producing companies and product by type has been shown in fig 1.2.1.

1.1.6 Synthesis and production processes of nanostructures:

Nanostructures can be synthesized mainly via two approaches, bottom up or top down [9-12]. In bottom up approach, nanoparticles are buildup atom by atom i.e. atoms and molecules assemble to form the nanostructures with desired size. However the top down approach relies either on the division or removal of bulk materials or on the miniaturization of bulk fabrication processes to produce the desired structures with appropriate properties. The main techniques used in top-down approach are ball milling, lithography and ion beam machining. In bottom–up approach, atoms, molecules and even nanoparticles themselves can be used as the building blocks for the creation of complex nanostructures. By altering the size of the building blocks, controlling their surface and internal structure, and then controlling their organization and assembly, it is possible to engineer the properties of nanostructures. Bottom-up approaches can be classified into two categories (i) physical and (ii) chemical routes. Vapour phase deposition, sputtering, ion implantation, pulse laser deposition, molecular beam epitaxy etc are fundamental techniques used in physical routes. However sol-gel, citrate reduction process etc are used in chemical routes. Bottom-up processes effectively encompass chemical synthesis and/or the highly controlled deposition and growth of nanostructured materials. Chemical synthesis may be carried out in either the solid, liquid or gaseous state. Solid-state synthesis usually involves an iterative procedure of bringing solid state reaction precursors into intimate contact by mixing and grinding and then promoting atomic diffusion processes via heat treatment at high temperatures to form a reaction product. Vapour phase deposition can be used to fabricate thin films, multilayers, nanotubes or nanometre-sized particles. The vapour phase deposition techniques can be classified into physical and chemical vapour depositions. Physical vapour deposition (PVD) involves the conversion of solid material into vaopur phase by physical processes, which is subsequently cooled and re-deposited on the substrate. In this thesis, the physical processes of co-

sputtering and ion implantation have been used for synthesizing different nanostructures. It is important to have basic idea of nucleation and growth of nanoparticles, during thin film growth which is discussed in the next section.

1.2 Materials of interest

Semiconductor nanocrystals are useful in both basic and applied research point of view. The structural, optical and electronic properties of low dimensional, indirect band gap materials have been investigated extensively over the past few years. During the last decade, semiconductor and metal nanocrystals embedded in an insulating matrix have attracted a large number of researchers due to their potential applications in optoelectronic and memory devices [13, 14].

When the crystallite size of these semiconductors is smaller than the exciton Bohr radius and carriers can be three-dimensionally confined, the properties of semiconductor nanostructures embedded in dielectrics may be engineered and monitored to suit required applications [15, 16]. Semiconductor nanostructures of indirect band gap materials such as silicon (Si) and germanium (Ge) have been studied widely because of their potential applications in optoelectronics and nanophotonics [17, 18]. Although porous Si is expected to be the most promising Si-based light emitting material, Ge nanocrystals (nc-Ge) embedded in Silica have their own advantages. It was reported, based on comparison of Si and Ge effective masses and energy differences between the indirect gaps, that it should be easier to modify the electronic structure around the band gap of Ge [19]. The exciton Bohr radius of bulk Ge is much larger than that of bulk Si, which implies that the quantum confinement effect of Ge nanostructures will be more prominent. Several techniques are being used to fabricate Ge nanocrystals, such as RF co-sputtering [20], DC sputtering [21], ion implantation [22], evaporation–condensation [23], electron beam evaporation [24], chemical vapour deposition [25] and pulsed laser deposition [26]. But the new versatile synthesis methods like atom beam sputtering, microwave annealing and swift heavy ion irradiation etc provide better control on the nanocrystal formations.

The main motivation of this thesis is to synthesize semiconductor nanocrystals by various methods. Extensive experimental work in this direction has been carried out for complete understanding. Ge nanocrystals embedded in SiO_2 matrix have been synthesized by various techniques like ABS, RF sputtering and ion implantation. We have used different post deposition methods like normal furnace annealing, RTA, microwave annealing and swift heavy ion irradiation to synthesize Ge nanocrystals. Advantages and limitations of all these methods are discussed in detail. The comparative study has been made with the results obtained by various techniques. Results, mechanism of crystallization and formation of nanocrystals in these samples under swift heavy ion irradiation are explained with the help of thermal spike theory. Crystallization and growth of nanocrystals in these films have also been discussed. Characterization techniques have been chosen in such a way to complement each other and to confirm the results obtained.

1.3 Importance and applications of Germanium

Nowadays, germanium is still a comparatively rare element, however, one with great technological importance: its fields of application range from semi-conductor industries and optical and telecommunication industries to applications in the biomedical field. Here we discuss the important technological and commercial uses, and their relevance and impact on man and the environment.

Germanium is a very brittle element of grayish-white appearance and submetallic lustre. It has atomic number 32, relative atomic mass 72.61, specific gravity 5.323, melting point 937.4^0C (1210.6 K) and boiling point $2{,}830^0$C (3103.2 K). Germanium has a refractive index of 4.0. Having the highest refractive index of any infrared bulk transmitting substrate materials and low dispersion properties across a wide range of temperatures avoids chromatic aberration in many applications. This combination of high refractive index and low dispersion also means that imaging by a single Ge lens with low f-number is easily achievable. Its surface hardness and robust mechanical strength also aid applications where ruggedness is a requirement. It is also non-hygroscopic, non-toxic and possesses good thermal conductivity.

Uses of germanium in the semiconductor industry: The first semiconductor of industrial importance was produced from germanium in the early 1940s. Over the last decades, germanium has regained a lot of interest as a semiconductor material for optoelectronic and electronic applications. The recent reintroduction of Ge in new transistor generations is due to the fact that Ge semiconductors can be operated at higher processor speeds than Si chips [27].

Ge crystals for infrared optics: Due to the transparency of germanium in the range from 1.85 to 15 µm, crystals made from germanium are widely used as lens or window material in infrared optical systems which are particularly useful and important for night vision instrumentation. Although germanium is practically transparent between 2 and 15 µm, it exhibits free carrier absorption which can be minimised, by doping the crystals n-type with a concentration between $4x10^{13}$ and $1x\ 10^{15}$ cm^{-3}. This way, the absorption coefficient for monocrystalline Ge is less than 0.02 cm^{-1} at room temperature. Optical-grade germanium must also be optically uniform and isotropic, i.e., the homogeneity of the refractive index must be very high and the birefringence must be minimized. High transparency and optical uniformity require a stringent reduction of grain boundaries. Furthermore, to ensure low birefringence, the residual stresses in the crystal, being a result of the production process of monocrystalline Ge, must be minimized. This is achieved by the use of appropriate heat shields and/or after heaters above the melt surface to minimize the radial thermal gradients [28].

Ge crystals for X-ray detectors: A much specialized, yet highly important field of application for germanium is its use as detector material for spectroscopy in nuclear physics. In contrast to silicon detectors which cannot be thicker than a few millimetres, germanium can have a thickness of the sensitive layer of centimeters, and therefore can be used as a total absorption detector for gamma rays up to few MeV. These detectors are also called High-Purity or Hyperpure Germanium detectors (HPGe). HPGe detectors can be allowed to warm up to room temperature when not in use [29].

Ge use for (UV/vis) fibre optics: The currently most important use of germanium is for the production of UV/vis optical fibres for the telecommunication industry. Due to its relatively similar atomic and ionic radii, glasses can be formed from SiO_2 and GeO_2 in any ratio. GeO_2 (refractive index 1.7 versus 1.46 for SiO_2) is thus used to modify the refractive index of the fibre [30]. In order that an optical fibre has low optical losses, it must consist of a core of lower refractive index that guides the light, and a cladding of higher refractive index that prevents leakage of the light to the surrounding medium. This can be achieved with either step- or continuous-gradient fibres.

Ge use as catalyst in polymerizations: The second major use of germanium is as catalyst or co-catalyst in the production of polyesters (e.g., polyethylene terephthalate) and synthetic textile fibers [31]. The advantage of the more expensive germanium over other catalysts (based on, e.g., titanium or antimony) is that the final product is colorless which is essential for some applications.

1.4 Structure of thesis

In the (present) first chapter, introduction to ion-solid interaction, materials of interest and the characterization techniques have been elaborated. The motivation of present thesis has also been discussed. The second chapter gives the details of the facilities used to carry out the experimental part of the work. The ABS, RF magnetron sputtering and ion implantation methods, high and low energy irradiation facilities, and characterization facilities used in this work namely, XRD [32, 33], Raman spectroscopy, FTIR, RBS [34, 35], AFM and TEM have been explained in detail.

Third chapter gives the results of furnace annealing and RTA effects on Ge+SiO_2 composite films prepared by ABS. We have also studied the effects of Ge composition on structural properties. On the other hand, these as-deposited samples have been irradiated with different fluencies and energies. Effects of SHI on these samples are studied in detail. The advantages of high energy irradiation are highlighted.

Fourth chapter describes the microwave annealing and swift heavy ion irradiation of Ge+SiO_2 composite films. Samples were annealed at different temperatures to see the variation of annealing temperature effect on crystallite size. As-deposited samples have been studied before and after heavy ion irradiation. It is observed that crystallite size increases with annealing temperature. Effects of Ge composition on structural properties are also studied. Raman results also confirm the presence of nanocrystals. RBS has been carried out to find the composition and thickness of composite films. AFM has also been used to see the surface morphology of these samples.

The fifth chapter describes the irradiation of Ge implanted SiO_2/Si samples. Ge ions were implanted into SiO_2 matrix at room temperature and subsequently irradiated with Ag ions by varying the fluence. On the other hand, Ge ions were implanted into Si at 573K and subsequently irradiated with 100 MeV Au ions at fixed fluence. Pristine and irradiated samples are studied using XRD, Raman spectroscopy. Surface morphology of the samples is studied by AFM. SHI induced effects and results are discussed in detail on the basis of thermal spike model.

Final chapter gives the overall conclusion of the thesis; comparison of all the results and the outlook for the possibilities of future works to be carried out along this direction.

1.5 Ion solid interactions

When a swift charged particle enters a material, it will interact with the electrons and nuclei in this material and begins to lose energy as it penetrates into the medium. The interaction can be generally thought of as collisions between the projectile and either the atomic electron or the nucleus. Knowledge of energy loss of these charged particles in matter is important to understand the mechanisms of material modification induced by the ions. Depending on the projectile velocity, the energy loss may be classified as:

(i) nuclear energy loss
(ii) electronic energy loss
(iii) photon emission and
(iv) nuclear reactions.

Among these, the electronic energy loss is most prominent one in slowing down the high velocity charged particles. At high energies (1 MeV/nucleon), where the velocity of ion is comparable with the Bohr velocity of orbital electrons, the ion interacts with the electrons of the target atoms as a result of which the target atoms undergo electronic excitation/ionization (inelastic collisions). Since the mass of the ion is much higher than the mass of the electron, the initial direction of the ion in the solid remains almost unchanged. The ion stopping power as a function of ion velocity has been shown in fig 1.3.1.

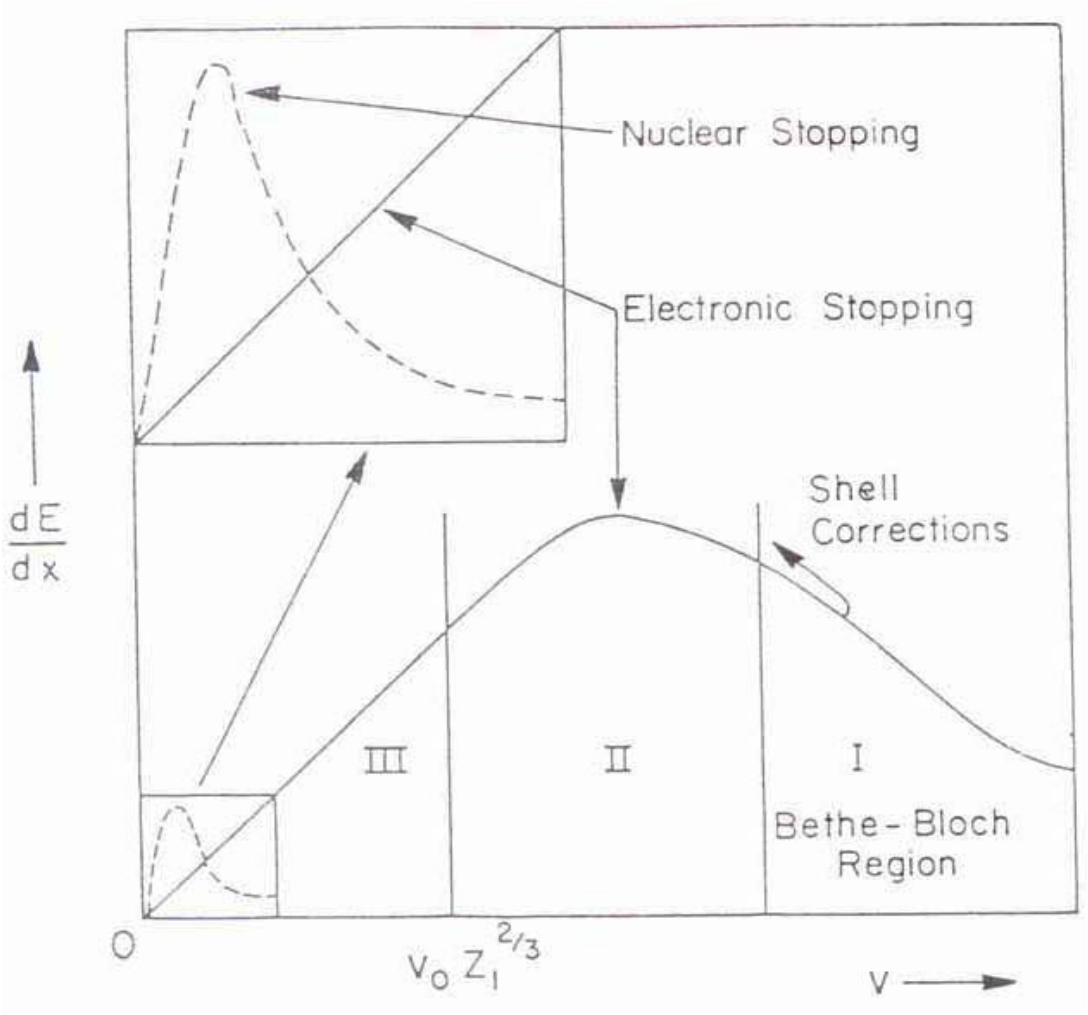

Figure.1.3.1: Stopping power as a function of ion velocity

Influence of nuclear reactions depends on the projectile energy, the desired accuracy and on the projectile-target combination considered [36]. The interest of present thesis limits to nuclear and electronic energy loss regimes of the incident ions.

1.5.1 Nuclear energy loss

The nuclear stopping is a sum of the energy losses of a moving ion due to its elastic collisions with the target atom/nuclei as a whole. The energy that an ion loses is converted to heat in the slowing down material as the atoms spread the kinetic energy in series of collisions, namely in collision cascades resulting in displacement of target atoms. A common feature for all ions is that the nuclear stopping of the medium as a function of ion energy has a maximum at a relatively low energy (of the order of 1 keV/amu) and thereafter, the nuclear stopping of the medium decreases as the energy of the ion increases. This means that the nuclear stopping is important only for low ion velocities. Analytically, the nuclear energy loss of an ion can be integrated if one knows the statistics of energy transfer in atomic collisions [37]. Nuclear energy loss dominates for heavy ions over most of their path, and for light ions at low energies. Along the path of the ion the nuclear energy loss has the following important regimes: displacement and replacement collisions. At the entrance of the surface, the ions displace atoms from the lattice site and the number of displaced atoms can be calculated using Kinchin-Pease formula,

$$\nu = \frac{k\,E_N}{2\,E_d} \qquad \text{(First approximation)} \qquad (1.1)$$

where E_N is the energy deposited in elastic nuclear collisions, E_d is displacement energy (typically ~15 to 25 eV for Si), k independent of energy for given material (~0.8). Ions having enough energy after displacing the atoms from the lattice site proceed along the direction until it come to rest. The displaced region of the solid is full of vacancy rich zone.

In the replacement collisions regime the incident ion displaces host atom, but does not have enough energy to escape the vacancy. This happens close to the end of range of the incident ions (very slow ions). Energetic projectiles displace many target atoms, which in turn displace many more resulting in a Cascade. Primary damage results in vacancy rich region (depleted zone) is surrounded by interstitial defects. Large energy deposition: Secondary cascades (“sub-cascades”), Collective interactions; dense cascades; disordered zone. Shown schematically in Fig.1.3.2

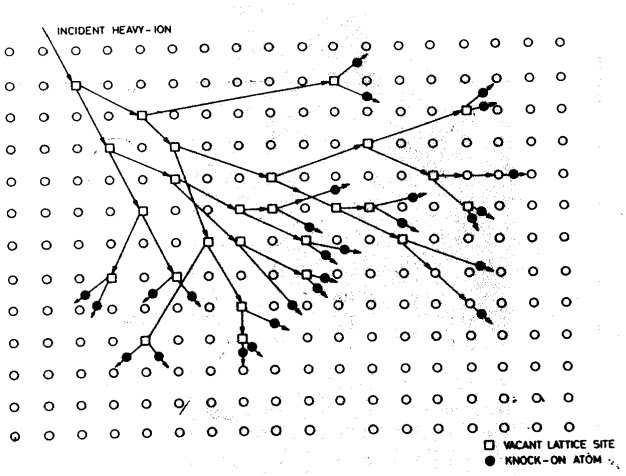

Fig.1.3.2: Schematic of nuclear energy loss

1.5.2. Electronic energy loss

According to the velocity dependence, the electronic energy loss may be visualized having three distinct regions: first, high velocity region where energy loss decreases with increasing velocity; second, medium velocity region having maxima in the energy loss and third, the low velocity region where the energy loss decreases with the decreasing velocity. Here we consider the high velocity regime and discuss in detail. There are two basic approaches used to evaluate a charged particle's electronic energy loss. These are the Bohr approach, which is dependent on the impact parameter between the particle's trajectory and the target nucleus, and the Bethe approach which depends on momentum transfer from the particle to the target electrons [38]. Bethe's approach was necessary since quantum mechanics prohibits a particle with a **well defined momentum** having a **spatially localized** position. Hence Bohr's concept of an impact parameter (defined in 1913, before quantum mechanics was developed) could not be directly upgraded to wave mechanics. There was no quantized solution to close collisions if one attempted to use the Bohr impact parameter concepts. The classical Bohr approach considers a heavy charged particle of charge, Z_1e, moving at a velocity, v, passing near a light electron of charge, e, and mass m, at an impact parameter, b. The transverse momentum impulse, Δp, to the light electron is [39, 40]:

$$\Delta p = \int_{-\infty}^{\infty} e\overline{E}(t)\,dt \quad = \frac{2Z_1e^2}{bv} \tag{1.2}$$

where E is the transverse electrical field. The energy transferred is then:

$$\Delta E = \frac{(\Delta p)^2}{2m} = \frac{2Z_1^2 e^4}{mv^2}\left(\frac{1}{b^2}\right) \qquad (1.3)$$

This expression assumes that the electron does not move much relative to the impact parameter, b. To obtain the stopping power, S, this transferred energy must be integrated over all possible impact parameters, b. assuming the target is made of atoms of atomic number, Z_2. The energy loss per target atom is :

$$S = 2\pi Z_2 \int \Delta E(b) \qquad (1.4)$$

$$= 4\pi Z_2 \frac{Z_1^2 e^4}{mv^2} \int_0^\infty \frac{1}{b^2} b db \qquad (1.5)$$

The integral of this expression diverges as $b \rightarrow 0$, so it is necessary to argue a minimum impact parameter, b_{min}. If the electron mass is assumed to be very much smaller than the mass of the incident particle, the electron will recoil strongly for very small impact parameters. Noting that the maximum energy transfer is for a head-on collision, we may use Rutherford two-particle elastic scattering to estimate the closest distance of approach for a head-on collision. This gives a minimum distance of

$$b_{\min} = \frac{Z_1 e^2}{mv^2} \qquad (1.6)$$

The integral also becomes undefined for $b_{max} \rightarrow \infty$. This can be made tractable by noting that, for distant collisions, if the interaction is long compared to the orbiting frequency of an electron, the collision will become adiabatic and no energy will be transferred. This suggests a cutoff when the collision time becomes longer than the orbital frequency, $b_{max} \sim v/\omega$, where ω is the orbital frequency.

Inserting these values for b_{min} and b_{max}, the energy loss becomes:

$$\frac{dE}{dx} = 4\pi Z_2 \frac{Z_1^2 e^4}{mv^2} \ln\left(\frac{mv^3}{Z_1 e^2 \omega}\right) \qquad (1.7)$$

The relativistic form of this equation is obtained by equating the particle's energy, $E = \gamma M_1 c^2$, where $\gamma = 1/(1-\beta^2)^{1/2}$ and $\beta = v/c$. This expands $b_{max} \sim \gamma v/\omega$, and $b_{min} \sim Z_1 e^2/\gamma m v^2$ and the integral become [38]

$$\frac{dE}{dx} = \frac{4\pi Z_2 e^4}{mv^2} Z_1^2 \ln\left(\frac{\gamma^2 mv^3}{Z_1 e^2 \omega}\right) \qquad (1.8)$$

Bohr used this expression to form the basis of his evaluation of the energy loss of a heavy particle to a medium of harmonically bound electrons.

Let us estimate the energy loss (-dE/dx) suffered by an incident charged particle when it interacts with a free and initially stationary electron. Referring to the collision cylinder of radius b as the impact parameter and its length to be the small distance traveled dx as shown in Fig.1.4,

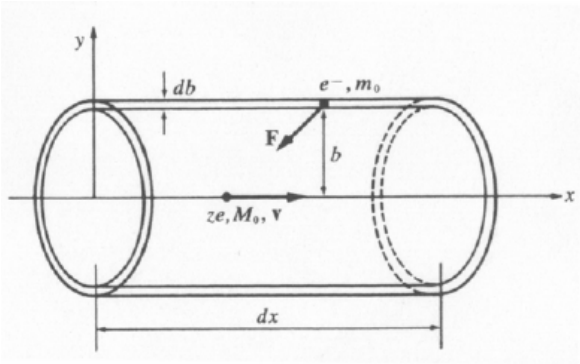

Fig.1.4: Interaction of heavy charged particle of mass M_o and a free electron of mass m_e the impact parameter b is indicated

The net momentum transferred to the electrons as the particle moves from one end of the cylinder to the other end is essentially entirely directed in the perpendicular direction (F_x changes sign so the net momentum along the horizontal direction vanishes) along the negative y-axis. So,

$$\int dt F_x(t) \approx 0 \qquad (1.9)$$

$$p_e = \int F_y(t)\, dt$$

$$= \int \frac{Z_1 e^2}{x^2 + b^2} \frac{b}{(x^2 + b^2)^{1/2}} \frac{dx}{v}$$

$$\cong \int \frac{Z_1 e^2 b}{v} \int_{-\infty}^{\infty} \frac{dx}{(x^2 + b^2)^{3/2}} = \frac{2Z_1 e^2}{vb}$$

The kinetic energy transferred to the electron is therefore

$$p_e^2 = \frac{2\left(Z_1 e^2\right)^2}{m_e b^2 v^2} \qquad (1.10)$$

If we assume this is equal to the energy loss of the charged particle, then multiplying by nZ_2 (2π b dbdx), the number of electrons in the collision cylinder, we obtain

$$-\frac{dE}{dx} = \int_{b_{\min}}^{b_{\max}} nZ_2 2\pi b db \frac{2}{m_e}\left(\frac{Z_1 e^2}{vb}\right)^2$$

$$= \frac{4\pi\left(Z_1 e^2\right)^2 nZ_2}{m_e v}\ln\left(\frac{b_{\max}}{b_{\min}}\right) \qquad (1.11)$$

where b_{max} and b_{min} are the maximum and minimum impact parameters and depend on the physical description of the problem. In reality the atomic electrons are of course not free electrons, so the charged particle must transfer at least an amount of energy equal to the first excited state of the atom. If we consider a time interval of energy transfer to be $\Delta t \approx b/v$, then $(\Delta t)_{max} \sim 1/\nu$, where $h\upsilon = \langle I \rangle$ is the mean ionization potential. Then,

$$b_{\max} = \frac{h\nu}{\langle I \rangle}$$

An empirical expression for I normally used is $I \approx kZ_2$, with k ~ 19 eV for H and ~ 10 eV for Pb. We estimate b_{min} by using the uncertainty principle to say that the electron position cannot be specified more precisely than its de Broglie wavelength in the relative coordinate system of the electron and the charged particle. Since electron momentum in the relative coordinate system is $m_e v$, we estimate,

$$b_{\min} = \frac{h}{m_e v} \qquad (1.12)$$

Combining these two estimates we obtain

$$-\frac{dE}{dx} = \frac{4\pi Z_1{}^2 e^4 nZ_2}{m_e v}\ln\left(\frac{2m_e v^2}{\langle I \rangle}\right) \qquad (1.13)$$

In the above eq. (1.13) a factor of 2 has been included in the argument of the logarithm; this is to make the formula agree with the result of quantum mechanical calculation which was first carried out by Bethe using the Born approximation. Basically this factor of 2 comes from the consideration of equality in stopping contributions due to close and distant collisions.

Eq.(1.13) describes the energy loss due to particle collisions in the nonrelativistic regime. One can include relativistic effects by replacing the logarithm by,

$$\ln\left(\frac{2m_e v^2}{\langle I\rangle}\right)-\ln\left(1-\frac{v^2}{c^2}\right)-\frac{v^2}{c^2}$$

Eq.(1.13) is a relatively simple expression, yet one can gain much insight into the factors that govern the energy loss of a charged particle by collisions with the atomic electrons. We can see why one can usually neglect the contributions due to direct collisions with nuclei at these high velocities. In a collision with a nucleus the stopping power would increase by a factor Z, because of the charge of the target with which the incident charged particle is colliding, and decrease by a factor of $m_e/M(Z)$, where M(Z) is the mass of the atomic nucleus. The decrease is a result of the larger mass of the recoiling target. Since Z is always less than 102 whereas M(Z) is at least a factor 2 x 10^3 greater than m_e, the mass factor always dominates over the charge factor. Another useful observation is that (1.13) is independent of the mass of the incident charged particle. This means that nonrelativistic electrons and protons of the same velocity would lose energy at the same rate.

The original Bethe-Bloch relativistic stopping formula, S may be written as:

$$S=\frac{4\pi e^4 Z_2}{m_e v}Z_1^{\,2}\left[\ln\left(\frac{2m_e v^2}{\langle I\rangle}\right)-\ln\left(1-\beta^2\right)-\beta^2+\Psi(Z_1)\right] \qquad (1.14)$$

where <I> is the mean ionization potential per electron.

Using further approximations, Fano [41] described a relativistic version of Bethe-Bloch energy loss formula where two additional corrective terms are included, the shell correction term C/Z_2 and the density effect correction term $\delta/2$ and it is given as,

$$S=\frac{4\pi\, e^4 Z_2}{m_e v}Z_1^{\,2}\left[\ln\left(\frac{2m_e v^2}{\bar{I}}\right)-\ln\left(1-\beta^2\right)-\beta^2-\frac{C}{Z_2}-\frac{\delta}{2}\right] \qquad (1.15)$$

which is simplified using the definitions,

$$r_o\equiv e^2\big/mc \qquad \text{(the Bohr electron radius)}$$

$$f(\beta)\equiv\ln\left[\frac{2mc^2\beta^2}{1-\beta^2}\right]-\beta^2 \qquad (1.16)$$

$$S=\frac{4\pi r_0^{\,2} m_e c^2 Z_2}{\beta^2}Z_1^{\,2}\left[f(\beta)-\ln<I>-\frac{C}{Z_2}-\frac{\delta}{2}\right] \qquad (1.17)$$

There have been many corrections proposed to improve on Fano's theoretical approximations. Traditionally, this is done by expanding this equation in powers of Z_1, which can be used to add additional corrections to the ion and target interaction.

1.6 Swift Heavy Ion induced effects on materials:

Swift heavy ion beams play an important role in the field of research in material science. In ion beam modification of materials, the energetic ions interact with the solid through interatomic potential. These interactions are the basis of the development of expressions for ion range and ion damage in solids. When an energetic ion passes through a solid, it undergoes collisions with the stationary target atoms, which deflect the ion from its initial direction. The ion also collides with electrons in the solid and loses energy in these collisions. The major changes in its flight direction are due to the ion's collision with individual lattice atoms. Ion beam effects on the materials depend on the ion energy, fluence and ion species. Low energy ions up to a few hundred keV available from ion implanters have been used in semiconductors and modification of surface of materials. High energy ions (energy > 1 MeV/nucleon) whose velocity is comparable to Bohr velocity are known as swift heavy ions (SHI). These ions have been used for synthesis, modification, characterization and engineering of materials with their unique feature of electronic energy deposition.

In the present thesis, the focus has been to study the swift heavy ion induced effects and modifications in composite nanostructured thin films. Ion beams have proven to be the versatile tool for engineering the properties of materials. Materials modification with ion beams [42-53] has emerged with interesting technological aspects with fundamental understanding of ion matter interaction and has resulted in significant progress in development and miniaturization of devices.

SHI irradiation of materials can result in sputtering, mixing, amorphization, epitaxial crystallization, plastic deformation, nanophase & nanostructure formation etc. Techniques employing ion beams span a large range of ions, their energy and fluence. These can be combined with various material preparation techniques permitting

additional processing degrees of freedom for producing new class of materials. The passage of energetic ions into matter results a loss of their energy [54-57] mainly via collision either with nuclei or with electrons. In low energy regime, the velocity of ions is relatively small as compared with Bohr velocity of orbital electrons. Hence the incoming ions hit the target nuclei elastically and the energy is directly transferred to target nuclei resulting in displacement of target atoms. This energy loss is termed as nuclear energy loss (Se) which is dominant at lower energies and is helpful for studying in phenomenon of mixing in materials and ion implantation in semiconductor industries. When high energy positively charged ions pass through the matter, they deposit a large amount of energy within the confined volume. Due to huge amount of electronic energy deposition, the material goes into molten state for short duration of time (~few pico-seconds), creating a cylindrical track along their path. The material modification takes place in this cylindrical track. This leads to the formation of nanocrystals.

1.6.1 Formation of Ion Tracks in Materials by Swift Heavy Ions

Bombardment of solids with swift heavy ions leads to formation of damage zones in these materials. Due to large amount of electronic energy deposition within a confined volume, the materials go into the molten state transiently in a narrow cylindrical region. The materials transformed into disordered state along the ion trajectory called latent track (damage zone created along the paths of swift heavy ions). The formation of track is the result of high local electronic energy deposition along the ion path and hence conditions for track formation in different materials are different because of their different properties. Basically, two different mechanisms named as Coulomb explosion and thermal spike [58] can be considered for track formation.

1.6.2 Coulomb Explosion Model

In the Coulomb explosion model, it is assumed that an energetic ion creates a cylindrical region of highly ionized matter along its path. Here, the energy of the ion beam is assumed to lie in the electronic stopping regime and the ion carries an effective charge because it loses those electrons with orbital velocity smaller than the velocity of the ion in the medium. As it passes through the target, the projectile

ionizes atoms along its trajectory. These target ions then recoil due to repulsion from projectile ion as well as their mutual Coulomb repulsion. These amounts of repulsive energy are substantial compared to the binding energy per atom of the solid. It is important to note that the track develops an intense charge due to the large amount of energy that is deposited on a very local scale by the impinging ion. Due to the strongly localized charge, relatively narrow regions of charged ions inside the track experience an intense accelerating force from the resulting electric field. This is sufficient to induce significant motion of the target ions on time scales of 10^{-15} s or shorter, long before thermal motion due to phonons can occur. The Coulomb explosion is significant only if the charge neutralization time exceeds 10^{-14}s [59]. This phenomenon leads to the localized destruction of the lattice.

1.6.3 Thermal Spike Model: In this model the energy is first deposited onto the electrons and subsequently transferred to the atomic subsystems via electron-phonon coupling. The presence of free electrons tends to screen the projectile charge to avoid any coulomb explosion. The heat diffusion in the electron and lattice subsystems is described by two coupled differential equations governing the energy diffusion on the electron and atomic subsystems and their exchange via the electron-phonon coupling. The projectile ion gives its energy to the electron gas, and then energy is transferred to the lattice via electron-phonon coupling in the hot electron system during the characteristic time 10^{-13}s [60]. The electron-phonon coupling stands for the ability of electrons to transfer their energy to the lattice. The interaction between electrons and phonons originate from the phenomenon of local polarization. It is assumed that when the temperature exceeds the melting point of the crystal, then a molten state is formed in a localized zone of few nanometers. The rapid thermal quenching of the hot region induces an amorphous track left along the ion path in a short span of time ($t \sim 10^{-11}$s), with the diameter of typically few nm. The narrow cylinder of material that was heated to high temperature transiently and then rapidly quenched by thermal conduction, results in modifying/disordering in the track core. It has been observed experimentally [61, 62] that only continuous tracks are formed if the energy deposition along the ion path exceeds a threshold value of electronic energy loss (Seth), which depends on the target material. The evolution of the track morphology depends on stopping power, proposed by Toulemonde, et al. [61] and later confirmed

by Meftah et al [62]. Toulemonde et al. [61] has described the necessary and sufficient conditions for formation of ion tracks in different materials.

1.6.4 Nano-engineering by Swift Heavy Ions

As swift heavy ions pass through the materials, they create nanosized ion tracks along their paths due to large electronic energy deposition and the material present within the ion tracks goes into molten state for a short duration of time of the order of few pico-seconds. The energy of excited electrons is transferred to lattice system through electron phonon coupling and then this energy is transferred to surroundings via normal conduction process. So, drastic modifications in the materials occur after swift heavy ion irradiation. The size of these cylindrical ion tracks depends on the energy of projectile ions and the type of material (mainly insulators). Thus choice of projectile ion and type of target material allows one to create the nanotracks of desired size. Ion fluence (Φ), i.e. the total number of ions incident on the material per unit area is another significant parameter for modification of the materials due to SHI irradiation.

Since during passage of SHI in the materials, nanodimensional tracks are created and the material present within the cylindrical track goes into the molten state, the properties of materials present within the track are modified. The material modification can be controlled by ion beam parameters. SHI irradiation of materials can result in crystallization, amorphization, growth and dissolution, and expansion of materials along the ion track [63-66]. In this thesis, the focus has been given on SHI irradiation effects on Ge+SiO_2 composite films.

1.7. Characterization techniques

The following techniques have been used for characterization of composite films. The characterizations are,

(i) **X-R**ay **D**iffraction (XRD)

(ii) Raman Spectroscopy

(iii) **R**utherford **B**ackscattering **S**pectrometry (RBS)

(iv) **A**tomic **F**orce **M**icroscopy (AFM)

(v) **F**ourier **T**ransform **I**nfrared **S**pectroscopy (FTIR)

(vi) **T**ransmission **E**lectron **M**icroscopy (TEM)

These techniques have been used in the present thesis extensively and hence the basics are discussed in detail in this section.

1.7.1 X-ray diffraction

Diffraction of X-rays or neutrons from polycrystalline samples is one of the most important, powerful and widely used analytical techniques available to materials scientists. The present thesis deals with semiconductor composite films and the discussions are confined to XRD. It is useful in getting the information about the crystallinity of the material, lattice parameter, phase present and grain (particles size) size. The variation of peak position with sample orientation can be utilized to deduce the information regarding the internal strain of the sample.

1.7.2 Raman spectroscopy

Raman scattering is an inelastic scattering of photons from an atom or a molecule. Raman spectroscopy is a spectroscopic technique used in condensed matter physics and chemistry to study vibrational, rotational, and other low-frequency modes in a system. It depends on the inelastic scattering, or Raman scattering of monochromatic light, usually from a laser in the visible, near-infrared or near-ultraviolet range of electromagnetic spectra. The shift in energy in Raman Effect gives information about the phonon modes in the systems, which are the quantized modes of vibration occurring in a rigid crystal lattice. Each peak in the spectrum corresponds to one or more vibrational modes of the nanostructures. Raman spectroscopy is commonly used in chemistry, since vibrational information is very specific for the chemical bonds in molecules.

In our study, Ge and silica composite films have been characterized by Raman spectroscopy. Raman spectra of the samples show a shift in the peak position and an asymmetrical broadening on the lower frequency side when compared with the spectrum of the bulk sample. The significance of shift with respect to bulk value has been discussed and related to nanocrystals. The results are explained in respective chapters.

1.7.3 Fourier Transform Infrared Spectroscopy:

An FTIR Spectrometer is an instrument which acquires broadband NIR to FIR spectra. Unlike a dispersive instrument, i.e. grating monochromator or spectrograph, an FTIR Spectrometer collects all wavelengths simultaneously and it is based on the fundamental principles of molecular spectroscopy. The basic principle behind molecular spectroscopy is that specific molecules absorb light energy at specific wavelengths, known as their resonance frequencies. An FTIR spectrometer works by taking a small quantity of sample, which is subjected to an infrared light source, scanned from 4000 cm^{-1} to around 600 cm^{-1}. FTIR has been employed to study the nc-Ge embedded SiO_2 films and results are discussed in the third chapter.

1.7.4 Rutherford backscattering spectrometry (RBS)

Rutherford Backscattering Spectrometry (RBS) is a widely used nuclear method for the near surface layer analysis of solids. A target is bombarded with lighter ions at an energy in the MeV-range (typically 0.5–4 MeV), and the energy of the backscattered projectiles is recorded with an energy sensitive detector, typically a solid state detector. RBS allows the quantitative determination of the composition of a material and depth profiling of individual elements. RBS is quantitative without the need for reference samples, nondestructive, has a good depth resolution of the order of several nm, and a very good sensitivity for heavy elements of the order of parts-per-million (ppm). The analyzed depth is typically about 2 μm for incident He-ions and about 20 μm for incident protons. Using RBS, it is possible to determine atomic mass and elemental concentrations versus depth below the surface. RBS is ideally suited for determining the concentration of trace elements heavier than the major constituents of the substrate. Its sensitivity for light masses, and for the makeup of samples well

below the surface, is poor. In this thesis, RBS has been used to estimate the Ge composition and composite film thickness.

1.7.5 Atomic force microscopy

The Atomic Force Microscope was developed to overcome a basic drawback with STM-that it can only image conducting or semiconducting surfaces. The AFM, however, has the advantage of imaging almost any type of surface, including polymers, ceramics, composites, glass, and biological samples. AFM measures three dimensional images of surfaces and is very helpful for visualizing surface topography. Nanometer sized dimensions of surface features are measurable with the AFM. We have studied the surface morphology and roughness of the samples using this technique.

1.7.6 Transmission electron microscopy

The transmission electron microscope (TEM) operates on the same basic principles as the light microscope but uses electrons instead of light. What you can see with a light microscope is limited by the wavelength of light. TEMs use electrons as “light source” and their much lower wavelength make it possible to get a resolution a thousand times better than with a light microscope. We have used TEM to characterize the nanocrystals in our samples.

1.8 Conclusions

This chapter discussed basics involved and provided the motivation for the work carried out and explained the advantages of semiconductor nanocrystals. Brief discussion about characterization techniques used in this thesis has been given. But the complete principle and system details have been discussed in (next) second chapter. We conclude this chapter by giving a brief overview of the rest of the thesis: The next chapter describes the experimental facilities utilized while the third chapter discusses the synthesis of Ge nanocrystals by ABS followed by RTA, furnace annealing and irradiation. In fourth chapter we demonstrate the use of microwaves and ions in preparation of Ge nanocrystals, while in fifth chapter SHI effects on Ge implanted SiO_2 / Si films have been presented. Finally we conclude the overall work in the last chapter and project possible future outlook.

1.9 References

1. S. Takeoka, Phys. Rev. B 58 (1998) 12
2. L. Brus, Appl. Phys. A 53 (1991) 465
3. Y.X. Jie, Y.N. Xiong, A.T.S. Wee, C.H.A. Huan, W. Ji, Appl. Phys. Lett. 77 (2000) 3926
4. M. O. Oyewumi, and R. J. Mumper, Drug Dev Ind Pharm. 28(3): (2002) 317
5. W Gerbericha, et al. J. of the Mechanics and Phy. of Solids 51 (2003) 979.
6. T Ung, L Liz-Marza, and P Mulvaney, Physicochemical and Engineering Aspects 202 (2002) 119.
7. H N Aiyer, V Vijayakrishnan, G N Subanna, and C N R Rao, Surf. Sci. 313 (1994) 392.
8. C N R Rao, G U Kulkarni, P J Thomas, and P P Edwards, Chem. Eur. J. 8, No. 1 (2002) pp 28–35.
9. Daniel L. Feldheim and Colby A Foss, Handbook on “Metal Nanoparticles: Synthesis, Characterization and Applications “CRC Press 2002, ISBN 0824706048.
10. G. Cao, Handbook on “Nanostructures & Nanomaterials: Synthesis, Properties & Applications” Imperial College Press, ISBN 1860944809.

11. R. W. Kelsall, M. Geoghegan and I. W. Hamely, Handbook on “Nanoscale Science and Technology” John Wiley & Sons, ISBN 0470850868.
12. M. B. Cortie and E. van der Lingen, Mat. Forum 26 (2002) 1.
13. H. Takagi, H. Ogawa, Y. Yamazaki, A. Ishizaki, and T. Nakagiri, Appl. Phys. Lett. 56 (1990) 2379.
14. S. Tiwari, F. Rana, H. Hanafi, E. F. Crabbe, and K. Chan, Appl. Phys. Lett. 68 (1996) 1377.
15. K S Zhuravlev, A M Gilinsky and A Yu Kobitsky, Appl. Phys. Lett. 73 (1998) 2962
16. S H Choi and R G Elliman, Appl. Phys. Lett. 75 (1999) 968
17. L T Canham, Appl. Phys. Lett. 57 (1990) 1046
18. L. Pavesi, L. Dal Negro, C. Mazzoleni, G. Franzo, and F. Priolo, Nature (London) 408 (2000) 440.
19. Y Maeda, Phys. Rev. B 5 (1995) 1658.
20. P Caldelas, A G Rolo, A Chahboun, S Foss, S Levichev, T G Finstad, M J M Gomes, O Conde, J. of Nano. and Nanotechnology 8 (2008) 572
21. M Zacharias, P M Fauchet. J Non-Cryst Solids 227–230 (1998)1058.
22. S N M Mestanza, E Rodriguez and N C Frateschi, Nanotechnology 17 (2006) 4548
23. A Stella, P Tognini, C E Bottani, P Milani, P Cheyssac, R Kofman, Thin Solid Films 318 (1998) 100
24. Q Wan , C L Lin, N L Zhang, W L Liu, G Yang, T H Wang, Appl Phys Lett 82 (2003) 3162
25. Z He, J Xu, W Li, K Chen, D Feng, J Non-Cryst Solids 266–269 (2000) 1025.
26. Y Zhu, P P Ong, J Phys Condens Matter 13 (2001) 4075.
27. E E Haller, Mater Sci Semicond Process 9 (2006) 408–422.
28. B DepuydtB, A Theuwis , I Romandi , Mater Sci Semicond Process 9 (2006) 437–443.
29. Vetter K, Ann Rev Nucl Part Sci 57 (2007) 363–404
30. H M J M Van Ass, P Geittner, R G Gossink , D Kuppers, P J W Severin, Philips Tech Rev 36 (1976) 182–189
31. Karl-Heinz Wolf, Bernhard Küster, Heinz Herlinger, Chung-Ji Tschang,

Eckhard Schollmeyer, Die Angewandte Makromolekulare Chemie, 68, Issue 1, (1978) pages 23–37

32. B. D. Cullity, Elements of X-ray Diffraction, 2nd. Ed., Addison-Wesley, (1978)
33. L. C. Feldman and J. W. Mayer; Fundamentals of Surface and Thin Film Analysis; North-Holland. New York, 1986
34. W.K.Chu, J.W.Mayer, and M.A. Nicolet, Backscattering Spectrometry, Academic Press, New York, 1978
35. Introduction to solid state physics- C. Kittel
36. P Sigmund, Energy loss of charged particles in solids, Monograph No. 73-20 (1973).
37. J F Ziegler, J P Biersack and U Littmark, The Stopping and Range of Ions in Solids, Vol.1 of "The Stopping and Ranges of Ions in Matter", Pergamon Press, New York (1985).
38. J F Ziegler, J. Appl. Phys / Rev. Appl. Phys. 85 (1999) 1249.
39. P Sigmund, Radiation Damage Processes in Materials, C. duPuy, ed., Noordhoff, Leiden, 3 (1975).
40. M Inokuti, Rev. Mod. Phys. 43 (1971) 297.
41. U Fano, Ann. Rev. Nucl. Sci. 13 (1963) 67.
42. S. Klaumunzer, M. D. Hou and G. Schumacher, Phys. Rev. Lett. 57 (1986) 850.
43. S. Klaumunzer, Nucl. Instr. and Meth. B 215 (2004) 345.
44. S. Klaumunzer, Nucl. Instr. and Meth. B 244 (2006) 1.
45. A. Gutzmann and S. Klaumunzer, Nucl. Instr. and Meth. B 127/128 (1997) 12.
46. S. Roorda, T. van Dillen, A. Polman, C. Graf, A. van Blaaderen and B. J. Kooi, Adv. Mater. 16 (2004) 235.
47. J. J. Penninkhof, C. Graf, T. V. Dillen, A. M. Vredenberg, A. V. Blaaderen and A. Polman, Adv. Mater. 17 (2005) 1484.
48. C. D. Orleans, J. P. Stoquert, C. Estournes, C. Cerruti, J. J. Grob, J. L. Guille, F. Haas, D. Muller and M. R. Plouet, Phys. Rev. B 67 (2003) 220101.
49. A. Oliver, J. A. R. Esqueda, J. C. Cheang-Wong, C. E. R. Velázquez, A. C. Sosa, L. R. Fernández, J. A. Seman, and C. Nogue, Phys. Rev. B 74 (2006) 45425.

50. Y. K. Mishra, F. Singh, D. K. Avasthi, J. C. Pivin, D. Malinovska and E. Pippel, Appl. Phys. Lett. 91 (2007) 63103.
51. T. Van Dillen, E. Snoeks, W. Fukarek, C. M. Van Kats, K. P. Velikov, A. V. Blaaderen and A. Polman, Nucl. Instr. and Meth. B 175-177 (2001) 350.
52. E. Snoeks, A. V. Blaaderen, T. van Dillen, C. M. van Kats, K. P. Velikov, M. L. Brongersma and A. Polman, Nucl. Instr. and Meth. B 178 (2001) 62.
53. Y. K. Mishra, D. K. Avasthi, P. K. Kulriya, F. Singh, D. Kabiraj, A. Tripathi, J. C. Pivin, I. S. Bayer and A. Biswas, Appl. Phys. Lett. 90 (2007) 73110.
54. J. F. Ziegler and Z. P. Biersack, U. Littmark, „The Stopping and Range of Ions in Solid, (Pergamon, New York, 1985). [www.srim.org]
55. E. Valentin, H. Bernas, C. Ricolleau, F. Creuzet, Phys. Rev. Lett. 86 (2001) 99.
56. A. Meftah, F. Brisard, M. Costantini, E. Dooryhee, M. Hage-Ali, M. Hervieu, J. P. Stoquert, F. Studer and M. Toulemonde, Phys. Rev. B 49 (1994) 12457.
57. M. Toulemonde, J. M. Costantini, Ch. Dufour, A. Meftah, E. Paumier, and F. Studer, Nucl. Instr. and Meth. B 116 (1996) 37.
58. M. Toulemonde, Ch. Dufour and E. Paumier, Phys. Rev. B 46 (1992) 14362.
59. R. E. Johnson and W. L. Brown, Nucl. Instr. and Meth. B 198 (1982) 103.
60. A. I. Ryazanov and A. E. Volker Phys. Rev. B 51(1995-II) 12107.
61. M. Toulemonde, J. M. Costantini, Ch. Dufour, A Meftah, E. Paumier and F. Studer, Nucl. Instr. and Meth. B 116 (1996) 37.
62. A. Meftah, F. Studer and M. Toulemonde, et al., Phys. Rev. B. 48 (1993) 920.
63. S. Klaumunzer, Nucl. Instr. and Meth. B 225 (2004) 136.
64. S. Roorda, T. V. Dillen, A. Polman, C. Graf, A. V. Blaaderen and B. J. Kooi, Adv. Mater. 16 (2004) 235.
65. S. K. Srivastva, D. K. Avasthi and E. Pippel, Nanotechnology 17(2006) 2518.
66. S. Klaumunzer, Nucl. Instr. and Meth. B 244 (2006) 1.

Chapter – II

Experimental Details

2.1 Experimental facilities

Several experimental facilities have been used in our work for sample preparation and subsequent treatment. Particularly, Atom Beam sputtering (ABS) method was used extensively to grow Ge+SiO_2 composite films at **I**nter **U**niversity **A**ccelerator **C**entre (IUAC), New Delhi. We have also used our in-house RF Magnetron sputtering (RF sputtering) for deposition of composite films. High and low energy irradiation works have been carried out using the accelerator facilities at IUAC, New Delhi and ion implantation at **I**ndira **G**andhi **C**entre for **A**tomic **R**esearch (IGCAR), Kalpakkam respectively. The glancing incidence X-ray diffraction (GIXRD) and Fourier transform infrared spectroscopy (FTIR) characterizations have been carried out at IUAC, New Delhi**. R**utherford **B**ackscattering **S**pectrometry (RBS) studies were carried at IGCAR Kalpakkam, Orsay France and NCCCM, Hyderabad. **A**tomic **F**orce **M**icroscopy (AFM) measurements were carried out in-house. Raman spectroscopy measurements have been carried out in-house as well as at IUAC, New Delhi. The **T**ransmission **E**lectron **M**icroscopy (TEM) studies have been carried out at HCU. The detailed description of the facilities and their usage is given in this chapter.

2.2 Samples growth

Synthesis of Germanium – Silica composite Thin Films by Co-sputtering:

Sputtering is a process whereby atoms are ejected from a solid target material due to bombardment of the target by energetic particles [1-3]. Sputtering can be classified into three types (i) nuclear sputtering, (ii) electronic sputtering and (iii) ion sputtering. Nuclear sputtering is totally governed by kinetics, which is based on the exchange of momentum between energetic ions and atoms in the material. Atoms of the lattice are pushed into new position giving rise to surface migration of atoms and to surface damage. At energy exceeding the heat of sublimation [1] of the target material, the

dislodging of atoms and ejection into the gas phase begin to play an important role. The silent features of sputtering process in thin film preparation technique are (i) high uniformity of thickness of the deposited film, (ii) good adhesion to the substrate, (iii) better reproducibility of films, (iv) ability to deposit the films with the stochiometry of the original target composition, and (v) better film thickness control [1, 2]. Thus the major advantage of sputtering is that high melting point materials like ceramics, insulators and refractory metals, which are hard to deposit by evaporation techniques, can easily be deposited using sputtering. Furthermore, sputtering techniques range from a simple DC glow discharge sputtering, which is limited to the sputtering of conductive targets, to RF sputtering where any target regardless of its conductivity can be sputtered, to a more sophisticated ion beam sputtering in which very controlled deposition of material is possible. The sputtering yield, the most important parameter for characterizing the sputtering process, is defined as the number of atoms ejected from the target surface per incident ion. The sputtering yield depends on the bombarded materials, its structure and composition, the mass and energy of the incident ion, and also the experimental geometry [1]. It has been observed that emission of elections and ions in above-mentioned techniques can cause damage in many targets materials due to charging effects. Hence sputtering of insulating materials using DC glow discharge sputtering techniques is difficult because of space charge effect. In this thesis, a new type of sputtering setup called atom beam sputtering [4-7] was used in which energetic neutral Ar atoms have been delivered for sputtering of target materials.

2.2.1 Atom Beam Co-sputtering The atom beam sputtering setup is shown in Fig. 2.1 and the geometry of source is shown in Fig. 2.2. In this system, the source generates neutral argon atoms to sputter the target material. We have used argon atoms instead of ion source in other conventional sputtering systems. It is very useful to use the neutral beam produced by atom source since it does not produce any charging effect, which allows the sputtering of insulating materials without any space charge problem. The geometry of the source (Fig. 2.2) has been made in such a way that initially ions are produced by passing the Ar gas through a high potential (~1.5keV) and they are neutralized before extraction from the source. Thus a neutral beam of Ar atoms with about ~1.5keV of energy impinge at the surface of sputtering

target. This system has been used to produce semiconductor nanocrystals embedded in SiO_2 matrix. The atom source is mounted at an angle of 45° facing towards the sputtering target.

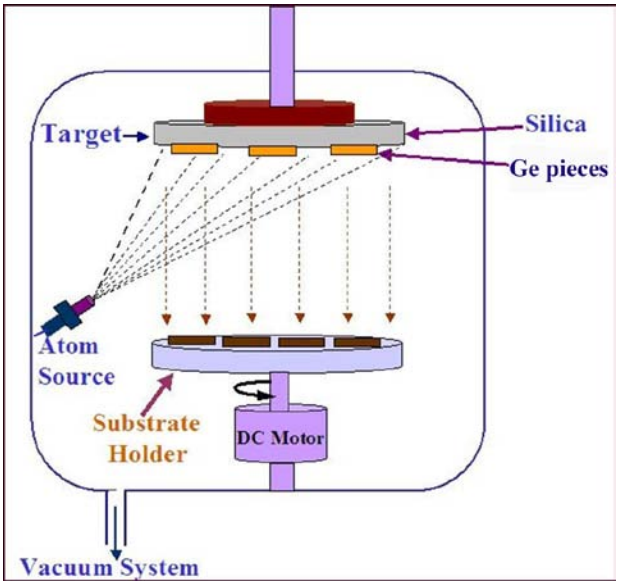

Fig.2.1: Schematic set-up of ABS

The substrate holder is mounted on a DC motor for better uniformity of the film [4]. The distance between substrate and the sputtering target can also be adjusted as per requirement. The gap between source and target is maintained in such a way that the beam covers approximately 50 mm in diameter at the target. The source delivers a maximum current density of ~30 $\mu A/cm^2$ on the target. The energy can be varied from 0.5 to 2.0 keV as per requirement. This source produces a directed beam of neutral atoms and substrate damage due to beam charge is minimal and can be neglected.

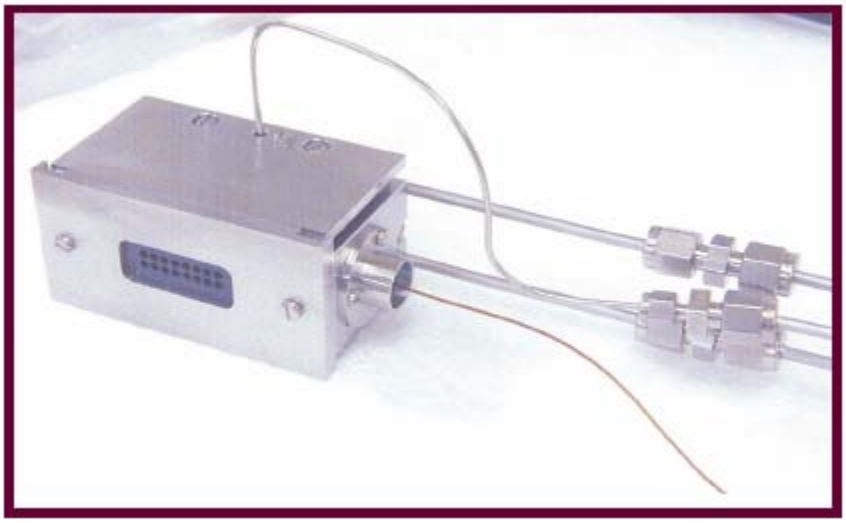

FIG. 2.2: FAB110 Saddle field source.

The energetic atoms or fast atoms originate as energetic ions within the plasma. The plasma chamber permits to ionize the Ar gas resulting in formation of diluted gas containing free electrons and positive Ar^+ ions. The arrangement of the electrostatic field close to the output grid, allows the acceleration of the ions. The source is able to operate at pressure approaching two orders of magnitude lower (10^{-3} mbar with pumping speed of 150 lit/sec) then those normally associated with cold cathode sources. The operation of the source is dependent on the plasma current and voltage. The plasma voltage is determined by the gas flow, which is related to the discharge impedance within the source. The current and the gas flow are the key parameters that require adjustment to operate the source at constant output. The source requires a current regulated DC power supply with an open circuit voltage of 2.5 kV. During the experiment, the source requires a vacuum pumping system speed of 150 to 250 lit/s, a clean cooling water supply (flow rate ~0.5 lit/min) in the temperature range 15-20^0C and a gas supply of pure Argon, controlled by a regulator with flow adjustments by fine control needle valve.

Since, the aim was to synthesize Ge nanoparticles embedded in insulating matrices; therefore we have co-sputtered both the Ge and Silica matrix simultaneously. The schematic of the sputter target can be seen in Fig. 2.3. Spherical silica with diameter around 75 mm was taken and it was partly covered by Ge chips each with area around 1cm^2 depending upon the requirement. The chips were symmetrically glued at the

surface of silica for getting the uniform sputtering from the composite target. At the same time the substrate is rotated by a DC motor for better uniformity.

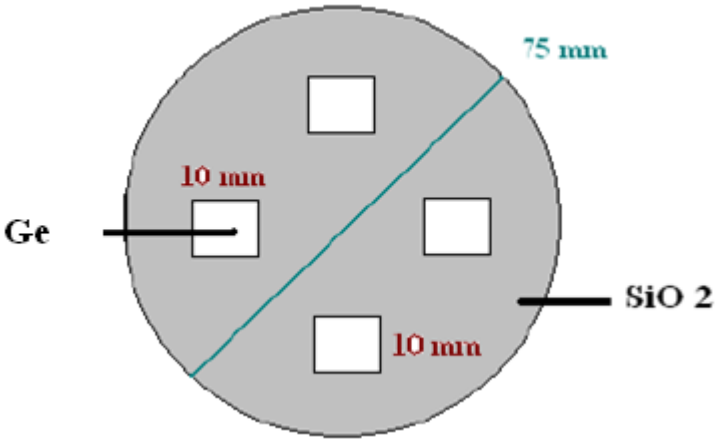

FIG. 2.3: Schematic of co-sputtering target.

The samples were prepared by the fast ABS method where small pieces of high purity Ge were placed on a SiO_2 target and co-sputtered by an Argon atom source. Thin films of Ge and SiO_2 nanocomposites with various Ge compositions were prepared by co-sputtering of Ge and silica using 1.5 keV Ar atoms. The Ar atom source was mounted at an angle of 45^0 facing the sputtering target inside a vacuum chamber, as shown in Fig. 2.1.

The Ge nanoparticles embedded in insulating matrices with varying semiconductor fraction have been synthesized using atom beam co-sputtering technique [8-9]. In this thesis, effects of Ge concentration and annealing temperature have been studied and discussed in detail. The main advantages of atom beam sputtering setup are discussed in the next chapter.

2.2.2 Radio Frequency Magnetron Co-sputtering (RF Sputtering):

The composite thin films described in this work were prepared using a process called radio frequency (r.f.) magnetron sputter deposition. In this process, the substrates onto which the films are to be deposited are placed into a vacuum chamber, also known as the sputter chamber, and all of the gas is pumped out of the chamber until sufficient vacuum (10^{-5} torr or less) is obtained. Argon (Ar) gas is then passed into the chamber.

Within the chamber there may be one or multiple sputter guns onto which targets are placed. The targets are disks made out of the materials that are to be deposited, or their metal counterparts that will be oxidized during the deposition. A r.f. power supply is connected to the sputter gun and when the power is turned on an electric field is generated between the target and the substrate. The current is alternating, so free electrons are alternately attracted and repelled from the target. As the electrons move between the target and the substrate they collide with argon atoms and knock off more electrons. This process continues exponentially until a cloud of argon ions (Ar^+) and electrons, called plasma, is generated. The argon ions bombard the surface of the target and physically knock off pieces which are ejected and deposited onto the substrate (Figure 2.4). The same process would occur at the surface of the substrate however magnets placed within the sputter gun confine the plasma to a region immediately above the target. In this way, small pieces of target material are sputtered onto the substrate and over a period of time, a thin film is deposited.

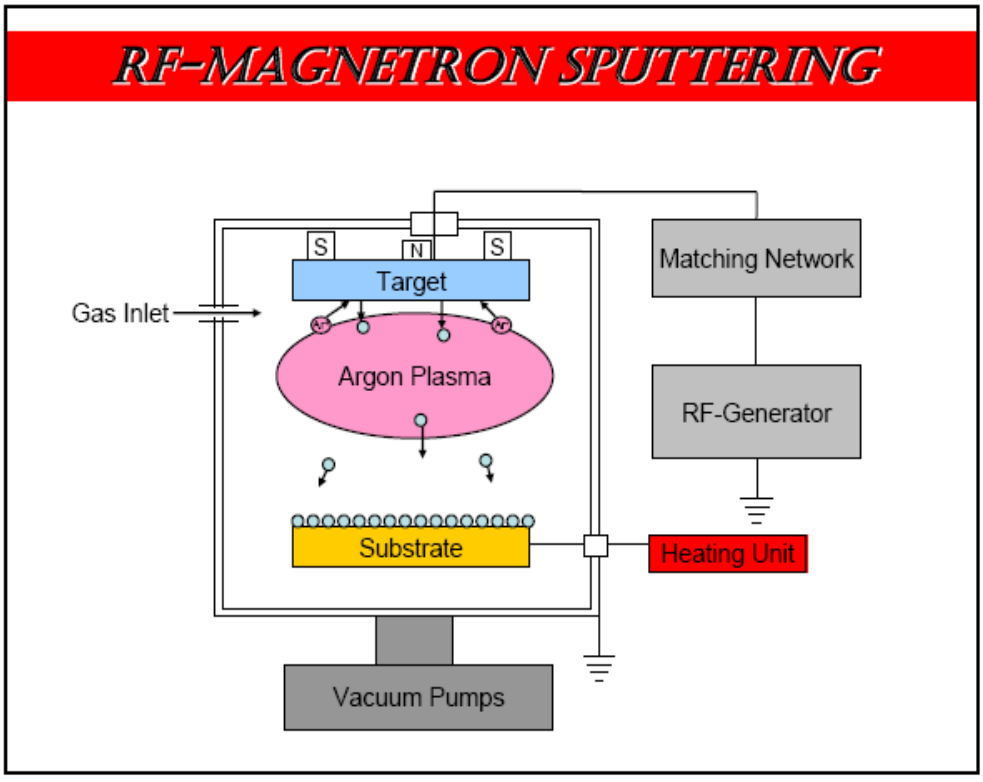

Fig.2.4: RF magnetron sputtering system block diagram

The glow discharge is initiated by applying power to the target in a controlled gas atmosphere, and consists of a partially ionized gas of ions, electrons, and neutral species. The ejected material diffuses until it reaches and nucleates on the substrate. The duration of this process controls the thin film thickness.

The use of a radio frequency generator is essential to maintain the discharge and to avoid charge build-up when sputtering insulating materials such as PZT. The presence of a matching network between the rf generator and the target is necessary in order to optimize the power dissipation in the discharge. Magnets are used to enhance the sputtering rate, by increasing the ionizing effect of electrons magnetically trapped in the vicinity of the target (magnetron sputtering). Their use provides the advantage of trapping not only electrons, but also charged species at the target, so that they do not hit the substrate, with an improvement of the film quality.

The composite thin films were prepared by the RF-magnetron sputtering technique with a composite target of Ge of purity 99.999% (2 inch in diameter) and several SiO_2 pieces (the purity is 99.999%) chips were attached on the top of Ge target. The films were deposited on (1 0 0) oriented p-type Si substrates. Prior to deposition, the substrates were cleaned in alchohol and acetone. Eventually, substrates were rinsed with a large amount of de-ionized water, dried in hot air and immediately placed into the chamber. In situ Ar pre-sputtering of the target was performed in order to clean it and remove any Ge oxide on the surface of these Ge pieces. After vacuum pumping, the co-sputtering was performed with an Ar pressure of 20 SCCM (standard cubic centimeter per minute). The gas was introduced inside the chamber through a mass flow controller. The sputtering was performed at RF power of 30 W. The vacuum before the sputtering was 5×10^{-6} and during the sputtering was 3×10^{-3} torr.

2.3 Accelerator facilities

2.3.1 Pelletron accelerator at IUAC

The swift heavy ion irradiation work has been done at IUAC, New Delhi [10]. High voltage up to 15 million volts is generated in the centre portion known as terminal. The Pelletron accelerator can be operated upto 15 MV of terminal potential and can produce dc as well as pulsed beam of a variety of elements. The IUAC pelletron accelerator is basically a heavy ion Tandem type of electrostatic accelerator. A **S**ource of **N**egative **I**ons by **C**esium **S**puttering (SNICS) is used to produce negative ions with a pre-acceleration of 400keV within the ions source which are injected into strong electrical field inside the accelerator tank filled with SF6 insulating gas. At the center of the tank a terminal shell is maintained at required high voltage ($\leq$15MV). This terminal voltage builds-up based on the principle of Van-de Graff accelerator. A chain of metal pellets are used instead of belt for carrying the charge to the terminal and hence the name Pelletron. The negative ions on traversing through the accelerating tube from the top column of the tank to the positive terminal get accelerated. A stripper foil is placed at the terminal (either thin carbon foil or gas stripper) for which the potential is set to collect all the stripped electrons within required time span. Thus the negative ions are transformed into positive ions at the terminal. These positive ions are repelled away from the positive terminal and get accelerated to ground potential to the bottom of the tank. In this manner the same terminal potential is used to accelerate the ions twice. On exiting from the tank, the ions are bent into horizontal plane by analyzing magnet, which also selects a particular ion mass and charge state. The switching magnet diverts the high energy ions into a pre-selected beam line. The entire machine is computer controlled and is operated from the control room. The schematic of the pelletron is shown in Fig.2.5.

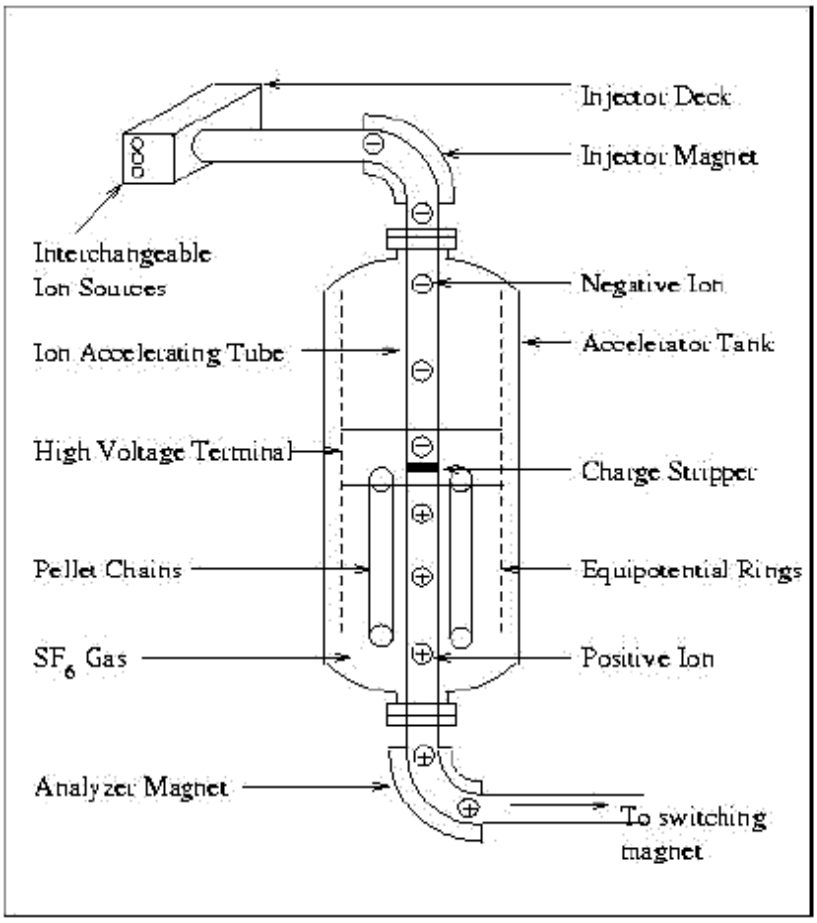

Fig.2.5: Schematic of 15MV pelletron accelerator

Fig.2.6: Materials science high vacuum irradiation chamber

The high energy irradiations were carried out using this facility at IUAC. We have used 150 MeV Ag^{12+} and 100 MeV Ag^{+12} ions for most of the high energy irradiation studies by varying the fluence from $5x10^{12}$ ions/cm^2. The samples also have been

irradiated with 70 MeV Ni ions with various fluences to see the effect of electronic energy loss. The high vacuum (~1x10^{-6} mbar) irradiation chamber is shown in Fig.2.6.

2.3.2 Tandetron accelerator at IGCAR

Ion beam characterization and the low energy irradiation work, presented in this thesis have been carried out using the accelerator facilities at IGCAR, Kalpakkam. This tandetron accelerator has dual source (i) Duoplasmatron (for H and He ions) and (ii) SNICS (almost all elements in the periodic table) with a terminal potential which can be varied between 0.1 and 1.7MV (Fig.2.7 shows the schematic).

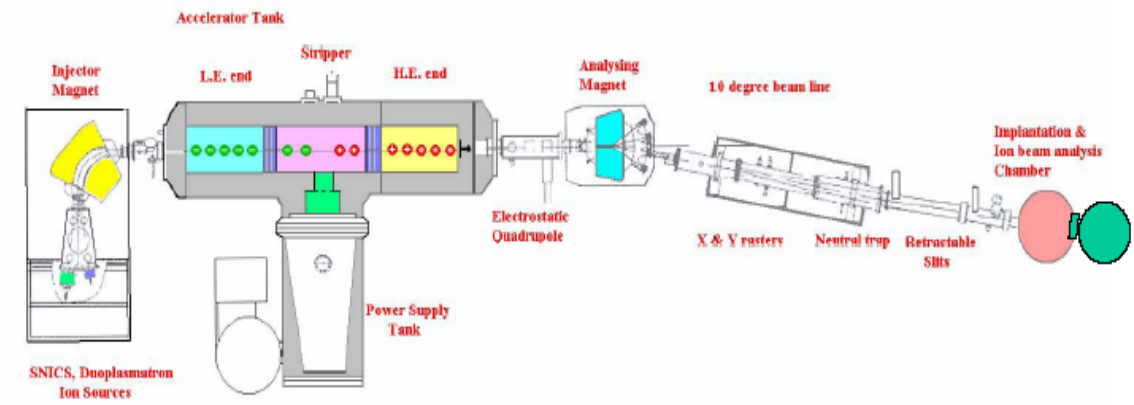

Fig.2.7: 1.7MV tandetron accelerator (Schematic)

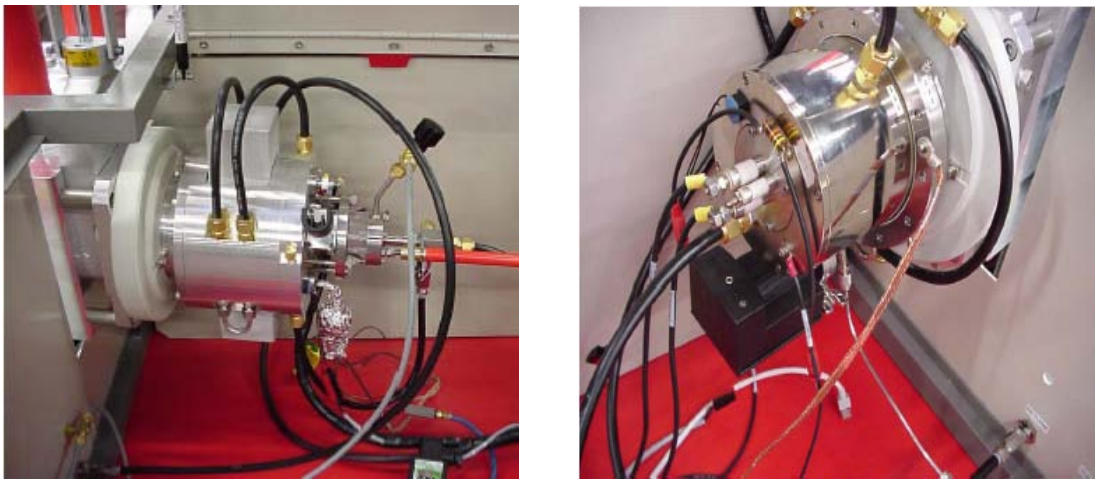

Fig.2.8: (a) SNICS Source (b) Duaplasmatron source

The central feature of the Tandetron concept is a state of the art, SF_6 insulated parallel fed Cockroft-Walton type HV power supply characterized by high reliability, extreme low noise level, high voltage stability and low ripple. A high RF driving frequency, special RC-filtering and feedback circuits eliminate hum, drift and jitter and provide a high terminal voltage stability and low terminal voltage ripple without the need for

slit stabilization. As the Tandetron HV power supply is a solid state power supply, it has the advantage of having no moving parts. As a result there are no vibrations, which might result in terminal voltage fluctuations. Also, ripple and stability values and dynamic behaviour are stable over many years of operation. A Generating Voltmeter (GVM) is used for measuring the terminal voltage. Stripper gas (N_2) at 7 Kg/cm^2 is provided in the high voltage terminal by means of a plastic tube running through the column from outside the pressure tank to a metering valve feeding gas to the stripper canal. The plastic tube is of sufficient length to withstand the high voltage. It is kept as a coil mounted inside a Teflon tube. A turbo molecular pump is provided in the terminal to pump out and recirculate the stripper gas so as to maintain a gas pressure of 50–100 microns in the stripper canal and 10^{-7} mbar in the accelerating tubes. The negative ions accelerated in the lower energy side are made positive by stripping of the electrons by N_2 gas. They are further accelerated by the high energy accelerating tube.

2.3.2.1. Duaplasmatron ion source

This source can provide H^+ and He^+ ions. Positive ion beam from the duaplasmatron ion source is accelerated by anode voltage of 100V into a charge exchange canal. Lithium vapour introduced into the charge exchange cell converts 1-2% of the positive ions to negative ions. The negative ion beam is pre-accelerated by a gap lens to 10-20 keV and focussed at the entrance of the 90^0 mass analysing magnet.

2.3.2.2 Negative sputter ion source

This source can provide ions of almost all elements, which can form negative ions. The target material in solid form necessary for producing the ion beam is packed in a copper target holder and mounted in the source and 3 to 10 kV voltage is applied. Cesium ions, produced by thermal ionization of Cesium vapour sputter the target material. The sputtered atoms pass through a thin layer of Cesium on the target and negative ions are produced. They are pre-accelerated to 20 to 30 keV and focused at the entrance of the 90^0 mass analyzing magnet.

2.3.2.3 RBS facility

The setup at IGCAR has following major parts [11]:

(i) a versatile UHV compatible five axis goniometer (from M/s Vacuum Generators, UK) with three manually controlled linear translation motions (x,y,z) and two stepper motorized closed loop control of rotational axes, angular tilt (θ) and azimuthal angle (φ) using a dual axis Intelligent Motion controller (IMC), model SM9740 of M/s Mclennan, UK;

(ii) a surface barrier detector with necessary nuclear instrumentation modules (such as, a charge sensitive preamplifier, a spectroscopic amplifier, an ion beam current integrator, a single channel analyzer (SCA) and a 16 k channel332 bit high resolution, plug-in-type multi channel analyzer (MCA).

(iii) a PC with Pentium II processor fitted with a PCI compatible data acquisition card (DAQ), model KPCI3104 from M/s Keithley Instruments, supporting many functions like analog/Digital I/O and timer/counter.

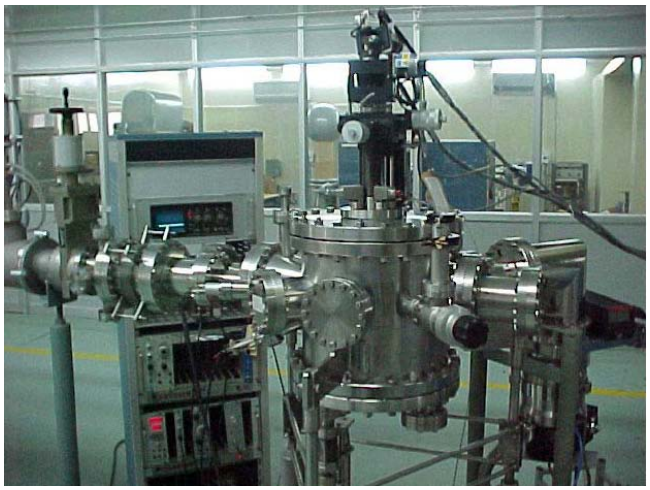

Fig.2.9: General purpose chamber

The RBS/C facility has been automated using virtual instrument automation software. This software consists of stand alone executable virtual instrument programs, position.VI, phiscan.VI, thetascan.VI, and polar.VI. These programs provide user interactive graphical interfaces which enable the user to control and read the θ and φ positions of the sample, on-line monitoring of the backscattered yield, the irradiated dose, automatic storing of the angular scan data and computing the axial channeling

position and details are given in Ref [11]. Low energy irradiation work using 3 MeV Ag^{2+} ions has also been carried out using the tandem accelerator facility. An UHV chamber (10^{-8} to 10^{-7} mbar) fitted with retractable slits, sample manipulator, surface barrier detector, electrical feed throughs, view ports, x-ray and gamma ray detectors. Ion implantation as well as ion beam analysis (Rutherford backscattering, channeling, NRA, PIXE, etc) studies will be carried out using this chamber (shown in Fig.2.9).

2.4 Thermal oxidation

This is one of the most basic deposition technologies. It is simply oxidation of the substrate surface in an oxygen rich atmosphere. The temperature is raised to 800° C-1100° C to speed up the process. This is also the only deposition technology which actually consumes some of the substrate as it proceeds. The growth of the film is spurned by diffusion of oxygen into the substrate, which means the film growth is actually downwards into the substrate. As the thickness of the oxidized layer increases, the diffusion of oxygen to the substrate becomes more difficult leading to a parabolic relationship between film thickness and oxidation time for films thicker than ~100nm. This process is naturally limited to materials that can be oxidized, and it can only form films that are oxides of that material. This is the classical process used to form silicon dioxide on a silicon substrate. A schematic diagram of a typical wafer oxidation furnace is shown in the figure 2.10 below.

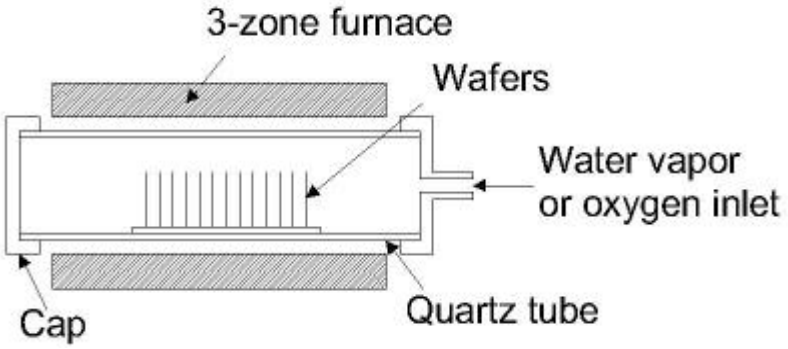

Fig. 2.10 Typical wafer oxidation furnace

2.5 Ion implantation:

The two key parameters defining the final implant profile are dose Φ (usually given in atoms/cm^2) and energy E (in keV). The dose is related to the beam current I by the following formula:

$$\Phi = It / q_i A \text{----------} (1)$$

where t denotes implantation time, A beam area and q_i is the charge per ion. Typical beam currents and implantation doses range from 1μA − 30mA and $10^{11} - 10^{16}$ atoms/cm^2. The lowest energies used start at the sub keV area for ultra shallow junctions to the MeV range for deep wells. When the ions enter the substrate they continuously loose energy and change direction by collisions with the target atoms. Due to the random nature of the collisions the total distance travelled (range) and its projection on the direction parallel to the ion beam (projected range) are random variables. Rp denotes the projected range, the depth were most ions stop. The projected straggle ΔRp describes the statistical fluctuation of Rp. When the implanted ion enters the target material there are two main effects that cause an energy loss:

• Elastic collisions with the atoms of the target material
• Inelastic collisions with the electrons.

In the work reported in this thesis, 400 keV Ge^+ ions were implanted with a fluence of $3x10^{16}$ and $5x10^{16}$ ions/cm^2 into a SiO_2 and p-type Si (001) substrates respectively. Complete experimental details have been given in the 5th chapter.

2.6 Furnace Annealing:

Furnace annealing is a process used in semiconductor device fabrication which consists of heating multiple semiconductor wafers in order to affect their structural and electrical properties. Here our mail goal is to crystallize the amorphous thin films by using furnace annealing. However, Heat treatments are designed for different effects. Furnaces are capable of processing lots of wafers at a time but each process can last between several hours and a day. Annealing of the samples was performed at 700 and 800^0C in a quartz tube furnace in Ar + H_2 (5%) reducing atmosphere. The duration of annealing was kept constant for 30 min in all cases. These annealing temperatures were chosen because in the literature it was reported that in most of the cases at very high temperatures films exhibit an amorphous nature [12].

2.7 Rapid thermal annealing (RTA)

RTA is faster than furnace annealing because the ramping and cooling cycle takes place within few minutes compared to hours in furnace annealing. The special arrangements in RTA can significantly reduce wafer emissivity variation and temperature non-uniformities. Rapid thermal processing (RTP) involving higher heating rates have long been used in the semiconductor industry as an alternative to the conventional furnace annealing. High temperature/short time annealing is of interest in the processing of thin-films in order to reduce unwanted diffusion during annealing and to minimize interaction between film and substrate.

The RTP system contains banks of tungsten-halogen lamps, symmetrically placed above and below the chamber, in order to uniformly heat the wafer. In the present set of experiments, wafers were placed in a graphite susceptor during annealing and the flow rate of ambient N_2 was 1000 sccm [13]. A pair of thermocouples monitored the temperature during annealing. Ramp up rates of about 30^0 C/s were applied to raise the temperature from ambient to the required annealing temperatures. Figure 2.11 shows the typical RTA cycle with a 'controlled cooling phase'. In this case, the ramp down rate was programmed to have slower rates with a holding step at different temperatures in order to minimize slip formation.

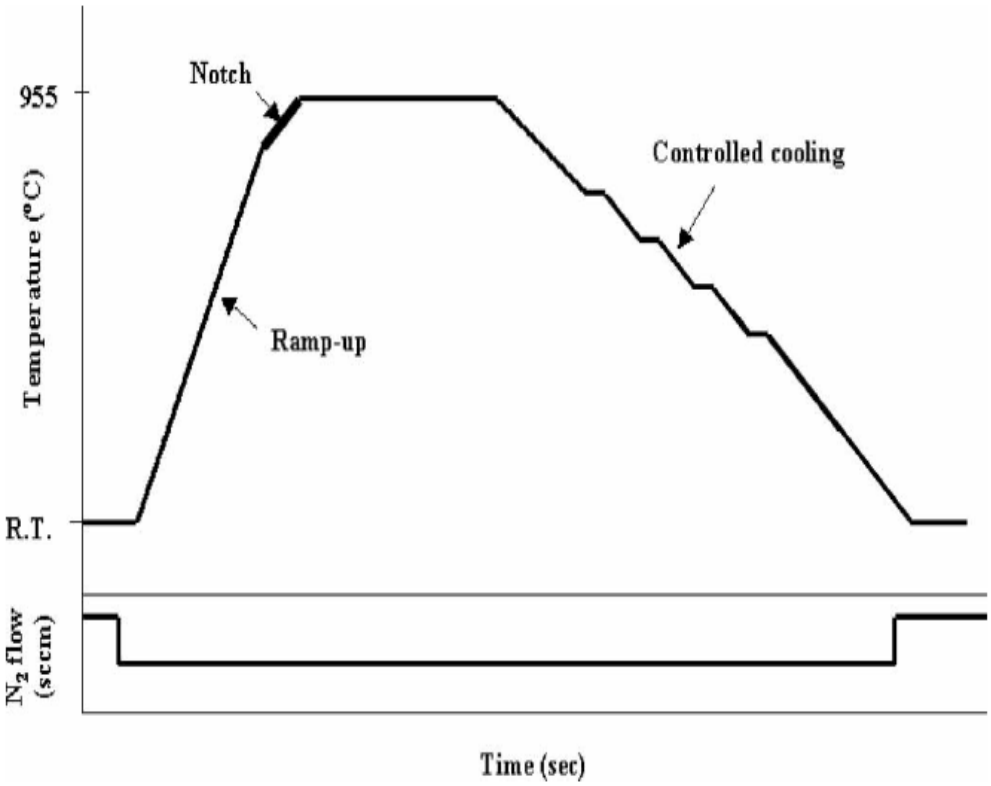

Figure 2.11 the typical annealing profile of RTA with the ambient gas flow cycle. The ramp down phase is tailored to control the cooling phase and a notch is introduced to prevent any overshoot.

RTA has been shown to be very efficient method to synthesize nanocrystals of Si and Ge compared to the conventional furnace annealing [14, 15]. The as-deposited samples were subjected to RTA in order to crystallize Ge+SiO_2 composite films prepared by Atom Beam sputtering. As-grown samples were annealed using RXV6 RTP system (AET Thermal Inc) at 700 and 800^0C for 120s in N_2 atmosphere (2000 SCCM). As it is reported, one needs to anneal the samples above crystallization of Ge amorphous films needs.

2.8 Microwave annealing:

Various annealing methods have been used to prepare nanocrystals like furnace processing, Rapid Thermal Annealing (RTA), and Laser Annealing. But, each of these methods has their own limitations. It is well known that furnace annealing takes few hours to complete the material processing. To avoid surface deterioration caused

by slow heating and cooling rates of conventional resistive heating furnaces, new ultrafast annealing techniques need to be explored. Similarly, in Laser Annealing method, the spot size is very small. Hence, it requires lot of time to cover entire surface area of wafer. In this process there is high probability for overlapping or missing some part of the wafer. Halogen lamp and laser-based rapid thermal processing techniques suffer from problems such as a possible limitation on the maximum achievable annealing temperature, surface melting, a large residual defect density, and redistribution of the implants [16, 17]. But microwave heating may solve many of these problems. Microwave heating is a process in which the materials couple with microwaves, absorb the electromagnetic energy volumetrically, and transform into heat. In conventional annealing methods the heat is transferred between objects by the mechanisms of conduction, radiation and convection. In conventional heating, there is a temperature gradient from the surface to the inside since the material's surface is first heated followed by the heat moving inward. However, microwave heating generates heat within the material first and then heats the entire volume [18]. This heating mechanism is useful for enhanced diffusion processes, reduced energy consumption, heating rates and considerably reduced processing times, improved physical and mechanical properties, decreased sintering temperatures, simplicity, unique properties, and lower environmental hazards. These are features that have not been observed in conventional processes [19-22]. Advantages of microwave annealing over conventional annealing have been reported in detail recently [23]. One can tune the structural, optical and electrical properties of nanocrstals by varying the microwave annealing parameters like annealing time, temperature, and RF deposition parameters for various applications.

The microwaves used in these experiments were produced using a 1.3 KW, 2.45 GHz single mode applicator. The samples were loaded in a chamber, thermally insulating package which is made of fiber-frax porous mullite fibers to prevent heat loss. Proper amount of silicon carbide was used as microwave susceptor around the sample within the insulating package to preheat the sample and compensate the heat loss from the sample. This configuration makes the microwave heating more uniform. The temperature of the sample was monitored by using IR pyrometer.

2.9 Characterization Techniques

2.9.1 Rutherford Backscattering Spectrometry (RBS)

Rutherford backscattering spectroscopy technique is one of the analytical techniques, which makes use of the accelerators. A target is bombarded with relatively lighter ions with energy in the MeV-range (typically 0.5–4 MeV), and the energy of the backscattered projectiles is recorded with an energy sensitive detector, typically a solid state detector. The amount of energy loss in the collision with the atomic nuclei depends on atomic number *Z* of each element present in the target material. RBS allows the quantitative determination of the composition of a material and depth profiling of individual elements. RBS is quantitative without the need for reference samples, nondestructive, has a good depth resolution of the order of several nm, and a very good sensitivity for heavy elements of the order of parts-per-million (ppm). The analyzed depth is typically about 2 μm for incident He-ions and about 20 μm for incident protons.

Thus, RBS can be used for elemental analysis, especially in the near surface region [24]. In RBS, one is concerned with incident ions of a given energy that move through a sample, losing energy along their path, and are scattered by collision with atoms in the sample. The ions scattered in the backward direction are detected and energy-analysed to obtain information about various aspects of the sample. The interaction between a projectile (ion) and a target (sample) atom can be described as an elastic collision between two isolated particles and expressed in terms of a scattering cross section. The energy of the projectile after the collision can be related to its energy before the collision by means of a kinematic factor. As the ion passes through the scattering medium, it suffers an average energy loss dE/dx. Thus the energy of a scattered ion not only depends upon the kinematic factor but also on the depth from the sample surface where the Scattering occurs. The incident ion loses some energy to reach this depth and after scattering, it again loses some energy to come out of the sample from this depth. So the energy of the detected scattered ion contains the depth information.

Kinematic factor and the energy spectrum: When a particle of mass M_1 moving with a constant velocity collides elastically with a stationary particle of mass M_2, energy is transferred from the moving to the stationary particle. In backscattering analysis, mass M_1 is the mass of an ion in the analyzing beam and M_2 is that of an atom in the sample. The energy E of the projectile after collision with the target atom, is related to its energy E_0 before the collision by the kinematic factor K defined by

$$E=KE_0 \qquad (1)$$

Where

$$K=\left[\frac{\left(M_2^2-M_1^2\sin^2\theta\right)^{1/2}+M_1\cos\theta}{M_1+M_2}\right]^2$$

If ions of known mass M_1 and known energy E_0 are directed at a sample containing an element of unknown mass M_2; by measuring the energy (E) of ions scattered at an angle q, the unknown mass M_2 can be determined.

Scattering cross section **dσ/dΩ(θ)** ***and the scattering yield:*** In RBS, ions that are scattered by an angle θ are usually detected by a solid state detector that subtends a small solid angle Ω (typically less than 10^{-2} Sr). The yield or the number of counts, Y, registered by a 100% efficient detector is given by

$$Y= QNt\,[d\sigma/d\Omega(\theta)]\,\Omega, \qquad (3)$$

where Q is the number of ions incident on the sample, N the bulk density of atoms in the sample, t the sample thickness and $d\sigma/d\Omega(\theta)$ the average differential scattering cross section for scattering into a solid angle Ω at a scattering angle θ. The differential cross section is given by Rutherford's formula (in laboratory frame of reference):

$$\frac{d\sigma}{d\Omega}(\theta)= \left(\frac{Z_1Z_2e^2}{4E}\right)^2 \frac{4}{\sin^4\theta}\frac{\left(\left\{1-[(M_1/M_2)\sin\theta]^2\right\}^{1/2}+\cos\theta\right)^2}{\left\{1-[(M_1/M_2)\sin\theta]^2\right\}^{1/2}}$$

where E is the energy of the ion immediately before scattering and Z_1 and Z_2 are the atomic numbers of the ion and the target atom respectively.

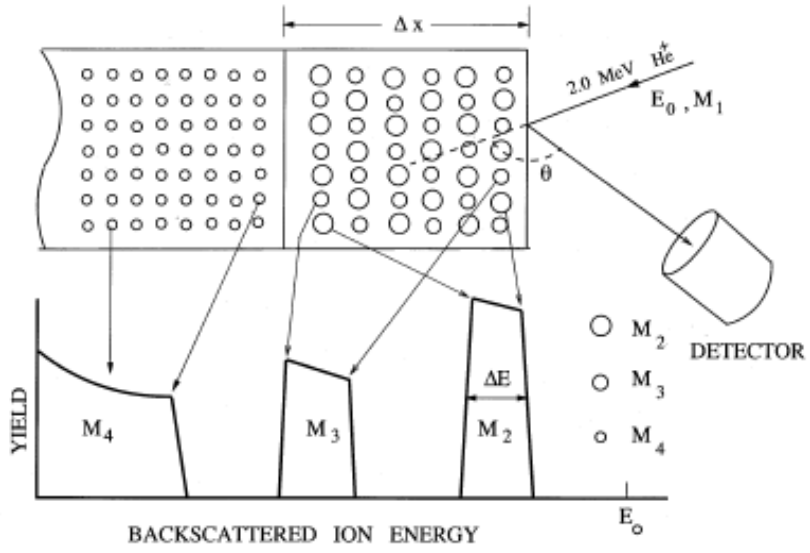

Figure 2.12. Schematic diagram of illustrating backscattering spectrum of ions of mass M_1 impinging on a thin film containing two different masses (M_2, M_3) deposited on a low-mass (M_4) elemental substrate. Energies of backscattered ions from various depths and various atoms are marked by arrows. The film thickness (Δx) is determined from the measured energy width ΔE.

Energy loss of ions (dE/dx): As an energetic ion passes through a solid, it loses energy on its way. For light ions and for ion energies used in RBS analysis (0.1–3 MeV) there are two dominant energy loss processes: (i) By interactions with bound or free electrons in the solid [electronic energy loss: $(dE/dx)_e$] and (ii) by interactions with the screened or unscreened nuclei of the atoms in the solid [nuclear energy loss: $(dE/dx)_n$]. From the knowledge of the total $dE/dx = (dE/dx)_n + (dE/dx)_e$ for a given ion in a given sample material, the thickness (Δx) of thin film samples can be determined from the measured energy width (ΔE) in the RBS spectrum. This is illustrated in Figure 1 which shows schematically an RBS spectrum from a sample containing a thin film of a compound (two elements) on a thick substrate (single element).

The RBS data is analyzed by Rutherford universal manipulation program (RUMP) or SIMNRA to find the elemental composition, film thickness and depth profile.

Ideal Uses for RBS Analysis:

- Thin film composition/thickness
- Determine areal concentrations (atoms/cm^2)

- Determine film density (when thickness is known)

Strengths of RBS Analysis:

- Non-destructive compositional analysis
- Quantitative without standards
- Whole wafer analysis (150, 200, 300 mm)
- Conductor and insulator analysis
- Hydrogen measurements (in HFS mode)
- Low-Z element sensitivity (in NRA mode)

Limitations of RBS Analysis:

- Large analysis area (~2 mm)
- Useful information limited to top ~1 μm of samples

2.9.2 X-ray diffraction (XRD)

The XRD method for materials analysis was devised by Debye and Scherrer in 1916. Phase identification was introduced later in 1938 by Hanawalt *et al*. (USA).The X-rays are usually generated when high-energy electrons impact on a metal target. The X-rays have wavelengths from 0.1 to 10 A^0, which are located between y-radiation and ultraviolet rays. The wavelengths, most commonly used in crystallography, range between 0.5 to 2.5 A^0, since they are of the same order of magnitude as the shortest interatomic distances observed in both organic and inorganic materials. In an X-ray diffractometer, X-rays are produced whenever high speed electrons collide with metal (Cu) target. X ray tube consists of: (a) source of electrons (b) a high accelerator voltage and (c) a metal target (Cu). X-rays are generated within an evacuated tube and exit through a window composed of a light element, usually beryllium. Inside the tube, a current is passed through a filament (usually tungsten) to generate electrons. These electrons are then accelerated through a potential difference (~40kV) towards target made of copper. When the incoming electrons have sufficient energy to eject electrons from the core-shell (K shell) of copper, a characteristic spectrum is created. The characteristic spectrum is also composed of discrete energies, which are suppressed with suitable filters to have mono-energetic X-rays at the sample.

X-ray powder diffraction is a non-destructive technique widely applied for the characterization of crystalline materials. The method has been traditionally used for phase identification, quantitative analysis and the determination of structure imperfections. It is useful to get the information about the crystallinity of the material, lattice parameter, phase present and grain (particles size) size. The variation of peak position with sample orientation can be utilized to deduce the information regarding the internal strain of the sample. In recent years, applications have been extended to new areas, such as the determination of crystal structures and the extraction of three-dimensional microstructural properties.

When X-ray radiation passes through matter, the radiation interacts with the electrons in the atoms, resulting in scattering of the radiation. The atoms in crystals interact with X-ray waves in such a way as to produce interference. The interaction can be thought of as if the atoms in a crystal structure reflect the waves. This result in diffraction where X-rays are emitted at characteristic angles based on the spacings between the atoms organized in crystalline structures called planes (Fig. 2.13).

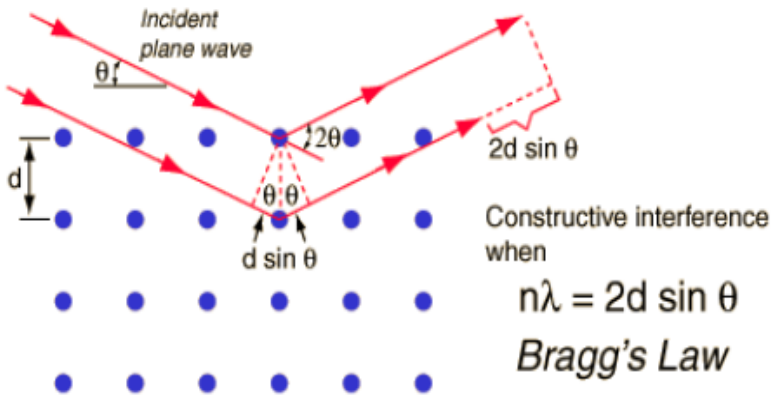

Fig. 2.13 X-ray diffraction schematic diagram

Most of the X-rays undergo destructive interference; however, the X-rays that interact with the sample at a specific angle θ undergo constructive interference, which results in a signal for that particular angle [25].

The condition for the constructive interference between the scattered X-ray is given by Bragg's condition. Constructive interference of the X-ray from successive planes occurs when the path difference is an integral multiple of wavelength so that here d_{hkl} is the interplanar spacing and θ is the angle of incidence also known as the Bragg angle. The resultant spectrum can be plotted between the intensity and the 2θ. XRD exploits the wave nature of electromagnetic radiation and as X-rays interact with a sample, they interfere with each other. The advanced D-8 X-ray diffractometer was procured from Bruker AXS, Germany. Normally, the model has vertically mounted goniometer with sample being in horizontal plane. A photograph of the XRD setup with its sample cooling unit is shown in Fig. 2.14

FIG. 2.14: A photograph of the XRD setup in materials science beam line at IUAC.

This instrument consists of CuK_{α} rotating anode X-ray source (wavelength: 1.54 Å, energy: 8.0 keV), gobble mirror, LiF monochromator, scintillator detector and high speed Vantec detector. The Vantec detector (due to its position sensitivity) makes data collection 60 times faster as compared to the conventional NaI detector with reasonably good resolution. The position sensitive feature of Vantec detector is very useful for in-situ measurement during ion irradiation experiments, where fast

scanning is required for optimum utilization of the accelerator time [26]. The average size of the nanocrystals is calculated using Scherrer's formula [27] given by

$$D = \frac{0.9\,\lambda}{\beta\, Cos\theta_B}$$

Where λ is the wavelength of the X-ray source (*i.e*, 1.5406A^0 for CuKα), β = FWHM (in radians) and θ_B is Bragg angle and D is the diameter of the nanocrystal.

The strain in the nanocrystalline Germanium samples is estimated using Williamson-Hall method. The Williamson-Hall equation [28] can be written as

$$\beta \text{ Cos } \theta_B = [K\lambda/D] + [4\varepsilon \text{ Sin } \theta_B] \qquad (1)$$

Here K is the shape factor, λ is the x-ray wavelength, θ_B is the Bragg angle and D is the average crystallite size. Here ε is the root mean square value of the microstrain. Plotting the value of $\beta \cos\theta_B$ as a function of $4\sin\theta_B$ the microstrain ε may be estimated from the slope of the line.

2.9.3 Raman spectroscopy

The scattering of light may be thought of as the redirection of light that takes place when an electromagnetic (EM) wave (i.e. an incident light ray) encounters an obstacle or nonhomogeneity. As the EM wave interacts with the matter, the electron orbits within the constituent molecules are perturbed periodically with the same frequency (ν_o) as the electric field of the incident wave. The oscillation or perturbation of the electron cloud results in a periodic separation of charge within the molecules, which is called an induced dipole moment. The oscillating induced dipole moment is manifest as a source of EM radiation, thereby resulting in scattered light. The majority of light scattered is emitted at the identical frequency (ν_o) of the incident light, a process referred to as elastic scattering. However, as explained below, additional light is scattered at different frequencies, a process referred to as inelastic scattering. Raman scattering is one such example of inelastic scattering.

When light is transmitted through matter, it is scattered in random directions. Most of the scattered light is of the same wavelength (or frequency) as the incident light. This is known as "Rayleigh scattering" and is considered elastic as the scattered photon has the same energy as the incident photon. Some light is inelastically scattered-scattered photon having higher or lower energy than incident one-at a different wavelength (or

frequency). This is called "Raman Scattering". This shifting of frequency is also called "Raman Effect", which arises when the incident light excites molecules in the sample, which subsequently scatters the light. The schematic illustration of the differences between Rayleigh (elastic) and Raman (inelastic) scattering has been shown in Fig. 2.15

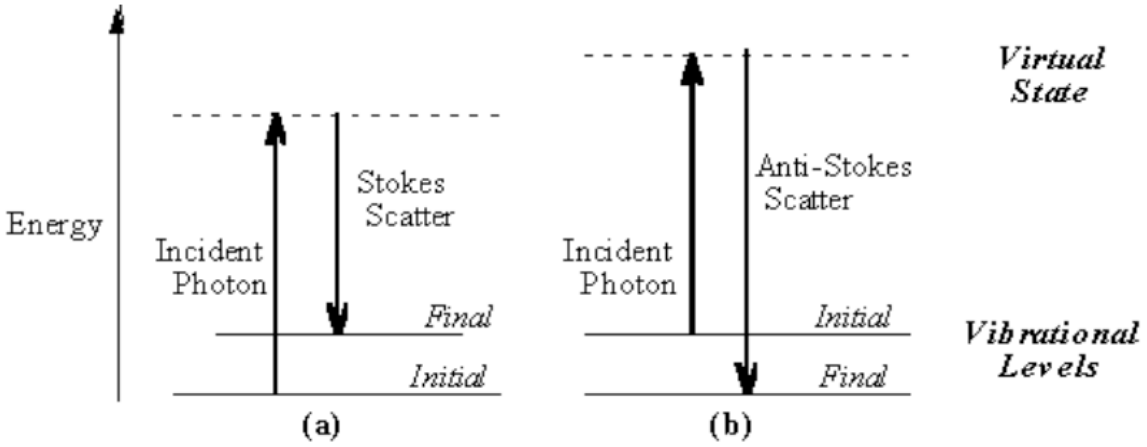

Energy level diagram for Raman scattering; (a) Stokes scattering, (b) anti-Stokes scattering

Fig.2.15: A schematic illustration of the differences between Rayleigh (elastic) and Raman (inelastic) scattering.

Typically, only one part in a thousand of the total intensity of incident light is Rayleigh scattered, while for Raman scattering this value drops to one part in a million (0.0001 percent). Thus, Raman Effect being quite weak, it is a major challenge in Raman spectroscopy to attenuate the light that is elastically scattered in order to detect the inelastically scattered Raman light.

"Raman Scattering" results from the molecule changing its molecular motions. The energy difference between the incident light and the Raman scattered light is equal to the energy involved in changing the molecule's vibrational state, and is called the "Raman shift". If the initial beam is sufficiently intense and monochromatic, a threshold can be reached beyond which light at the Raman frequencies is amplified, builds up strongly, and generally exhibits the characteristics of stimulated emission. This is called the stimulated or coherent Raman Effect.

A typical Raman system consists of the following basic components: (1) an excitation source, usually a laser; (2) optics for sample illumination; (3) a double or triple monochromator; and (4) a signal processing system consisting of a detector, an amplifier, and an output device. A block diagram of the Raman spectrometer is shown in Fig.2.16. A sample is mounted in the sample chamber and laser light is focused on it with the help of a lens. The scattered light is collected using another lens and is focused at the entrance slit of the monochromator. Monochromator slit widths are set for desired spectral resolution. Monochromator effectively rejects stray light and serves as a dispersing element for incoming radiation. The light leaving the exit slit of the monochromator is collected and focused on the surface of a detector. This optical signal is converted to an electrical signal within the detector and further manipulated using detector electronics. Such a signal is stored in computer memory for each predetermined frequency interval in a conventional Raman system using a CCD or photomultiplier tube (PMT) detector, light intensity at various frequencies is measured by scanning the monochromator.

Fig. 2.16 Raman spectrometer System

Raman scattering spectra of the our films were obtained before and after annealing in backscattering configuration with a Renishaw Raman microscope using a 514.5 nm Ar+ laser excitation source. Shift in the peak position and an asymmetrical broadening of the Raman peak with the spectrum of the bulk Ge sample have been discussed. Crystalline nature of films has been observed from the Raman spectra. Results are discussed in various chapters in detail.

2.9.4 Fourier Transform Infrared spectroscopy (FTIR)

Infrared spectroscopy reveals information about the vibrational states of a molecule. Intensity and spectral position of IR absorptions allow the identification of structural elements of molecule. The development of Fourier Transform Infrared spectroscopy (FTIR) in the early 1970s provided a quantum leap in infrared analytical capabilities for monitoring trace pollutants in ambient air. During the past years, the technique of FTIR has become more and more important as an instrument for obtaining high quality IR spectra in analytical research and process control. There are two reasons for this development, viz. the capability of Infrared Fourier Transform Spectrometers of producing routine spectra in shorter times and of better quality than those from conventional grating systems and the extension of the possibilities of performing measurements which would be impossible with grating systems. Superior sensitivity and resolution, rapid sample measurement, absolute wavelength accuracy, versatile spectra processing, and total automation of complex analysis are fundamental reasons why one is turning to FTIR. The basic components of an FTIR are shown schematically in Figure 2.17. The infrared source emits a broad band of different wavelength of infrared radiation. Infrared radiation is projected onto the beam splitter. An ideal beam splitter consists of a non-absorbing film which transmits 50% of the radiation to the mirror, which is moving back and forth at a constant speed, whereas 50% of the radiation is reflected to the fixed mirror. After being reflected, the two beams will recombine at the beam splitter where interference between the beams takes place. The interferometer performs an optical inverse Fourier transform on the entering IR radiation. The modulated IR beam passes through the sample where it is absorbed to various extents at different wavelengths by the various molecules present. Finally the intensity of the IR beam is detected by a detector. The detected signal is digitized and Fourier transformed by the computer to get the IR spectrum of the sample gas.

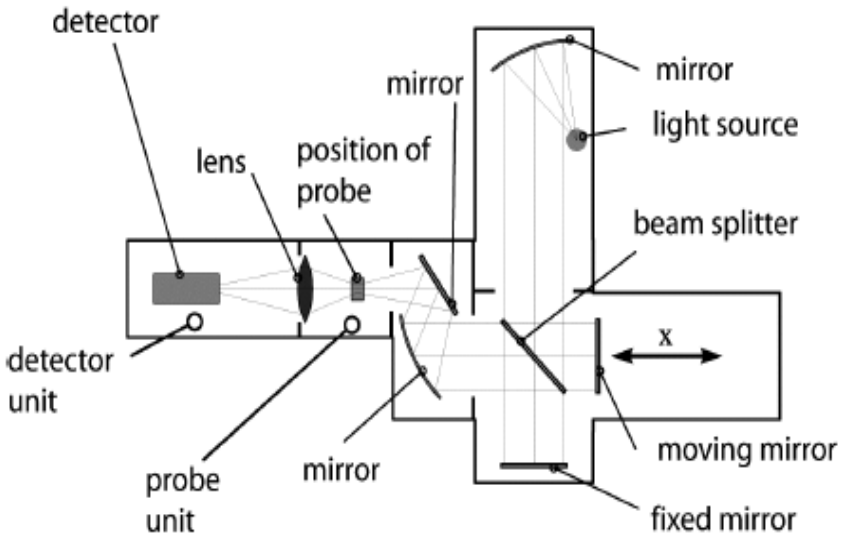

Figure 2.17: Design of an FTIR spectrometer

In the infrared region of the spectrum, the resonance frequencies of a molecule are due to the presence of molecular functional groups specific to the molecule. Among them are typical functional groups, hydrogen bonding, but also determination of conformations or even investigation of chemical reactions. A functional group is simply a group of two or more atoms, bonded together in a specific way. In the water molecule (H_2O), it is the O-H functional group that contributes to the resonance frequency around 3450 cm^{-1}. The benefit is that different types of molecules, such as the additive ZDDP (zinc dialkyl dithiophosphate) and water, or fuel and glycol that have different functional groups absorb infrared light at different wavelengths. Therefore, it is possible to determine the presence of different molecules in the sample with FTIR, simply by measuring the absorption at different wavelengths, or wavenumber.

2.9.5 Atomic force microscopy

Surface morphology of the samples was characterized using ***SPA400, Seiko Instruments Inc***. Both **D**ynamic **F**orce **M**icroscopy and AFM were used. The analysis software helps in extracting the required data from the recorded images. The roughness values and the sectional images can be obtained offline using the software. The topographical image of various scan areas is recorded and our scanner can

support as large as about $10\mu m^2$. Normally quantitative roughness information of composite films is obtained over lateral length scales ranging from 5nm to 5μm.

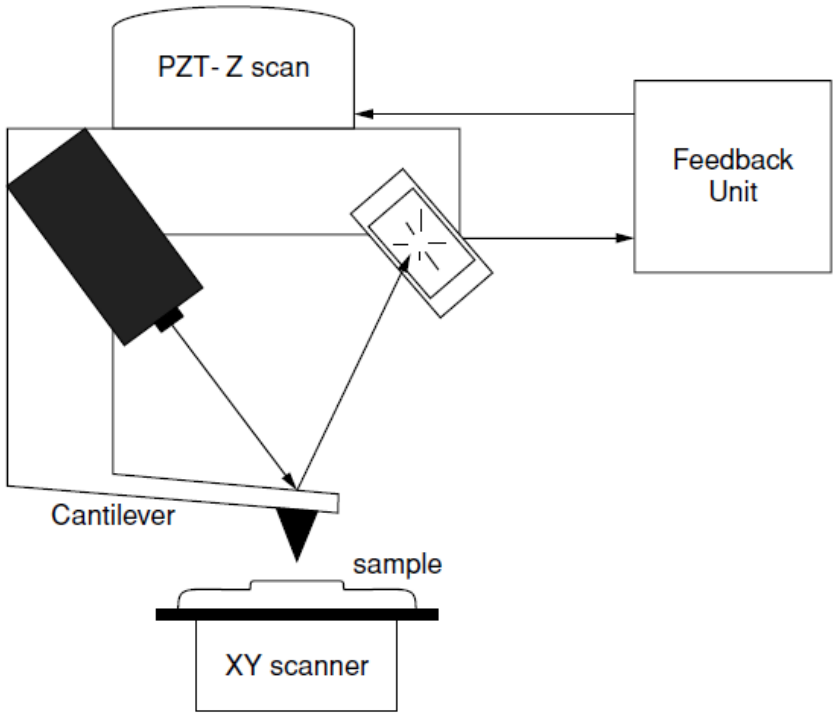

Figure 2.18 Schematic of AFM

The atomic force microscope (AFM) or scanning force microscope (SFM), like all other scanning probe microscopes, utilizes a sharp probe moving over the surface of a sample in a raster scan (see Fig. 2.18). In the case of the AFM, the probe is a tip on the end of a cantilever that bends in response to the force between the tip and the sample. An optical detector monitors the extent of bending of the lever. The cantilever beam obeys Hooke's Law for small displacements, and the interaction force between the tip and the sample can be found. The movement of the tip or sample is performed by an extremely precise positioning device made from piezoelectric ceramics. The scanner is capable of sub-nanometer resolution in the *x*-, *y*- and *z*-directions.

When the probe–surface spacing is relatively large (~1 nm or greater), the interactions are dominated by long-range van der Waals forces (Fig. 2.19). These attractive forces depend exponentially on distance and are extremely sensitive to

probe-tip shape. Other attractive forces include metallic adhesion forces and charge accumulation between the probe tip and the nearest surface atom.

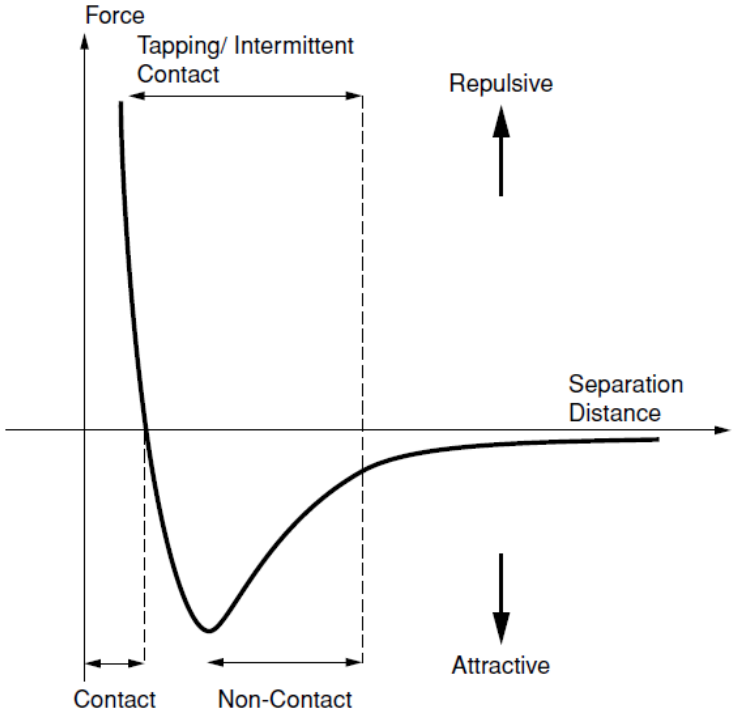

Figure 2.19 Schematic of van der Waals forces as a function of probe-tip–surface spacing.

At small spatial separations (~0.1 nm or less), the wave function of the probe–surface overlap and short-range quantum-mechanical exchange-correlation forces dominate due to the Pauli Exclusion Principle. These forces decay exponentially with increasing distance:

$$F = -\gamma(\Delta\varepsilon_C)\chi\left(\sigma\frac{H}{e^2}\right)^{1/2}$$

where $\Delta\varepsilon_C$ is the width of the conduction band, γ is a dimensionless factor approximately equal to one, χ is the decay rate of the force, and σ is the conductance. The slope of the van der Waals curve is very steep in the repulsive or contact region (Fig. 2.19). As a result, the repulsive van derWaals force balances almost any force that attempts to push the atoms closer together. For example, in AFM, when the cantilever pushes the tip against the sample, the cantilever deforms as opposed to pressing the probe tip closer to the surface. Only negligible reduction in the

interatomic separation between the probe-tip atom and the surface atoms is probable, even with the use of a rigid cantilever. These cantilevers will apply substantial forces onto the samples surface and will more than likely result in surface deformation. The point of balance between attractive and repulsive forces is defined as the *mechanical point contact*. Van der Waals forces also dominate the interaction between nonmagnetic and electrically natural solids that are separated by a distance of several nanometers. In addition to the repulsive van der Waals force described above, two other forces are generally present during contact AFM operation: a capillary force exerted by the thin water layer often present in an ambient environment, and the force exerted by the cantilever itself. The capillary force arises when water wicks its way around the tip, applying a strong attractive force (about 10^{-8}N) that holds the tip in contact with the surface. As long as the tip is in contact with the sample, the capillary force should be constant because the distance between the tip and the sample is virtually incompressible. It is also assumed that the water layer is reasonably homogeneous. The variable force in contact AFM is the force exerted by the cantilever. The total force that the tip exerts on the sample is the sum of the capillary plus cantilever forces, and must be balanced by the repulsive van derWaals force for contact AFM. The magnitude of the total force exerted on the sample varies from 10^{-8}N to the more typical operating range of 10−7 to 10^{-6}N [29].

Three imaging modes, contact mode, non-contact mode, and intermittent contact or tapping mode, can be used to produce topographic images of sample surfaces.

Contact Mode is widely used and it is the first and foremost mode of operation. As the tip is raster-scanned across the surface, it is deflected as it moves over the surface corrugation. In constant force mode, the tip is constantly adjusted to maintain a constant deflection, and therefore constant height above the surface. It is this adjustment that is displayed as data. However, the ability to track the surface in this manner is limited by the feedback circuit. Sometimes the tip is allowed to scan without this adjustment, and one measures only the deflection. This is useful for small, high-speed atomic resolution scans, and is known as variable-deflection mode. Because the tip is in hard contact with the surface, the stiffness of the lever needs to be less that the effective spring constant holding atoms together, which is on the order of 1 - 10 nN/nm. Most contact mode levers have a spring constant of < 1N/m.

Non-contact mode is a method where the cantilever is oscillated above the surface of the sample at distance such that it is no longer in the repulsive regime but in the attractive regime of the inter- molecular force curve. The operation of non-contact imaging is quite difficult in ambient conditions because of the existing thin layer of water on the tip and the surface. As the tip is brought close to the surface, a small capillary bridge between the tip and the sample and cause the tip to "jump-to-contact."

Tapping mode tends to be more applicable to general imaging in air, particularly for soft samples, as the resolution is similar to contact mode while the forces applied to the sample are lower and less damaging. In tapping mode, the cantilever oscillates close to its first bending mode resonance frequency, as in non-contact mode. However, the oscillation amplitude of the probe tip is much larger than for non-contact mode, often in the range of 20 nm to 200 nm, and the tip makes contact with the sample for a short duration in each oscillation cycle. As the tip approaches the sample, the tip-sample interactions alter the amplitude, resonance frequency, and phase angle of the oscillating cantilever. During scanning, the amplitude at the operating frequency is maintained at a constant level, called the set-point amplitude, by adjusting the relative position of the tip with respect to the sample. In general, the amplitude of oscillation during scanning should be large enough such that the probe maintains enough energy for the tip to tap through and back out of the surface contamination layer. In this thesis, AFM was used to characterize the surface morphology of the composite films.

2.9.6 Transmission electron microscopy

2.9.6.1 Transmission Electron Microscopy

Transmission electron microscopy (TEM) is a valuable tool in materials science since it allows for the observation and analysis of materials down to the nanometer scale [29-31]. The transmission electron microscope uses a high energy electron beam transmitted through a very thin sample to image and analyze the microstructure of materials with atomic scale resolution. The electrons are focused with electromagnetic lenses and the image is observed on a fluorescent screen, or recorded on film or digital camera. The electrons are accelerated at several hundred kV, giving wavelengths much smaller than that of light: 200kV electrons have a wavelength of 0.025Å. However, whereas the resolution of the optical microscope is limited by the wavelength of light, that of the electron microscope is limited by aberrations inherent in electromagnetic lenses, to about 1-2 Å. Because the wavelength of electrons is much smaller than that of light, the optimal resolution attainable for TEM images is many orders of magnitude better than that from a light microscope. Thus, TEMs can reveal the finest details of internal structure—in some cases as small as individual atoms. Magnifications greater than 300K times are routinely obtained for many materials. Under optimal conditions, even individual atoms can be imaged. Because of the high spatial resolution obtained, TEMs are often employed to determine the detailed crystallography of fine-grained or thin film materials. The biological sciences often use TEM as a complementary tool to conventional crystallographic methods such as X-ray diffraction.

Figure 2.20 shows a cross-section schematic of the components and beam path of the typical TEM. The four basic components that are required to produce a magnified image are (1) an electron gun, which emits a beam of monochromatic electrons as the illumination source, (2) a set of condenser lenses to focus the illumination onto the specimen, (3) an objective lens used to form the first image of the specimen, and (4) a series of magnifying lenses to create the final magnified image. The electron gun produces a beam of monochromatic electrons along the optical axis of the microscope. An intense electron beam is required for imaging at high magnification. The amount of electronic energy deposited in the beam spot causes sample damage, and ultimately limits the resolution. Electrons are emitted by heating a filament

(*thermionic emission*, tungsten or LaB6 filament) or from an unheated filament that has an extremely high potential gradient placed across the filament (field *emission*, fine-tipped single-crystal tungsten). The electron beam is focused into a thin, coherent beam with the use of the first and second condenser lenses. The first lens controls the beam-spot size and dictates the general size range of the final spot that illuminates the sample. The second lens controls the intensity and the size of the spot on the sample. A user-selectable, condenser aperture removes high-angle electrons (those far from the optic axis) and allows for a collimated beam down the optical axis. The beam strikes the specimen, and a portion of the beam is transmitted through the sample and other parts of the beam are diffracted. The sample stage must allow for easy access to the specimen, mechanical stability, and reproducible translations. Specialty stages allow for excess cooling (liquid nitrogen temperatures) or heating (~500^0C) or increased tilting ($\pm 60^0$). State-of-the-art stages allow for in-situ nano-indentation, in-situ electrical probing, or scanning tunneling microscopy.

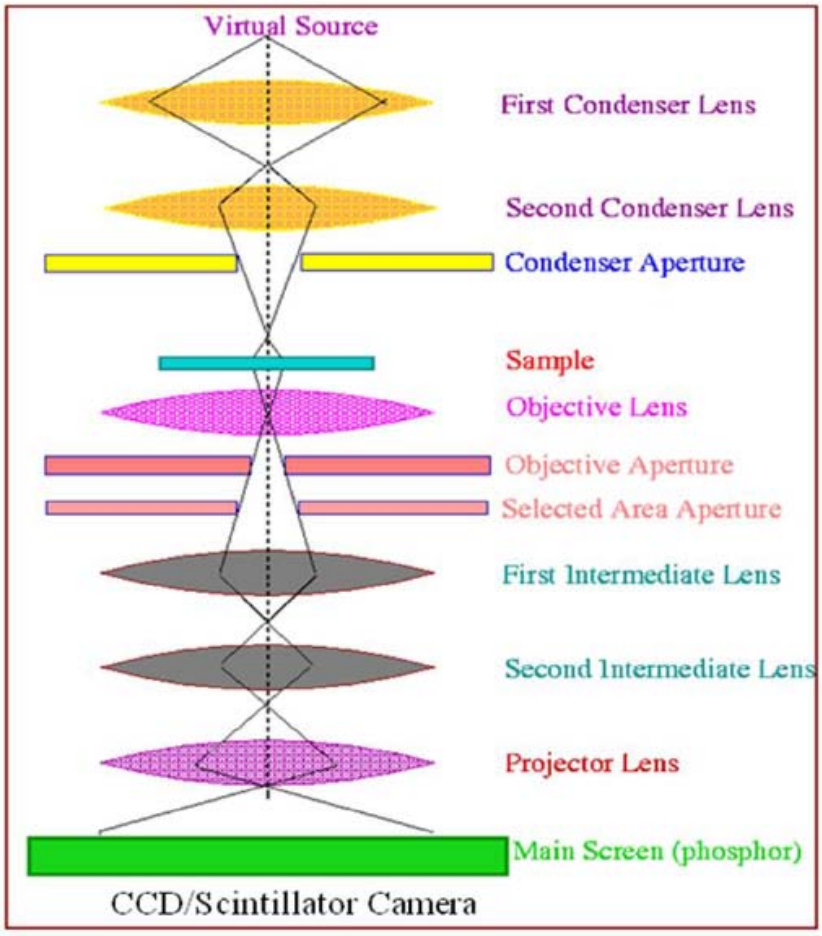

Fig 2.20 Block diagram of Transmission Electron Microscope

The transmitted portion of the beam is focused by the objective lens into an image. The electron image is focused by adjusting the objective focal length. Any defects associated with the objective lens are subsequently magnified onto the final image. Chromatic aberration results from variation in the electron velocity entering the specimen. Spherical aberration is due to variations in focal length as a function of radial position of the electrons in the beam. Such aberration is influenced by the effective aperture of the microscope. Lens-current fluctuations produce lens instabilities, which give unstable images.

The objective aperture and selected area diffraction aperture can both restrict the beam. The objective aperture enhances image contrast by blocking out high-angle diffracted electrons. Use of a selected-area aperture enables the user to image the electron diffraction pattern from a specific portion of the TEM sample. Accurate alignment of the various apertures is important for good imaging. The image is passed down the column through the intermediate and projector lenses. There the image of the sample is magnified onto the viewing screen or onto the recording media. Upon selection of the appropriate control, the projector system magnifies the image of the electron diffraction pattern from the rear focal plane of the objective lens. It is the projection lens setting that defines the camera length. The electrons that form the image strike a fluorescent screen (typically coated with a fine-grain ZnS). When the electrons strike the screen, fluorescence occurs and results in the formation of a visible image, allowing the user to see the image. The darker areas of the image represent those areas of the sample where fewer electrons were transmitted (they are thicker or denser). The lighter areas of the image represent those areas of the sample where more electrons were transmitted (they are thinner or less dense). Note that X-rays are also generated when the electrons strike the viewing screen. The leaded viewing glass absorbs the X-rays. A photographic plate or digital camera resides beneath the moveable viewing screen. A potential operational hazard can occur when the electron beam strikes the apertures or part of the column and produces X-rays. Hence, the column is shielded to protect the operator. On the other hand, the column must be shielded from external stray radiation, vibrations, and magnetic fields, if one desires a stable image.

2.9.6.2 Imaging Modes

In the bright field (BF) mode of the TEM, an aperture is placed in the back focal plane of the objective lens, allowing only the transmitted or direct beam to pass (see Fig. 2.21a). The diffracted beams are blocked. In this case, diffraction contrast contributes to image formation. Crystalline regions that are oriented so as to strongly diffract intensity away from the transmitted beam will appear dark. In addition, *Z*-contrast occurs when regions with heavy atoms scatter more of the incident beam and appear darker. Useful information is obtainable from BF images. However, interpretation of contrast should be done with care, since the phenomena mentioned above occur simultaneously. In dark field (DF) images, a selected diffracted beam is allowed to pass through the objective aperture (see Fig. 2.21b).

This is accomplished by electromagnetic lenses that effectively tilt the incident beam from the optical axis by an amount $2\theta_{hkl}$ such that the *hkl* diffracted beam exits the sample parallel to the TEM optical axis. The aperture blocks the direct beam. In contrast to the direct beam, the diffracted beam has interacted strongly with the specimen, and very useful information is often present in DF images, e.g., about planar defects, stacking faults, or particles. In many analyses, correlation between DF and BF images provides useful information about structure and morphology, including layer thickness, grain size, grain orientation, and defect orientations. In general, one or both of these imaging modes are used in conjunction with electron diffraction analysis [29].

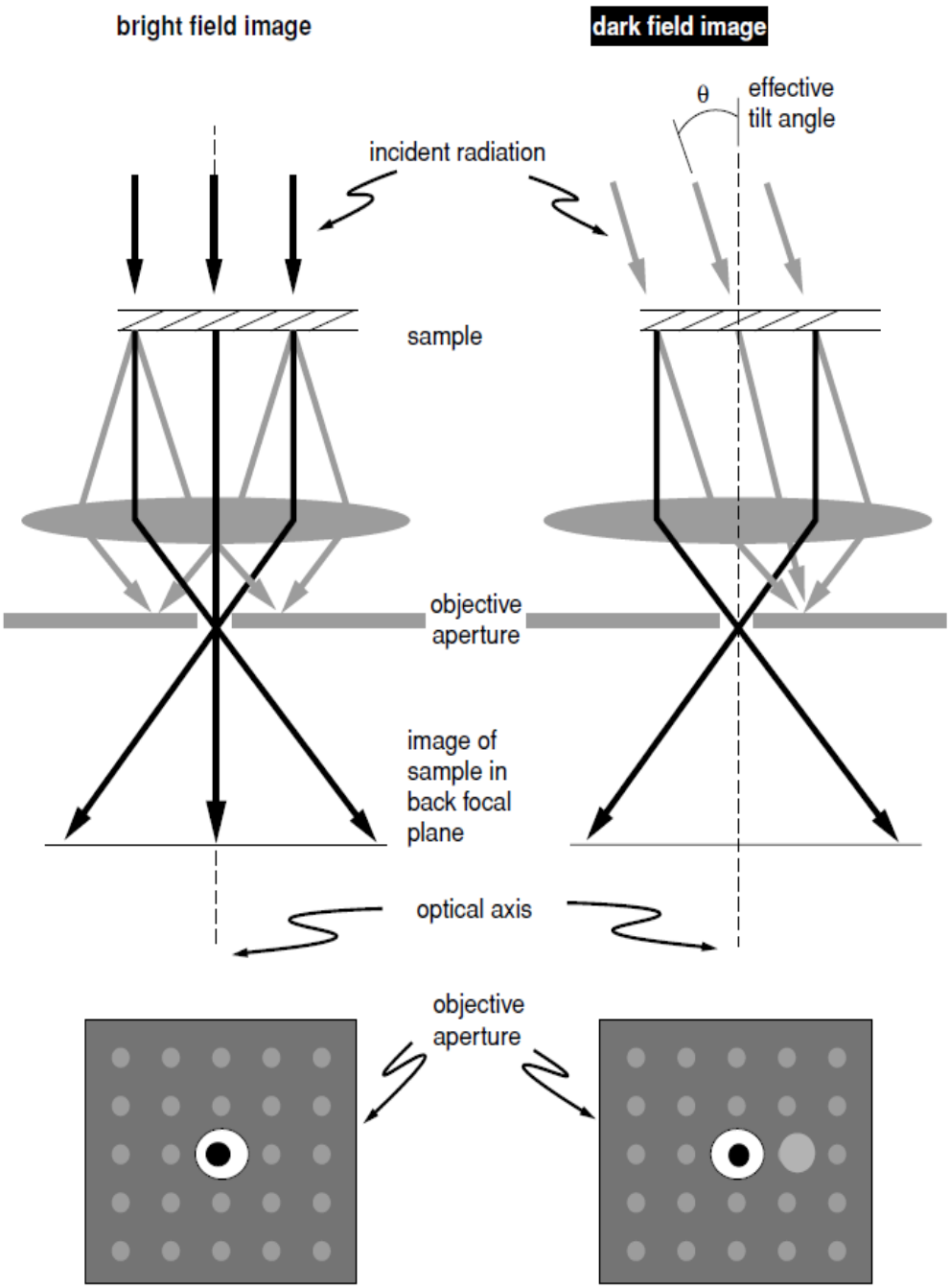

Figure 2.21 Diagram of an electron's path during (a) bright field imaging and (b) dark field imaging

2.10 Conclusions

In this chapter we have given the details of the experimental facilities for synthesis and characterization techniques used in this work. Further details of these facilities are given in respective chapters as and when required. Here, we have given complete description of the facilities with relevant references. Some of the above mentioned details may be repeated in certain cases in the following chapters for the sake of completeness.

2.11 References

1. R. Behrisch (ed.) (1981). Sputtering by Particle bombardment: Springer, Berlin
2. Kasturi L. Chopra, Thin Film Phenomena, McGraw Hill Company 1969.
3. E.B. Graper, Handbook of Thin Film Process Technology, IOP Publishing Ltd. (1995).
4. D. Kabiraj, S.R. Abhilash, L. Vanmarcke, N. Cinausero, J. C. Pivin and D. K. Avasthi, Nucl. Inst. and Meth. B 244 (2006) 100.
5. D. K. Avasthi, Y. K. Mishra, D. Kabiraj, N. P. Lalla and J. C. Pivin, Nanotechnology 18 (2007) 125604.
6. N Srinivasa Rao, A P Pathak, N Sathish, G Devaraju, V Saikiran, P K Kulriya, D C Agarwal, G Sai Saravanan and D K Avasthi (Accepted for publication in Solid State Communications Journal).
7. N. Srinivasa Rao, S. Dhamodaran, A.P. Pathak, P.K. Kulriya, Y.K.Mishra, F. Singh, D. Kabiraj, J.C. Pivin, D.K. Avasthi. Nucl. Inst. Meth B 264 (2007) 249–253.
8. A Singha1, A Roy, D Kabiraj and D Kanjilal, Semicond. Sci. Technol. 21 (2006) 1691
9. N Srinivasa Rao, S Dhamodaran, A P Pathak, D Kabiraj, S A Khan, B K Panigrahi, K G M Nair, B Sundaravel, J C Pivin and D K Avasthi, Radiation Effects and Defects in Solids. Vol. 164, Nos. 7–8, July 2009, 452.
10. D Kanjilal, S Chopra, M M Narayanan, I S Iyer, V Jha, R Joshi and S K Datta, Nucl. Instr. and Meth. A 238 (1993) 97.
11. K Suresh, B Sundaravel, B K Panigrahi, K G M Nair and B Viswanathan, Rev. Sci. Instr. 75 (2004) 4891.
12. W.K. Choi, Y.W. Ho, S.P. Ng and V. Ng, J. Appl. Phys. 89 (2001), p. 2168.

13. G. Sai Saravanan, K. Mahadeva Bhat, H. P. Vyas,; K. Muraleedharan, A. P. Pathak, Radiation Effects and Defects in Solids, Vol. 163, No. 9, September 2008, 737–748
14. F. Roozeboom_Ed.., Advances in Rapid Thermal and Integrated Processing, Kluwer Academic Publisher, 1996
15. O. Adeoya, M. Hage Ali, J.C. Muller, P. Siffert, 1987 Appl. Phys. Lett. 50, 1736.
16. Y. Tanaka, H. Tanoue, and K. Arai, J. Appl. Phys. 93 (2003) 5934.
17. S.D. Ruksell and A.D. Ramirez, Appl. Phys. Lett. 74 (2002) 3368.
18. P. Yadoji, R. Peelamedu, D. Agrawal, R. Roy, Mat. Sci. and Eng.B 98 (2003) 269.
19. D. Agrawal, Journal of Materials Education 19 (1999) 49.
20. D.E. Clark, D.C. Folz, J.K. West, Mat. Sci. and Eng. A 287 (2000) 15.
21. C. Leonelli, P. Veronesi, L. Denti, A. Gatto, L. Iuliano, Journal of Materials Processing Technology 205 (2008) 489.
22. R.R. Menezes, P.M. Souto, R.H.G.A. Kiminami, J. of Mat. Proc. Tech. 190 (2007) 223
23. M Oghbaei and O Mirzaee, Journal of Alloys and Compounds 494 (2010) 175
24. Feldman, L. C. and Mayer, J. W., Fundamentals of Surface and Thin Film Analysis, North-Holland, New York, 1986, pp. 113– 123.
25. B. D. Cullity, Elements of XRD, 2nd Ed., Wesley Publishing Company (1978).
26. P. K. Kulriya, F. Singh, A. Tripathi, R. Ahuja, A. Kothari, R. N. Dutt, Y. K. Mishra, Amit Kumar and D. K. Avasthi, Rev. Sci. Instr. 78 (2007) 113901.
27. B. D. Cullity, Elements of X-ray Diffraction, 2nd. Ed., Addison-Wesley, reading, MA, p.102. (1978)
28. G. K. Williamson and W. H. Hall, Acta Metall. 1 (1953) 22
29. Terry L. Alford, Leonard C. Feldman and James W. Mayer, Fundamentals of Nanoscale Film Analysis, Springer Press (2007)
30. D. B. Williams and C. B. Carter, Transmission Electron Microscopy, A Textbook for Materials Science, Plenum (1996).
31. J.C.H. Spence, Experimental High-Resolution Electron Microscopy, 2nd edition, Oxford University Press (1988).

Chapter – III

Structural studies of Ge nanocrystals prepared by Atom Beam sputtering

3.1 Introduction

The structural, optical and electronic properties of low dimensional, indirect band gap materials have been investigated extensively over the past few years. When the crystallite size of these semiconductors is smaller than the exciton Bohr radius, carriers can be three-dimensionally confined and the properties of such semiconductor nanostructures embedded in dielectrics show very interesting and useful properties [1, 2]. Semiconductor nanostructures such as silicon (Si) and germanium (Ge) have been studied extensively because of their potential applications in optoelectronics and nanophotonics [3, 4].

The formation of quantum-dots with uniform size and with a high density embedded in a dielectric medium is an essential process for the device fabrication. Quantum-dot is a nano-scale crystal. Since the volume of nanocrystal is very small, there is three-dimensional confinement in a quantum-dot. Thus electrons and holes would be efficiently confined in the quantum-dot, and hence the high recombination rate and luminescence efficiency would be obtainable. Therefore, the optical, electrical and magnetism characteristics are different from those of bulk material. Besides, the density of states of quantum-dot varies with its dot size. One can alter the above-mentioned characteristics by varying the dot size. Si and Ge both are indirect band-gap materials. Ge has the lower energy band-gap, the smaller energy difference between the indirect and direct gaps, and the higher absorption coefficient. Compared with Si, Ge has the smaller electron and hole effective masses and the larger dielectric constant, which results in the larger Bohr radius. Thus, it is implied that Ge quantum-dots would appear more obvious quantum-confinement effect than the corresponding Si ones.

It was reported, based on comparison of Si and Ge effective masses and energy differences between the indirect gaps, that it should be easier to modify the electronic structure around the band gap of Ge [5]. Several techniques are being used to fabricate Ge nanocrystals, such as RF co-sputtering [6], DC sputtering [7], ion implantation [8], evaporation–condensation [9], electron beam evaporation [10], chemical vapour deposition [11] and pulsed laser deposition [12]. Atom Beam Sputtering (ABS) method has been used to prepare metal and semiconductor nanocrystyals. [13-16].

Rapid Thermal Annealing (RTA) is faster than furnace annealing because the ramping and cooling cycle takes place within few minutes compared to hours in furnace annealing. The special arrangements in RTA can significantly reduce wafer emissivity variation and temperature non-uniformities. Rapid thermal processing involving higher heating rates have long been used in the semiconductor industry as an alternative to the conventional furnace annealing. High temperature and short time annealing is of interest in the processing of thin-films in order to reduce unwanted diffusion during annealing and to minimize interaction between film and substrate. RTA has been shown to be very efficient method to synthesize nanocrystals of Si and Ge compared to the conventional furnace annealing [17, 18]. The ABS technique has already been used to prepare Ge nanocrystals by normal furnace annealing [19]. ABS has also been already used to prepare Ge nanoparticles in SiO_2 matrix and to compare the luminescence properties with samples prepared by ion implantation [20].

Researchers are looking for various synthesis methods in order to optimize structural and optical properties of nanocrtystals for diverse applications. The properties of nanocrystals are not only determined by its size but also by its shape, composition and structure. An appropriate method helps to make use of nanocrystals properties for a wide range of applications. The motivation of present work is to investigate the structure of the Ge nanoparticles grown by ABS and subsequent rapid thermal annealing process. Therefore, we have deposited Ge+SiO_2 composite films by ABS. Subsequently these films were subjected to RTA at various temperatures. We have also investigated the effects of Ge composition and annealing temperature on Ge nanocrystal size and strain. RTA results were compared with the furnace annealing. Besides this, the effects of Swift Heavy Ion (SHI) irradiation on Ge+SiO_2 composite

films have been discussed in detail. It is important to understand the mechanisms behind the formation of the nanocrystals in order to tailor material properties suitable for applications. The characterization was done by X-ray diffraction, Raman spectroscopy, Fourier Transform Infrared Spectroscopy (FTIR), and Transmission Electron Microscopy (TEM). RBS results of as-deposited and annealed films have also been discussed.

3.2 Experimental Details

The samples were prepared by the fast ABS method where small pieces of high purity Ge were placed on a SiO_2 target and co-sputtered by an argon atom source. Thin films of the mixture of Ge and SiO_2 were deposited on Si substrates. Thin films of Ge and SiO_2 nanocomposites with various Ge compositions of 6%, 16%, and 30% were prepared by co-sputtering of Ge and silica using 1.5 keV Ar atoms. The Ar atom source was mounted at an angle of 45^0 facing the sputtering target inside a vacuum chamber, as shown in Fig 2.1. The uniformity of the films was achieved by rotating the substrate with a DC motor. The beam delivered by the atom source was around 5cm in diameter when placed 10 cm away from the sputtering target. The source delivers a maximum current density of 30 $\mu A/cm^2$ on the target with a variable energy ranging from 0.8 to 2 keV. The variation of the semiconductor fraction in the films is determined by the relative area and sputtering rates of Ge and SiO_2.

These as-deposited samples were subjected to RTA in order to synthesize the Ge nanocrystals. As-grown samples were annealed using RXV6 RTP system (AET Thermal Inc) at 700 and 800^0C for 120s in N_2 atmosphere (2000 SCCM). Besides RTA, normal furnace annealing of the samples was also performed at 700 and 800^0 C in a quartz tube furnace in Ar + H_2 (5%) reducing atmosphere. The duration of annealing was kept constant for 30 min in all cases. The irradiation was performed using the 15UD Pelletron accelerator at Inter University Accelerator Centre (IUAC), New Delhi. The as-deposited samples were irradiated by 100 MeV Au^{8+} and 70 MeV Ni^{6+} ions with $1x10^{13}$ ions/cm^2 fluence. The ion beam current was maintained low (0.5–2 pnA) to avoid heating of the samples. The samples were kept at an angle of 5^0 with respect to the beam axis to avoid the channeling effect.

Raman scattering spectra of the films were obtained before and after annealing in backscattering configuration with a Renishaw Raman microscope using a 514.5 nm Ar+ laser excitation source. All the measurements were carried out at room temperature. X-ray diffraction measurements were carried out with CuKα x-ray, λ=0.154nm in a glancing angle incidence geometry. FTIR spectra were recorded using a Nexus 670 FTIR spectrometer in the wave number region 400–1500 cm^{-1} with a resolution of 4 cm^{-1}. RBS measurements were carried out using 2 MeV α-particles in a standard scattering chamber. It was pumped down to 5×10^{-6} torr by a turbo molecular pump before the starting of the measurements. The energetic α-particles were obtained from a 3MV Tandetron (HVEE, EUROPA). A Si surface barrier detector (Energy resolution of 15 keV) placed at a backward angle of 170^0 detected the scattered particles. The spectra were acquired on 8K-PC based MCA. RBS was used for the quantification of Ge composition in ABS films. RBS spectra were simulated by SIMNRA code.

3.3 RTA effects on Ge+SiO_2 films

3.3.1 Rutherford Backscattering spectrometry:

The Rutherford Backscattering Spectrum of the Ge+SiO_2 composite pristine sample has been shown in Fig.3.1. SIMNRA, a computer code was used to simulate the RBS spectra [21]. The estimated Ge composition in this film was around 32%. The thickness of the composite films is around 140 nm. These are in good agreement with the expected values.

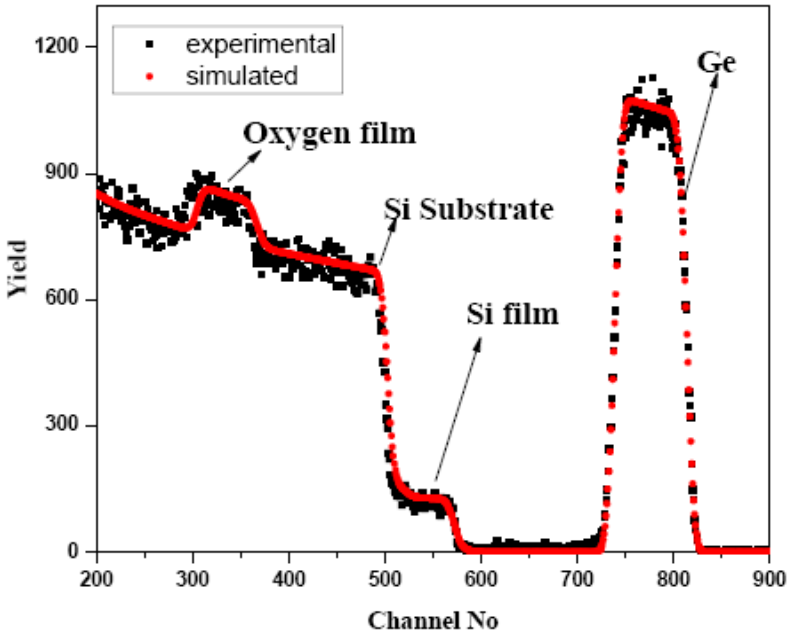

Fig.3.1: RBS spectrum of Ge as-deposited Set A sample

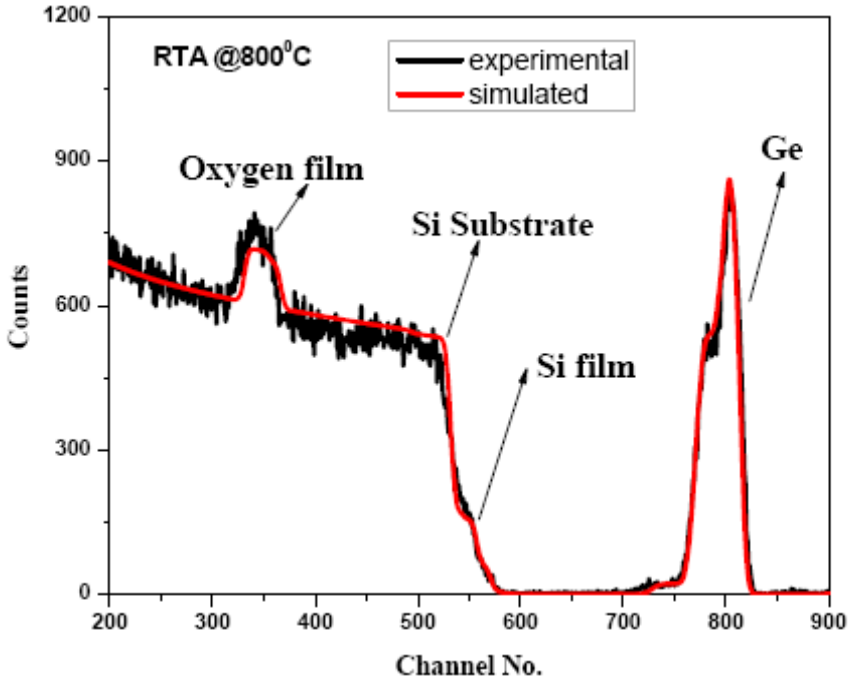

Fig.3.2: RBS spectrum of Ge annealed Set A sample at 800^{0}C

Fig. 3.2 shows the RBS spectrum of annealed sample at 800^{0}C. The Ge composition in this film is around 28%. For annealed sample at 800^{0}C, loss of Ge atoms has been observed. This is due to part of the Ge out-diffused or evaporated from the surface.

3.3.2 X-ray diffraction:

Set A and Set B samples are different in Ge composition embedded in SiO_2 matrix. The X-ray diffraction (XRD) spectra of set A as-deposited and rapid thermal annealed samples are shown in Figure 3.3. In the case of the as-deposited sample, no peak is observed, whereas the annealed samples at temperatures 700^0C and 800^0C show three peaks of Ge (111), (220) and (311) planes, which indicates the formation of nc-Ge [22].

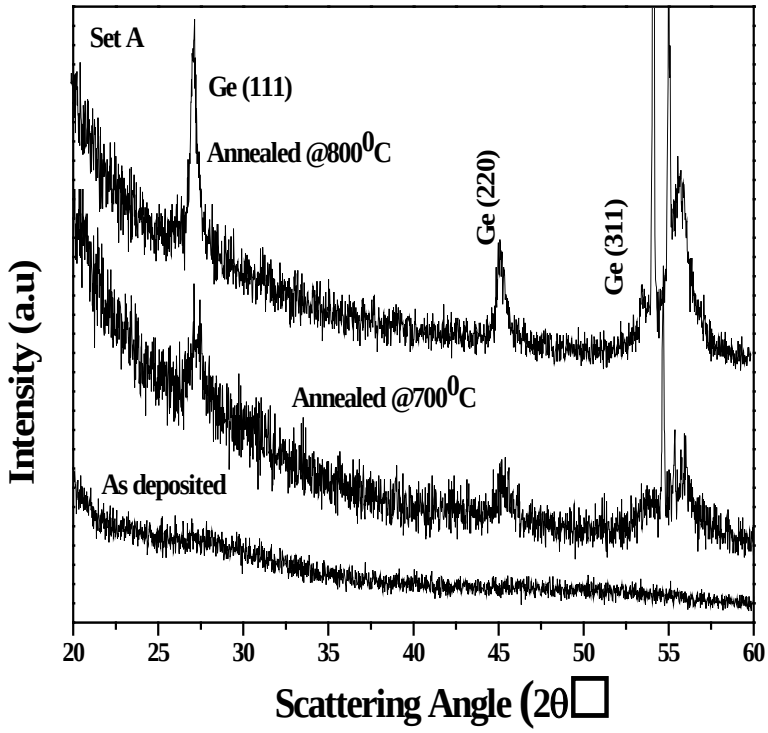

Fig. 3.3: GIXRD spectra of as-deposited and annealed samples of set A

As shown in Fig.3.3 the XRD peak becomes sharper and the full width at half-maximum (FWHM) of peak is reduced with the increase of annealing temperature. This indicates that the average size of nc-Ge increases with annealing temperature. On the other hand, XRD spectra of as-deposited and annealed samples at a given RTA temperature 800^0C with different Ge composition are shown in Fig 3.4. The average size of the nanoparticles is calculated using Scherrer's formula [23] given by

$$D = \frac{0.9\,\lambda}{\beta\, Cos\theta_B}$$

where λ is the wavelength of the X-ray source (*i.e,* 1.54A^0 for CuKα), β = FWHM (in radians) and θ_B is Bragg angle and D is the diameter of the nanocrystal.

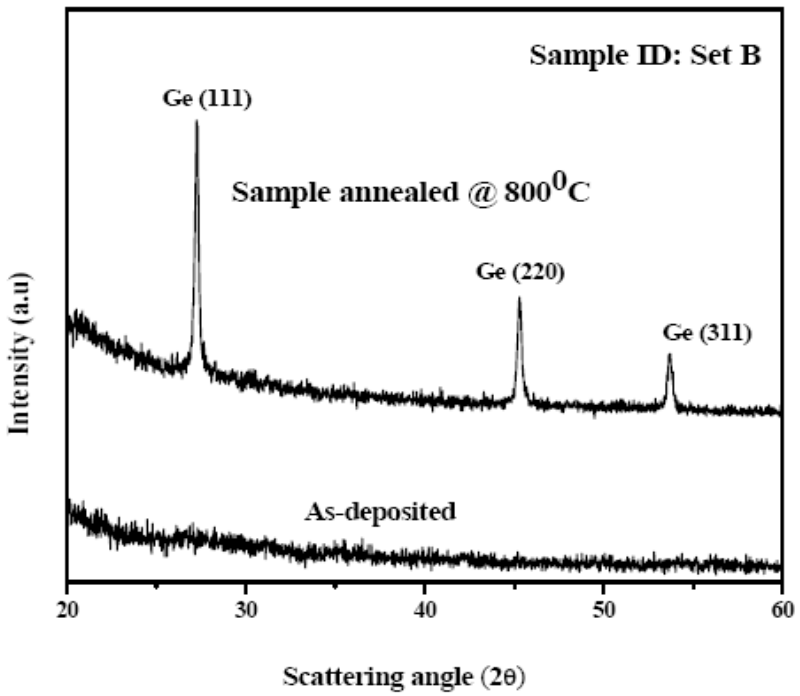

Fig. 3.4: GIXRD spectra of as-deposited and annealed samples of set B

The strain in the nanocrystalline Germanium samples is estimated using Williamson-Hall method. The Williamson-Hall equation [24] can be written as

$$\beta\, Cos\theta_B = [K\lambda/D] + [4\varepsilon\, Sin\theta_B]$$

Here K is the shape factor, λ is the X-ray wavelength, θ_B is the Bragg angle and D is the average crystallite size. Here ε is the root mean square value of the microstrain. Plotting the value of $\beta\, cos\theta_B$ as a function of $4sin\theta_B$ the microstrain ε may be estimated from the slope of the line.

We have plotted $\beta \cos\theta_B$ as a function of $4\sin\theta_B$ for samples annealed at different temperatures and for different Ge composition to calculate the microstrain. These plots have been shown in figure 3.5 and figure 3.6. The strain values are reported in the table-1 and 2. It increases with increase in Ge composition and with annealing temperature. The samples annealed at 700^0C and 800^0C indicate the average diameter of the nanocrystal is around 12 and 21 nm, respectively. Thus, the size of the nc-Ge increases with annealing temperature. This is in good agreement with the results reported in the literature [25].

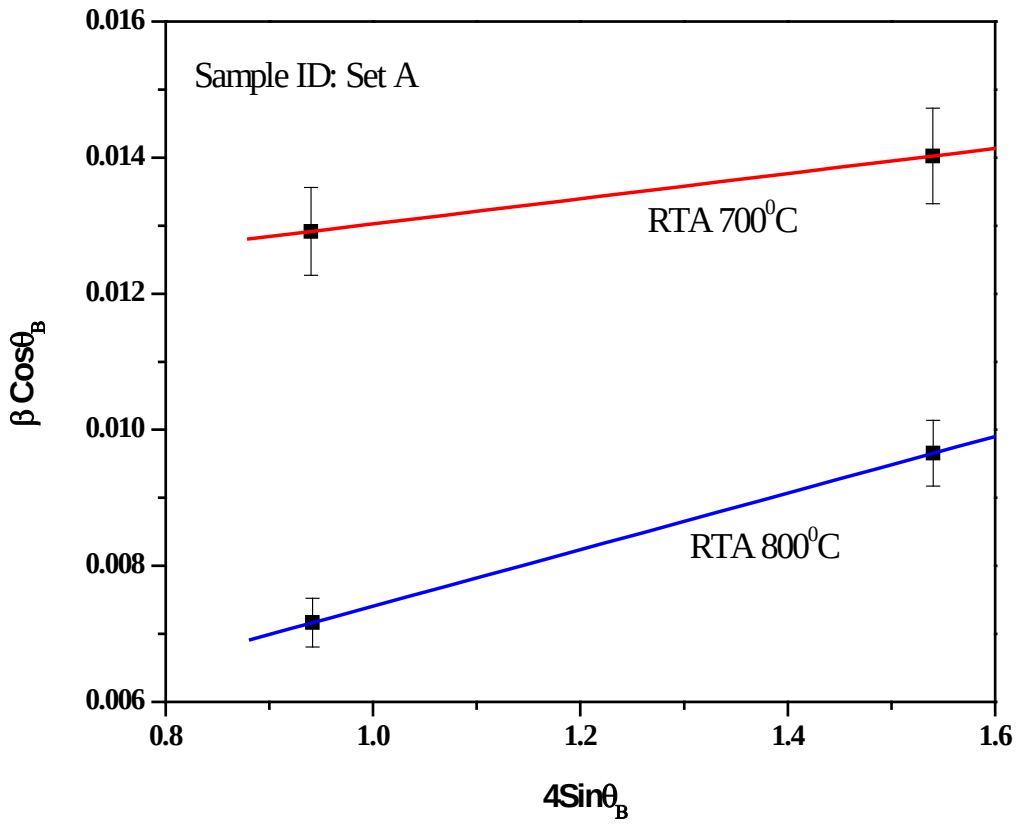

Fig. 3.5: Plot of $\beta \cos\theta_B$ as a function of $4\sin\theta_B$ annealed samples of set A

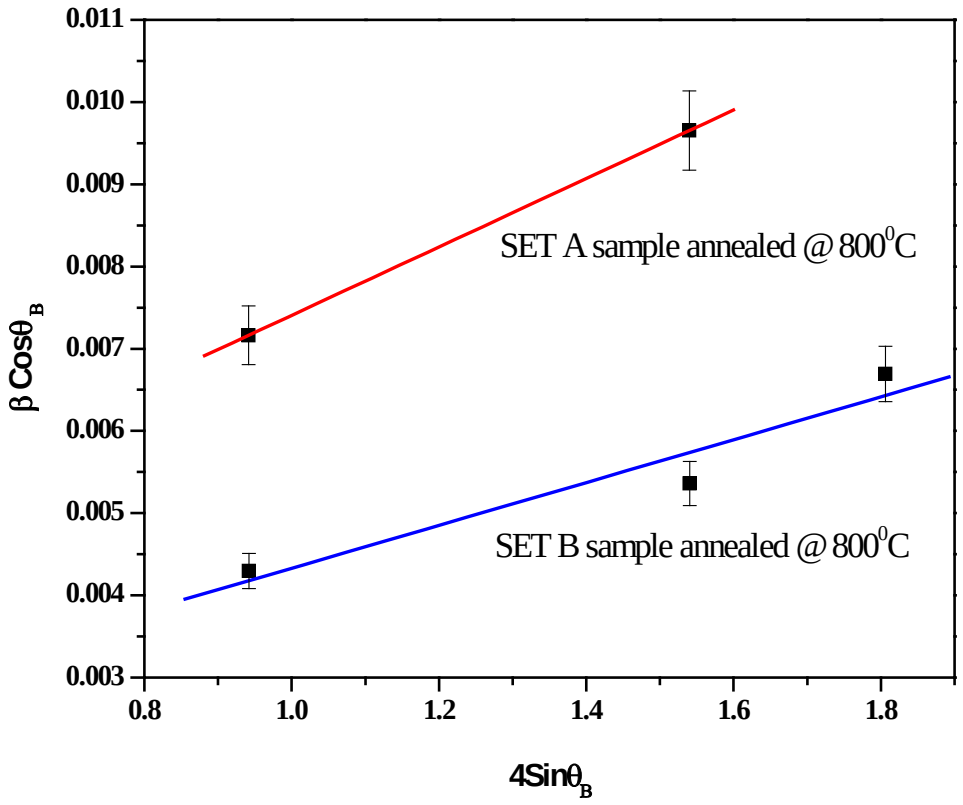

Fig. 3.6: Plot of $\beta \cos\theta_B$ as a function of $4\sin\theta_B$ annealed samples of set A and B

The crystallite size is increased with an increase in Ge composition at a given annealing temperature 800^0C. Here, the crystallize size is 21 and 32 nm in the set A and set B samples, respectively. Peak positions, d-spacing and strain values of all the peaks in XRD spectra are shown in Table 1 and Table 2.

Table 1: Lattice parameters, d spacing and strain values of Set A samples annealed at 700 and 800^0 C

Annealing Temp T (^{0}C)	Peak position	hkl	Inter planar spacing (d) (nm)	Lattice parameter (nm)	Crystallite Size (nm)	Micro-strain
700	27.19	111	0.327	0.567	12	1.83×10^{-3}
	45.28	220	0.200	0.565		
800	27.23	111	0.327	0.566	21	4.05×10^{-3}
	45.29	220	0.200	0.566		

Table 2: Lattice parameters, d spacing and strain values of Set A and Set B samples annealed at 800^0C

Annealing @ 800^0C	Peak position	hkl	Inter planar spacing (d) (nm)	Lattice parameter (nm)	Crystallite Size (nm)	Micro-strain
SET A	27.23	111	0.327	0.566	21	$4.05x10^{-3}$
	45.29	220	0.200	0.566		
SET B	27.24	111	0.326	0.566	32	$7.96x10^{-3}$
	45.29	220	0.199	0.565		
	53.70	311	0.170	0.565		

When the annealing temperature is higher, Ge atoms and small nanocrystals have higher mobility. Since nc-Ge crystallization temperature is lower than Ge melting temperature, Ge clusters and nanocrystals are formed by diffusion of Ge atoms or clusters inside the silicon oxide matrix. Therefore, an increase in annealing temperature leads to an increase of Ge crystallinity and crystallite size. Thus crystallinity improves with the annealing temperature as observed from decrease in FWHM and an increase in intensity from the XRD peaks.

3.3.3 Raman Spectroscopy:

Raman spectra of rapid thermally annealed samples have been shown in Fig 3.7. Raman spectra of all the samples show a shift in the peak position and an asymmetrical broadening on the lower frequency side when compared with the spectrum of the bulk Ge sample. The shift of the Raman band in thin films can arise due to tensile or compressive strain and phonon confinement. For the first order Raman spectrum, we have

$$I(\omega) \cong \int \frac{|C(0,\vec{q})|^2}{[\omega - \omega(\vec{q})]^2 + \left(\frac{\Gamma_0}{2}\right)^2} d^3\vec{q}$$

where ω (q) is the phonon dispersion relationΓand $_0$ is the natural line width (FWHM) of the scattered signal, and C (0, $q^{\rightarrow}$) is the Fourier transform of the phonon confinement, its value depend on the crystallite size. The as-deposited sample shows a broad Raman peak centered at 270 cm^{-1} which corresponds to amorphous Ge [26].

The appearance of sharp peak around 297 cm^{-1} for sample annealed at 700^0C indicates the initiation of crystallization process. The peak at ~299 cm^{-1} with FWHM ~6-7 cm^{-1} corresponds to Ge crystallites size around 10 nm. Raman spectra of the samples show a red shift in the peak position and an asymmetrical broadening when compared with the spectrum of the bulk Ge sample. This broadening of the Raman peak is attributed to phonon confinement [27].

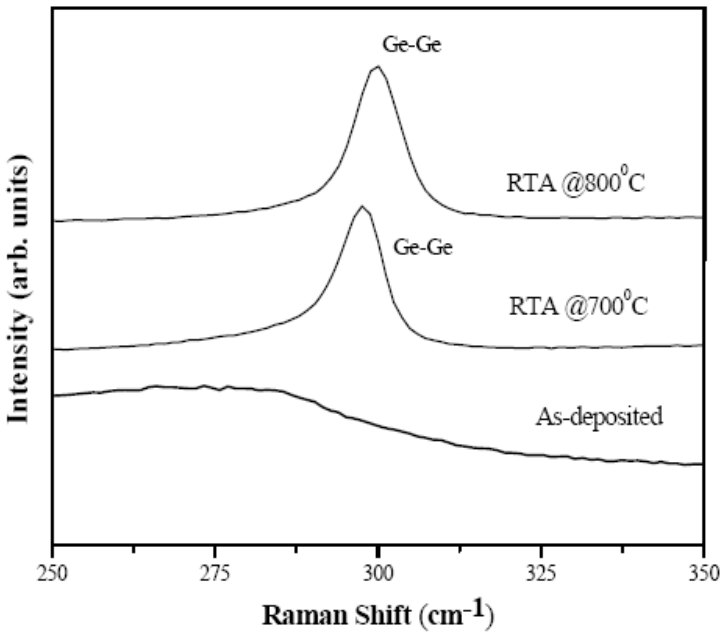

Fig.3.7: Raman spectra of Set A as-deposited and annealed samples

It has been reported that the diffusion of Ge in SiO_2 and nucleation of Ge depend upon the annealing temperature. In the present case, when the annealing temperature was 700^0C and above, the spectra show the formation of Ge nanocrystals due to nucleation of Ge atoms. Their diffusion and nucleation at surface as well as inside the matrix leads to the formation of nanocrystals. The various possibilities for formation of nanocrystals inside an insulating matrix by atom beam sputtering are diffusion of atoms or clustering of atoms that leads to the growth of nanoparticles. The ABS method is very simple and has better control over other ion beam methods like ion implantation and ion beam mixing. It is also economically more feasible than other ion beam synthesis techniques due to the use of a very low energy atom source (few keV) as compared with the ion implanter, which delivers ions of energies of ~100

keV. It is difficult to produce ion beams of all the elements in an ion implanter but Atom beam sputtering can sputter all the materials which are available in solid form.

3.4 Normal Furnace annealing effects on Ge+SiO_2 films:

3.4.1 Rutherford Backscattering spectrometry:

The Rutherford Backscattering Spectra of the ABS pristine samples have been shown in Fig.9 and Fig.10. The estimated Ge compositions in these films were 6% and 16% respectively. These are in good agreement with the expected values. We found that the thickness of deposited film is around 100 nm.

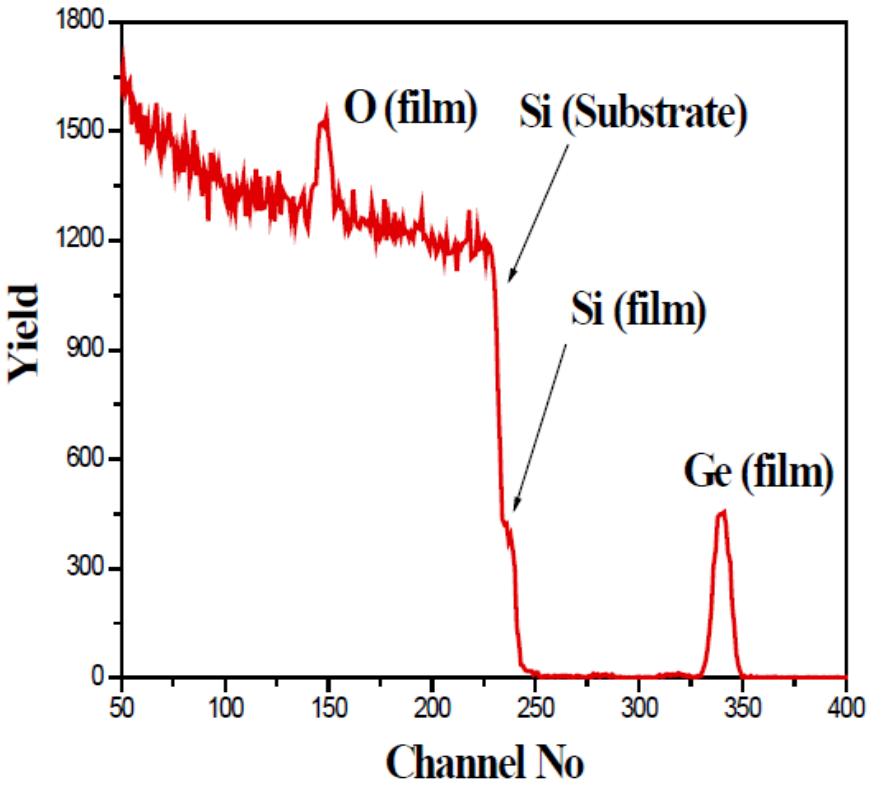

Fig.3.8: RBS spectrum of Ge 6% as-deposited sample

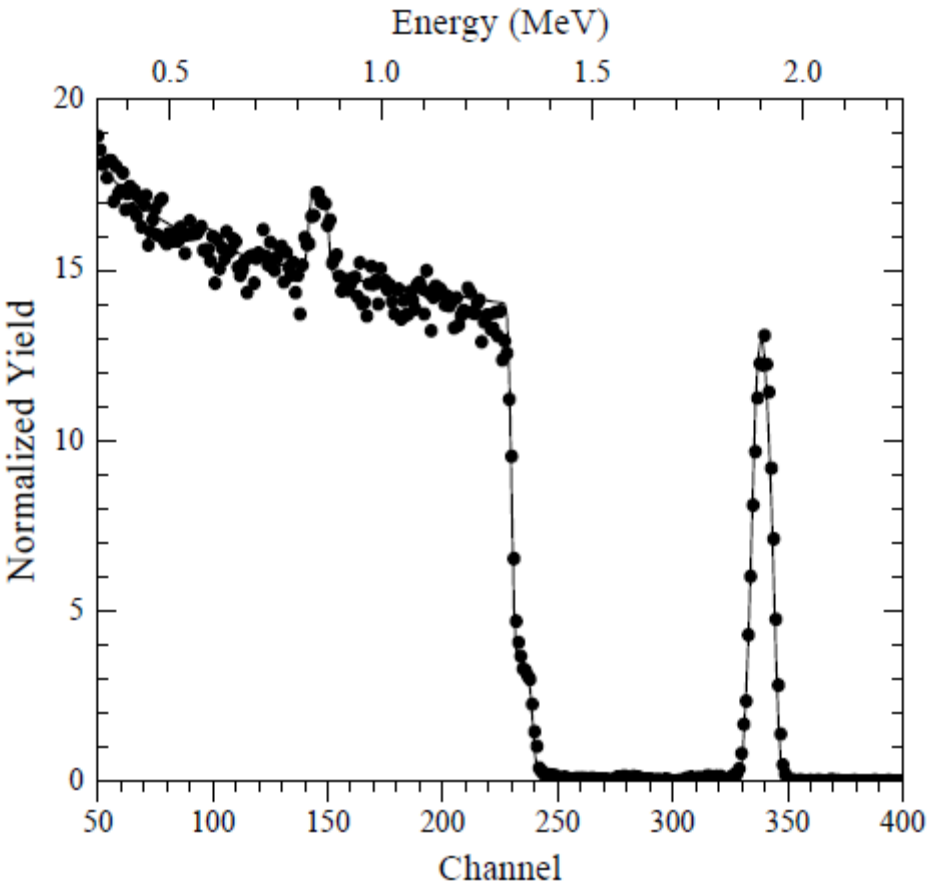

Fig.3.9: RBS spectrum of Ge 15% as deposited sample

3.4.2 Raman Spectroscopy:

It is known that the Raman spectra of Si wafer have similar line shapes comparable to Ge nanoparticles. Particularly the mode observed around 300 cm^{-1} from the Si wafer is identified as two-phonon TA modes of Si which overlaps with the single-phonon LO mode of Ge [28-30].

To remove the contribution of the Si peak, first Si wafer's Raman spectrum was recorded which showed a weak signal around 300cm^{-1}. Now the Raman spectrum was recorded from the Ge+SiO_2 composite film on Si wafer. After subtracting the Si peak contribution, we observe a high intensity peak which is attributed to Ge in the films. The entire spectrum has been shown in Fig 3.10.

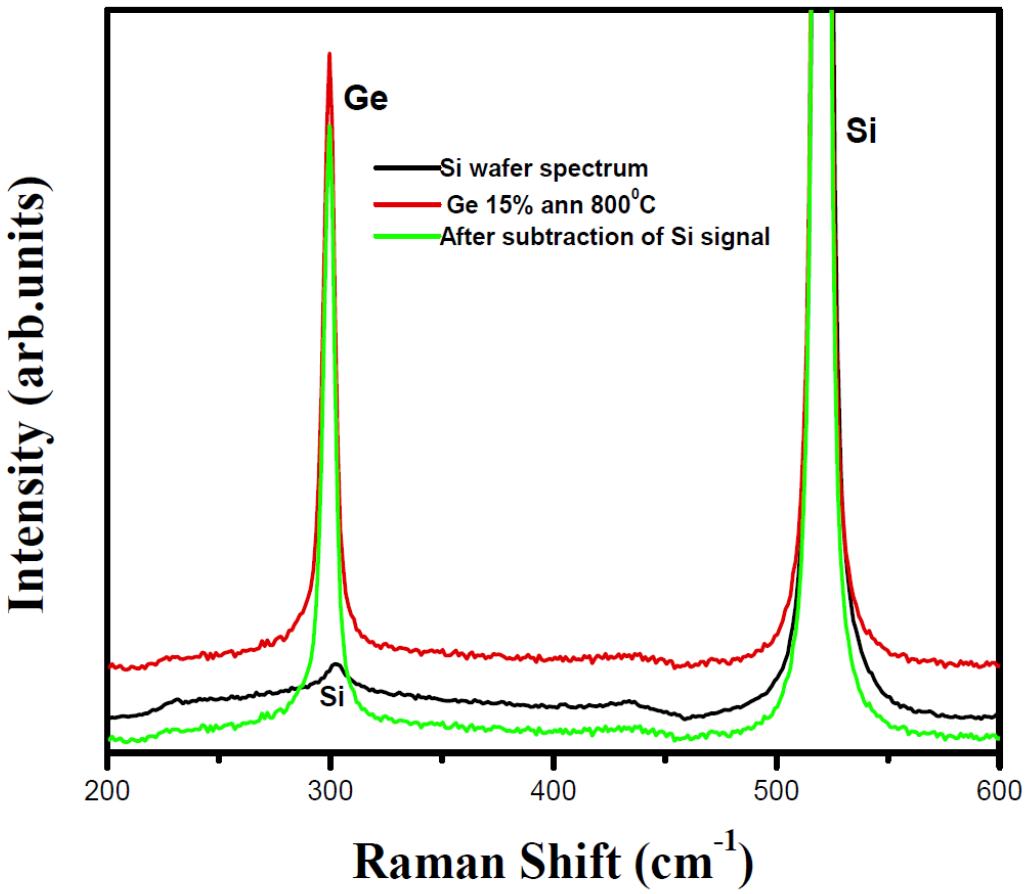

Fig.3.10: Raman Spectra of Si wafer, Ge+SiO_2 composite annealed at 800^0C and Ge+SiO_2 composite after removing the Si contribution

Figs.3.11 and 3.12 show the Raman Spectra of the as-deposited, 700 and 800^0 C annealed samples of 6% and 15%. For the as-deposited samples, we observed very low intensity of Ge peak around 300 cm^{-1} indicating early stage of Ge formation. For higher concentrations it is replaced by a broad hump around 270 cm^{-1} indicating the presence of amorphous Ge. The integrated intensity of the mode at 300 cm^{-1} is found to increase as a function of annealing, supporting our argument that the mode is from Ge and not the 2-TA phonon of Si substrate.

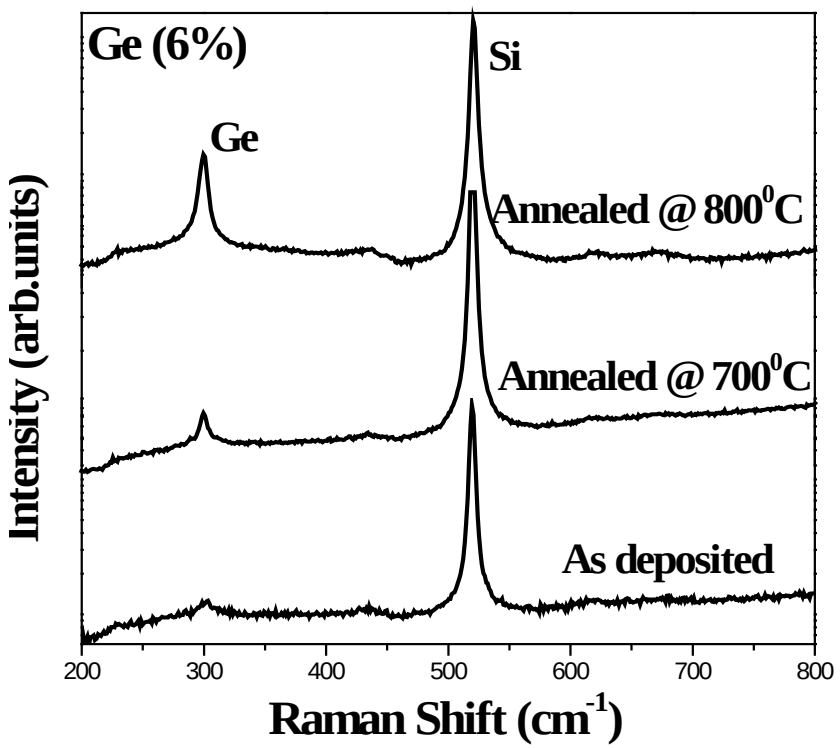

Fig.3.11: Raman spectra of Ge 6% as-deposited and annealed samples

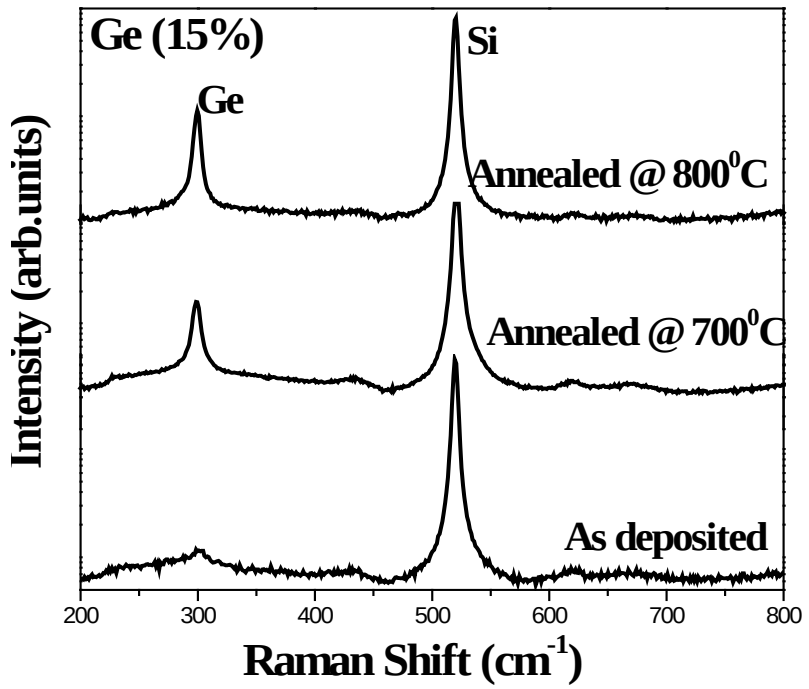

Fig.3.12: Raman spectra of Ge 15% as-deposited and annealed samples

The Raman modes around 410 and 480 cm^{-1} correspond to the Ge-Si and Si-Si local optical phonon modes respectively. The sharp peak position at 521 cm^{-1} is from the TO/LO phonon of the c-Si substrate. The peak around 300 cm^{-1} from annealed films appears asymmetric in the low-frequency region which is due to the smaller size of the Ge particles. The position of the Ge mode red shifts (~3 cm^{-1}) to lower frequency upon annealing for 6% and 15% samples.

3.4.3 X-ray diffraction:

Fig.3.13 shows the XRD patterns of the as-deposited and annealed films as indicated. No Ge peak is observed from the as-deposited films while high temperature annealing results in a broad Ge (311) peak [30, 31]. XRD spectra of Ge 15% have been shown in Fig 16. In few cases Ge (111) around 27.3^0 and GeO_2 peak around 26.5^0 (Fig.15) are observed.

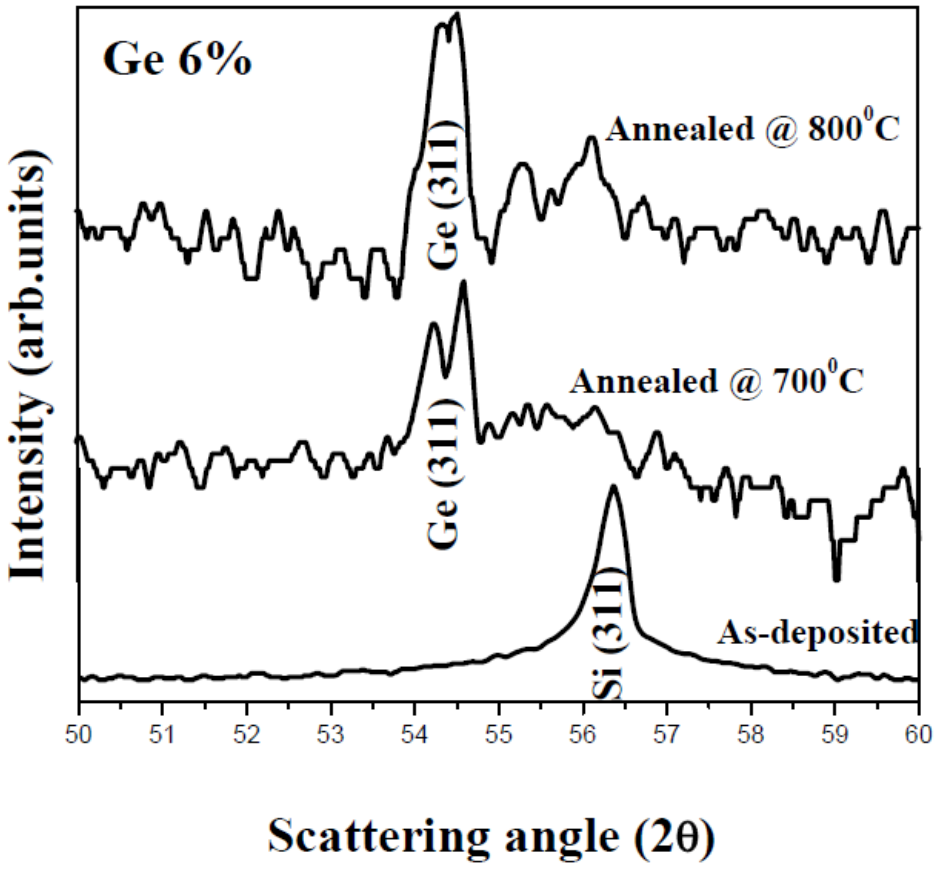

Fig.3.13: GIXRD of Ge 6% as-deposited and annealed

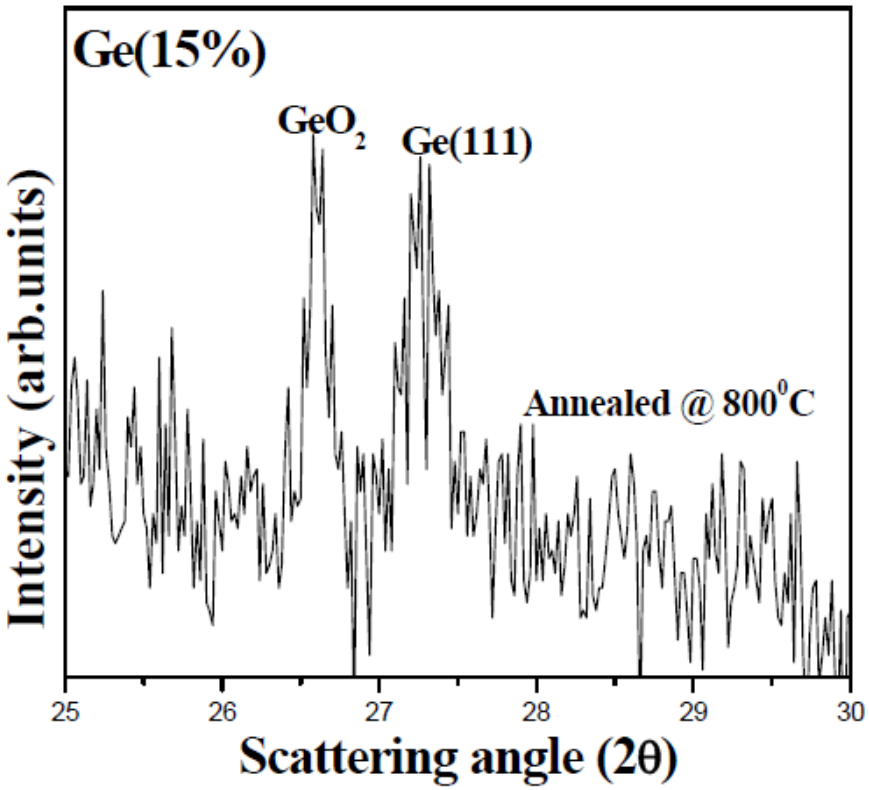

Fig.3.14 GIXRD of Ge 15% annealed sample at 800^0C

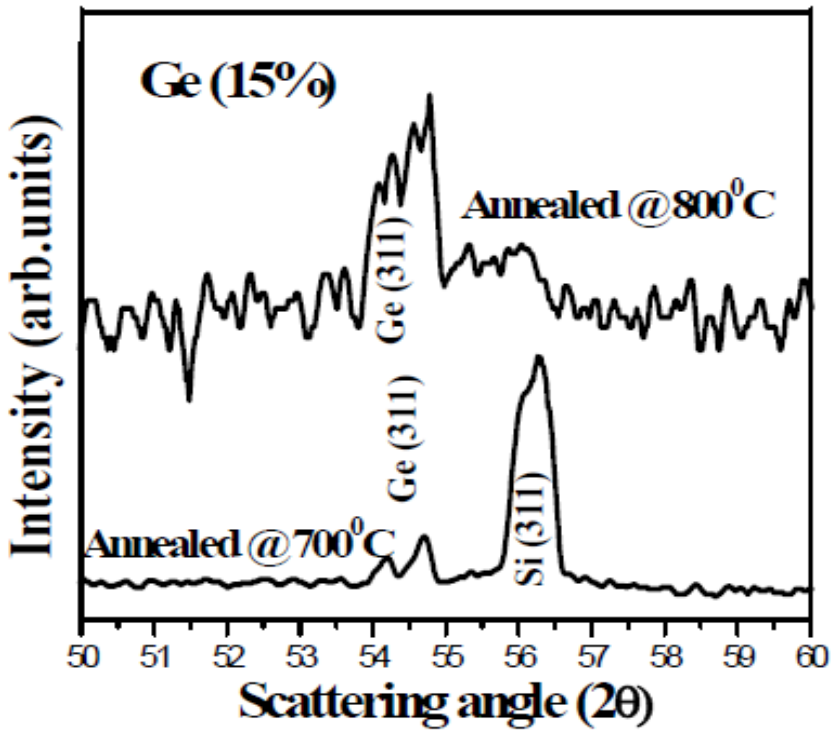

Fig.3.15 GIXRD of Ge 15% as-deposited and annealed

3.5. Irradiation effects on Ge+SiO_2 films:

3.5.1 Raman Spectroscopy:

The position of Ge mode for as-deposited 30% sample is observed around 270 cm^{-1} which is blue shifted to higher frequency upto ~300 cm^{-1} (Fig. 3.18) upon annealing. The peak around 300 cm^{-1} is due to confinement of phonons in Ge nanocrystals [32, 33]. A comparison with the existing literature, the width of the Ge mode indicates a particle size of 10 – 15 nm [34]. The Ge mode observed in the as-deposited sample for lower concentrations is a clear evidence for the crystalline Ge phase formation in the matrix. This is an advantage of the ABS technique over other room temperature preparation techniques like rf-sputtering where formation of crystalline Ge has not been observed [35-37].

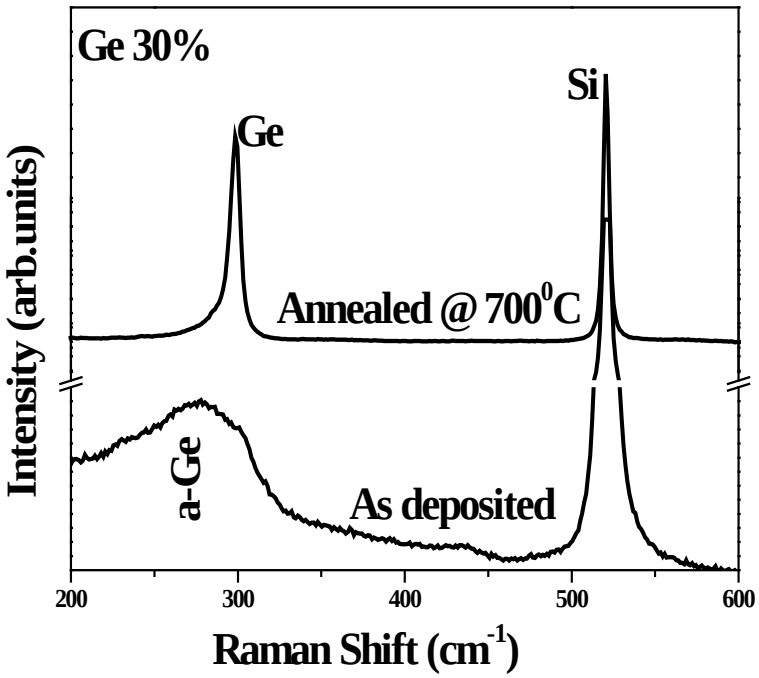

Fig.3.18 Raman spectra of Ge 30% as-deposited and annealed samples

The Raman spectra of Ge 30% for as-deposited and irradiated sample with 100 MeV Au and 70 MeV Ni ions with a fixed fluence $1x10^{13}$ ions/cm^2 were shown in Fig 3.19. The electronic energy loss of Au and Ni ions in Ge are about 17 and 11 keV/nm respectively. The Ni irradiated sample shows a broad peak around 300 cm^{-1} which may be due to combination of crystalline and amorphous signal.

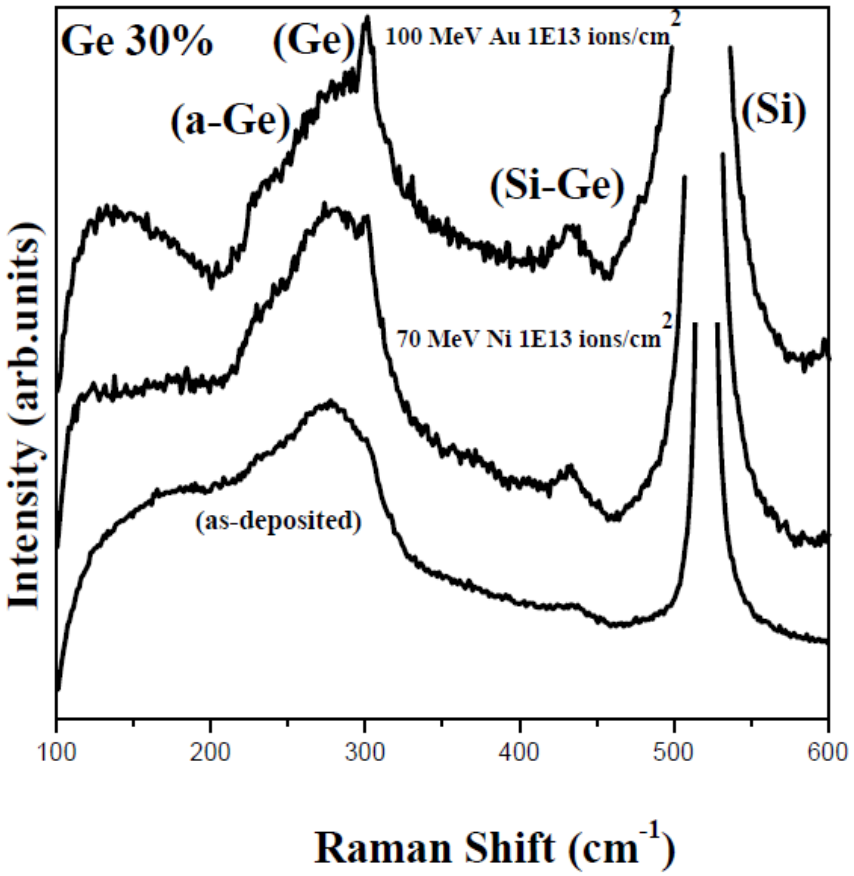

Fig.3.19: Raman spectra of Ge 30% as-deposited and irradiated sample.

The Au irradiated sample shows a sharp peak around 300 cm^{-1} which corresponds to the crystalline Ge with shoulder at low frequency around ~270 cm^{-1} corresponds to the amorphous Ge. Due to high electronic energy loss (in the case of 100 MeV Au irradiation case ~17 keV/nm), we could see the sharp crystalline peak as well as amorphous peak in the Au irradiated sample. This is in contrast to the annealing results where only sharp crystalline Ge mode was seen and no signal of amorphous Ge was observed. The Raman spectrum of irradiated sample is comparable with that of the samples prepared by implantation and rf-sputtering and subsequent high temperature annealing [38, 39].

3.5.2 Fourier Transform Infrared Spectroscopy (FTIR):

FTIR spectra of samples as a function of annealing and irradiation are shown in Fig.3.20 and Fig.3.21 respectively. The structure of amorphous GeO_2 can be described as $Ge\text{-}Ge_yO_{4-y}$ tetrahedral connected by bridging oxygen atoms. The asymmetric stretching vibration mode of Ge-O-Ge in stoichiometric GeO_2 is at $885cm^{-1}$. The vibration frequency of oxygen deficient structures, for y = 0 to 4 changes linearly from 885 to $740cm^{-1}$ according to the empirical equation [40], $\nu(x) = 72.4x+743\ cm^{-1}$, where x is the oxygen content that ranges from two to zero. In the case of as-deposited films Ge-Ge mode was also observed (~$740\ cm^{-1}$) along with Si-O-Ge and GeO_2 vibrational modes around 1020 and $840\ cm^{-1}$ respectively [41-42].

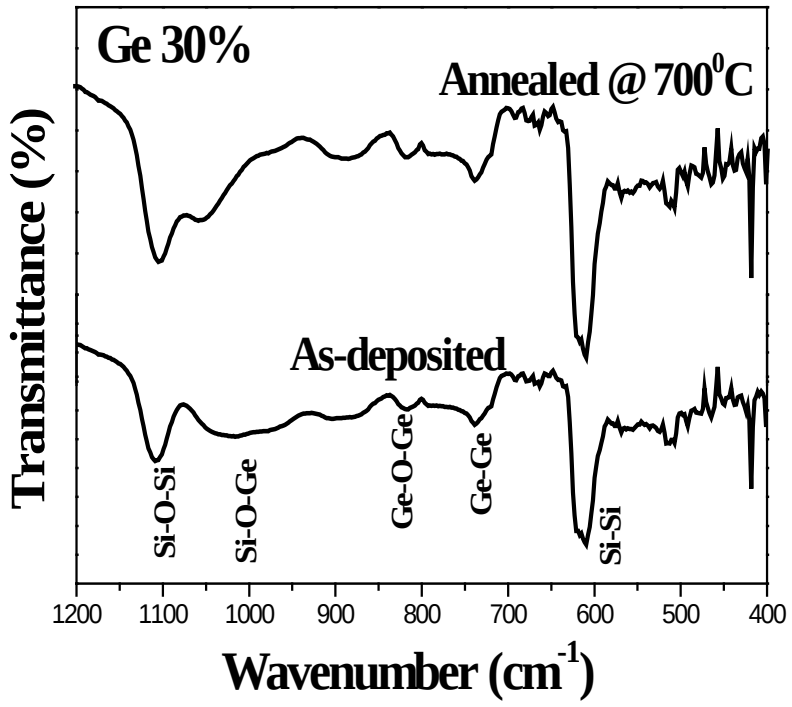

Fig.3.20: FTIR spectra of Ge 30% as-deposited and annealed

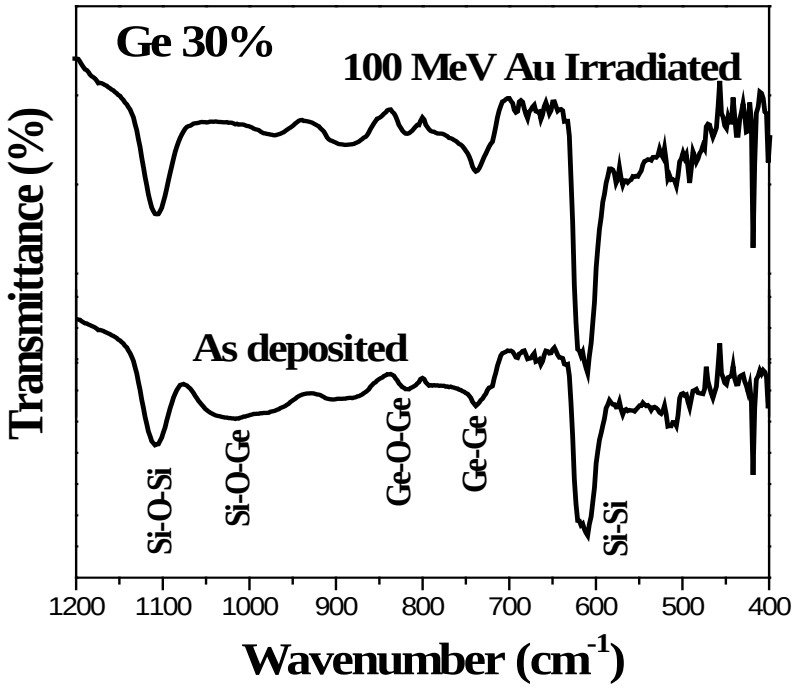

Fig.3.21: FTIR spectra of Ge 30% as-deposited and irradiated.

Upon reducing atmosphere annealing the Si-O-Ge mode merges with the Si-O-Si asymmetric stretching mode (~1108 cm^{-1}). Moreover the Si-O-Si mode sharpens which indicates the densification of the SiO_2 matrix. The stretching mode of Si-Si is observed around 614 cm^{-1} becomes sharper upon annealing. Apart from Ge-Ge, Si-Si peak also became sharp. At the higher temperature it is possible to diffuse Si atoms from substrate to matrix. In the case of irradiation the Si-O-Ge mode has totally vanished and the Ge-Ge mode becomes intense and sharper. This may be due to either diffusion of Si or reduction of oxygen content in the film or both. These observations are consistent with the Raman studies.

When an energetic ion interacts with a solid, it undergoes a series of collisions with the atoms and electrons in the target. In these collision processes incident ion losses energy ranging from few to 100 keV/ nm depending upon the energy, mass, and density of the target. The energy loss rate dE/dx of an energetic ion moving through a solid is determined by screened Coulomb interactions with the substrate atoms and electrons. Ion losses its energy through two major processes i.e. nuclear or elastic collisions, in which energy is transferred to a target atom as a whole and electronic collisions, in which the moving particle energy is used in exciting or ejecting the

atomic electrons of the target. Electronic collisions involve negligible deflection of the ion trajectory, and lattice disorder. When the projectile velocity v is much greater than that of an orbital electron, the influence of the incident particle on an atom (as a whole) may be considered as a sudden, small external perturbation. But the collision produces a sudden transfer of energy from the projectile to the target electrons. The stopping cross section increases with decreasing velocity because the particle spends more time in the vicinity of the atom, with slowing down. The deposition of energy into the film is predominantly through electronic energy loss. This energy deposition leads to crystallization similar to that of thermal crystallization and can be considered as the crystallization induced by thermal spikes. One can explain the basic mechanism of recrystallization and formation of nanocrystals in these samples, under ion-irradiation with the help of thermal spike theory [43]. When the swift heavy ion passes through the material the energy is transferred to the target lattice via electron–phonon coupling. It is known from the work of Meftah *et al.* [44] and Toulemonde *et al.* [45] that a track diameter of about 10 nm is created for a *Se* value of ∼11 keV/nm in silica. This large amount of energy is transferred to the target electrons in very short time, of the order of $\sim 10^{-12}$ seconds which leads to an increase of the lattice temperature above its melting point along the ion track. The temperature along the ion path goes to very high value which is sufficient to crystallize the Ge, which is embedded in Silica. This results in a modification of structure of films around the cylindrical zone and crystallization of the films.

3.6 Conclusions:

In conclusion, atom beam co-sputtering deposition technique followed by RTA has been used to synthesize Ge nanocrystals embedded in SiO_2 matrix. As-deposited and annealed samples were characterized by using XRD and Raman spectroscopy. The Ge modes of annealed samples in the Raman spectra show a red shift in the peak position and an asymmetrical broadening indicates the existence of crystalline Ge. The XRD results reveal that annealing leads to nanocrystal formation. Ge composition and film thickness were measured using RBS and possible reduction in Ge composition after annealing was also discussed. The variation of crystallite size as a function of RTA temperature and advantages of ABS method have been highlighted. The structural properties and size of nanocrystals strongly depend on RTA temperature and Ge

composition. The Ge modes in the Raman spectra of annealed samples are sharp indicating the existence of crystalline Ge, whereas the in the spectra of irradiated samples, the sharp mode was observed with a broad shoulder peak indicating the existence of both amorphous and crystalline phases of Ge. The XRD shows broad Ge (311) peak in all the cases and GeO_2 and Ge (111) peak in some cases. The FTIR complements the Raman results as a function of annealing the Si-O-Ge mode merges with the Si-O-Si stretching mode. The Si-O-Si mode becomes sharper upon annealing indicating densification of the matrix. The Si-O-Ge mode vanishes upon irradiation and more intense and sharp Ge-Ge mode has been observed. The possible mechanism for irradiation induced crystallization is discussed. It has been highlighted that ABS is a suitable technique to grow Ge nanoparticles embedded in SiO_2 matrix. The results have been compared with the other growth methods like sputtering and implantation. Eventually, it is possible to tune the properties of nanocrystals by changing the various pre and post deposition parameters in order to use them for different applications.

3.7 References:

1. K S Zhuravlev, A M Gilinsky and Kobitsky A Yu, Appl.Phys. Lett. 73 (1998) 2962
2. S H Choi and R G Elliman, Appl. Phys. Lett. 75 (1999) 968
3. L T Canham, Appl. Phys. Lett. 57 (1990) 1046
4. L Pavesi et al Nature 408 (2000) 440
5. Y Maeda, Phys. Rev. B 5 (1995) 1658 .
6. P Caldelas, A G Rolo , A Chahboun A, S Foss, S Levichev, T G Finstad, M J M Gomes, O Conde, Journal of Nanoscience and Nanotechnology 8 (2008) 572
7. M Zacharias, P M Fauchet. J Non-Cryst Solids 227–230 (1998) 1058.
8. S N M Mestanza, E Rodriguez and N C Frateschi, Nanotechnology 17 (2006) 4548
9. A Stella, P Tognini, C E Bottani, P Milani, P Cheyssac, R Kofman. Thin Solid Films 318 (1998) 100
10. W Wan, C L Lin, N L Zhang, W L Liu, G Yang, T H Wang. Appl Phys Lett 82 (2003) 3162

11. Z He , J Xu , W Li, K Chen, D Feng . J Non-Cryst Solids 266–269 (2000) 1025.
12. Y Zhu, P P Ong. J Phys Condens Matter; 13 (2001) 4075.
13. D. Kabiraj, S.R. Abhilash, L. Vanmarcke, N. Cinausero, J. C. Pivin and D. K. Avasthi, Nucl. Inst. and Meth. B 244 (2006) 100.
14. D. K. Avasthi, Y. K. Mishra, D. Kabiraj, N. P. Lalla and J. C. Pivin, Nanotechnology 18 (2007) 125604.
15. Y. K. Mishra, S. Mohapatra, Rahul Singhal, D. K. Avasthi, D. C. Agarwal, S. B. Ogale, Appl. Phys. Lett. 92 (2008) 043107
16. S. Mohapatra, Y. K. Mishra, D. Kabiraj, D. K. Avasthi, J. Ghatak, S. Verma, Appl. Phys. Lett. 92 (2008) 103105.
17. F. Roozeboom_Ed.., Advances in Rapid Thermal and Integrated Processing, Kluwer Academic Publisher, 1996
18. O. Adeoya, M. Hage Ali, J.C. Muller, P. Siffert, Appl. Phys. Lett. 50, (1987) 1736.
19. N. Srinivasa Rao, S. Dhamodaran , A.P. Pathak , P.K. Kulriya , Y.K.Mishra , F. Singh, D. Kabiraj , J.C. Pivin , D.K. Avasthi. Nucl. Inst. Meth B 264 (2007) 249
20. A Sigha, A Roy, D Kabiraj and D Kanjilal, Semicond. Sci. Technol. 21 (2006) 1691.
21. M. Mayer, Report IPP 9/113, Max–Planck-Institut für Plasmaphysik, Garching, Germany, 1997.
22. X M Wu, M J Lu, W G Yao, Surf. Coat. Technol. 161 (2002) 92.
23. B. D. Cullity, Elements of X-ray Diffraction, 2nd. Ed., Addison-Wesley, reading, MA, p.102. (1978)
24. G. K. Williamson and W. H. Hall, Acta Metall. 1 (1953) 22
25. M. J. Lu, X. M. Wu, W. G. Yao, Materials Science and Engineering B, 100 (2003) 152
26. Y. Sasaki and C. Horie, Phys. Rev. B 47 (1993) 3811
27. P. M. Fauchet, I.H. Campbell, Crit. Rev. Solid State Mater. Sci. 14 (1988) S79
28. A V Baranov, A V Fedorov, T S Perova, R A Moore, S Solosin, V Yam, D Bouchier and V Le Thanh. J. Appl. Phys. 96 (2004) 2857.

29. A V Baranov, A V Fedorov, T S Perova, R A Moore, V Yam, D Bouchier, V Le Thanh and K Berwick. Phys. Rev. B73 (2006) 75322.
30. V Ng, S P Ng, H H Thio, W K Choi, A T S Wee and Y X Jie, Mater. Sci. Eng. A 286 (2000) 161.
31. X M Wu, M J Lu, and W G Yao, Surface Coatings and Technology 161 (2002) 92.
32. C. E. Bottani, C. Mantini, P. Milani, M. Manfredini, A. Stella, P. Tognini, P. Cheyssac, and R. Kofman, Appl. Phys. Lett. 69 (1996) 2409.
33. N Srinivasa Rao, A P Pathak, N Sathish, G Devaraju, V Saikiran, P K Kulriya, D C Agarwal, G Sai Saravanan and D K Avasthi Solid State Communications 150 (2010) 2122
34. X.L. Wu, T. Gao, X.M. Bao, F. Yan, S.S. Jiang and D. Feng, J. Appl. Phys. 82 (1997) 2704
35. T.V. Torchynska , A.Vivas Hernandez , A.V. Kolobov, Y. Goldstein, E. Savir and J. Jedrzejewski, J. of Electron Spectroscopy and Related Phenomena 137–140 (2004) 619
36. W.K.Choi, Y.W.Ho, S.P.Ng, and V.Ng, J. Appl. Phys. 89 (2001) 2168.
37. V Baranov, A V Fedorov, T S Perova, R A Moore, S Solosin, V Yam, D Bouchier and V Le Thanh. J. Appl. Phys. 96 (2004) 2857
38. Y.M. Yang, X.L. Wu, L.M. Yang, G.S. Huang, T. Qiu, Y. Shi, G.G. Sui, P.K. Chu, J. Appl. Phys. 99 (2006) 14301.
39. M. Yamamoto, T. Koshikawa, T. Yasue, H. Harima, K. Kajiyama, Thin Solid Films 369 (2000) 100
40. S Witanachchi, and P J Wolf. J. Appl. Phys. 76 (1994) 2185.
41. M I Ortiz, A Rodriguez, J sangrador, T Rodriguez, M Avella, J Jimenez and C Ballesteros, Nanotechnology 16 (2005) S197.
42. E W H Kan, W K Choi and W K Chim, J. Appl. Phys. 95 (2004) 3148.
43. M. Toulemonde, C. Dufour, E. Paumier, Phys. Rev. B 46 (1992) 14362
44. A Meftah, F. Brisard, M. Costantini et al., Phys. Rev. B 49 (1994) 12457
45. M. Toulemonde, J.M. Costantini, Ch. Dufour et al., Nucl. Instrum. Methods B 116 (1996) 37.

Chapter – IV

Crystallization of RF sputtered Ge embedded SiO_2 films by microwave annealing and ion irradiation

4.1 Introduction:

Nanocrystals and quantum dots are nanometer-scale semiconductor structures that represent one of the most intensively developing areas of modern semiconductor physics. The optical, magnetic, electronic and mechanical properties of materials are beginning to be modified using nano-scale structures. Semiconductor nanocrystals exhibit size-tunable optical and electronic properties that are of interest in solid state lighting, sensors and other electronic and optoelectronic devices. In semiconductor nanocrystals the excitons are confined in all three spatial dimensions. As a result, they have different properties than those of bulk semiconductors. Besides, the surface electronic states also affect both electronic and optical properties of semiconductor nanocrystals due to large surface-to-volume ratios [1–3]. For these reasons, enormous amount of research effort has been put worldwide, to synthesize and study these materials.

Si and Ge nanocrystals embedded in a dielectric matrix have been demonstrated as potential candidates for the fabrication of optoelectronic, photovoltaic and nonvolatile memory devices [4–6]. The formation of Ge nanocrystals is easier of its lower melting point although there are numerous reports on Silicon (Si) nanocrystals, In addition to the ease in fabrication the quantum confinement is expected to appear more prominent for Ge than Si, because the Bohr exciton radius of the Ge is higher than Si [7-8]. There are three major phenomena induced when the size of a material is scaled down to the order of nanometers. Confinement of carriers and phonons, surface related phenomena, and phase transformation. One of the attractive features of Ge nanocrystals is visible light emission. Like Si, bulk Ge with an indirect bandgap is less attractive for light

emitting device applications. However, many photoluminescence colors have been observed from Ge nanocrystals. The Ge nanocrystals embedded in SiO_2 have been the most intensively studied because of good confinement of the electrons with a large potential barrier of the oxide. The size of the Ge nanocrystal can be controlled by the composition of Ge and annealing temperature. Different annealing techniques have been used for synthesis of Ge nanocrystals such as furnace annealing [9-10] and rapid thermal annealing [11]. Rapid thermal annealing (RTA) has been shown to be very effective in increasing the growth or the recrystallisation rate of Si and Ge compared to the conventional furnace annealing [12]. In spite of all this, researchers are looking for more compact and clean synthesis methods for various industrial applications. In addition to above annealing methods, microwave annealing is also one of the good techniques for synthesizing nanocrystals having its own advantages.

In addition to this, ion beam induced crystallization of materials has attracted enough interest in the recent years. Several such studies have been carried out on amorphized Si and implanted samples [13-16]. This important phenomenon of ion beam induced crystallization has been demonstrated using both, low energies as well as swift heavy ions [17]. Already Si nanocrystals embedded in SiO_2 [18-20] and Ge nanocrystals embedded in GeO_2 [21] matrix have been prepared by ion irradiation. Atom beam sputtering (ABS) is used to prepare Ge nanocrystals [22-23] and it has also been used to synthesize metal–polymer nanocomposites for optical applications and to study the controlled growth of gold nanoparticles by ion irradiation [24-25]. Crystallization of Ge implanted SiO_2 films by swift heavy ion irradiation was too reported [26]. Effect of ion irradiation on already prepared Ge nanocrystals has also been studied [27].

In the present chapter, we report the synthesis of Ge nanocrystals by microwave annealing and ion irradiation to discuss their relative importance. The structure of the films synthesized by microwave annealing has been evaluated by XRD and Raman spectroscopy. Surface morphology of the films was studied by AFM. Specifically, we demonstrate relative effects of microwave annealing and swift heavy ion irradiation of $Ge+SiO_2$ films deposited by RF magnetron sputtering. The samples were characterized by transmission electron microscopy (TEM), X-

ray diffraction, Raman spectroscopy and atomic force microscopy (AFM). Here we present TEM image of the formed nanocrystal that provides direct evidence of the nanocrystal formation. The characterization results obtained by using various techniques are consistent and have been discussed in detail.

4.2 Experimental Details

The composite thin films were prepared by the RF-magnetron sputtering technique with a composite target of Ge of purity 99.999% (2 inch in diameter) and several SiO_2 pieces (the purity is 99.999%) chips were attached on the top of Ge target. The films were deposited on (1 0 0) oriented p-type Si substrates. Prior to deposition, the substrates were cleaned in alchohol and acetone. Eventually, substrates were rinsed with a large amount of de-ionized water, dried in hot air and immediately placed into the chamber. In situ Ar pre-sputtering of the target was performed in order to clean it and remove any oxide on the surface of the target. After vacuum pumping, the co-sputtering was performed with an Ar pressure of 20 standard cubic centimeters per minute (SCCM). The gas was introduced inside the chamber through a mass flow controller. The sputtering was performed at RF power of 30 W. The vacuum before the sputtering was 5×10^{-6} torr and during the sputtering was 3×10^{-3} torr. These as deposited films were subjected to microwave annealing at 800 and 900^0C.

The microwaves used in these experiments were produced using a 1.3 KW, 2.45 GHz single mode applicator. The samples were loaded in a chamber, thermally insulating package which is made of fiber-frax porous mullite fibers to prevent heat loss. Proper amount of silicon carbide was used as microwave susceptor around the sample within the insulating package to preheat the sample and compensate the heat loss from the sample. This configuration makes the microwave heating more uniform. The temperature of the sample was monitored by using IR pyrometer.

On the other hand, these as-deposited composite thin films of Ge and silica were irradiated with 150 MeV Ag^{+12} ions. The mean projected range of these ions is about 20 microns, which is much larger than the film thickness. The electronic energy loss and nuclear energy loss of 150 MeV Ag ions are 13 keV/nm and 0.048 keV/nm respectively. The films were also deposited on Carbon coated Nickel grids for TEM measurements and the same grids were subjected to swift heavy ion irradiation. The irradiation was performed at fixed fluence of $3x10^{13}$ ions/ cm^2 using the 15UD Pelletron accelerator at IUAC New Delhi. The ion beam current was maintained low (0.5–2 pnA) to avoid heating of the samples. The samples were kept at an angle of 5^0 with respect to the beam axis to avoid the channeling effect.

The composite films were analyzed by RBS measurements using the HV make 1.7 MV Tandetron accelerator. For RBS 2 MeV He^+ beam was used as a projectile and the scattered He^+ particles were detected by a surface barrier Si detector with scattering angle of 165° from the incident beam direction. Raman scattering spectra of the films were obtained before and after annealing in backscattering configuration with a Raman microscope using a 514.5 nm Ar+ laser excitation source. X-ray profiles were obtained with CuKα X-ray, λ=0.154nm in a glancing angle incidence geometry. The AFM measurements were carried out using SPA400, Seiko Instruments Inc. All the measurements were carried out at room temperature. Size of Ge nanocrystals embedded in Silica matrix has been obtained using transmission electron microscopy (TEM), namely, FEI TECNAI, G2 F-TWIN D2083 TEM, with electron-accelerating voltage of 200 kV.

4.3 Microwave annealing results:

4.3.1 Rutherford Backscattering spectrometry:

Thin films of Ge and SiO_2 nanocomposites with various Ge compositions of approximately 15%, 25%, and 35% have been deposited on Si substrate and named Set A, Set B and Set C respectively. The Ge fraction has been varied by changing the Ge area covered on SiO_2 target. Set B RBS spectrum of the Ge+SiO_2 composite film has been shown in Fig.4.1. The spectrum indicates the presence of Si, O and Ge in the sample. The estimated concentration of Ge from the RBS spectrum is around 22%. The thickness of the film is around 230 nm.

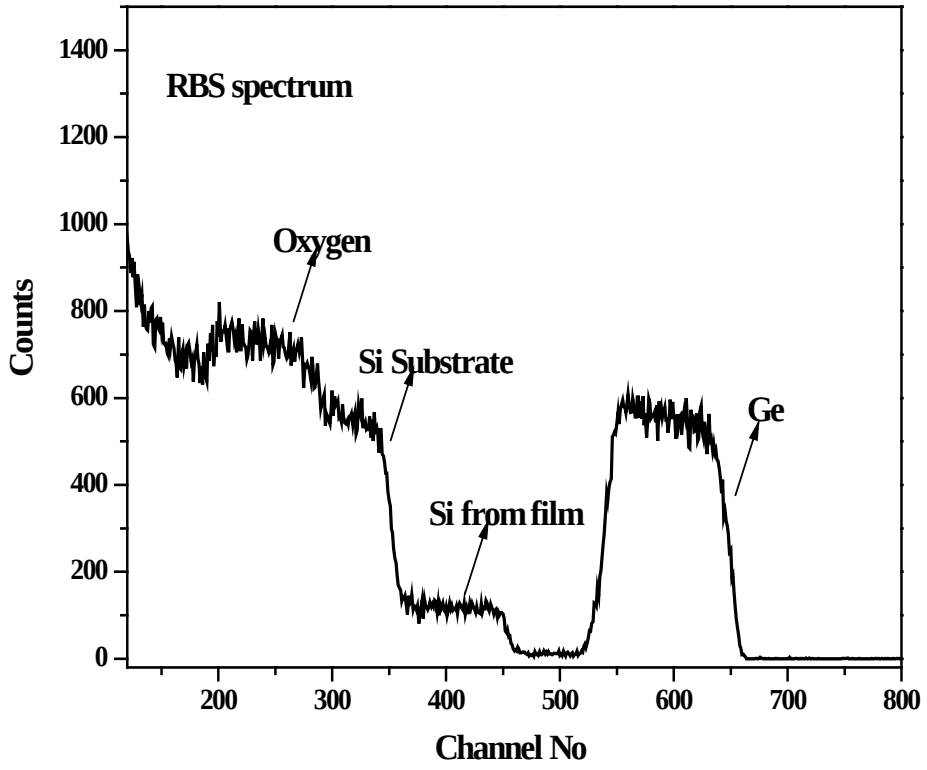

Fig. 4.1 RBS spectrum of as deposited sample B

4.3.2 Microwave temperature Profile:

Microwave annealing has been carried out systematically. Ramp up rates of about 30^0 C/min were applied to raise the temperature to the required annealing temperatures. Figure 4.2 shows the typical microwave annealing cycle with a controlled manner.

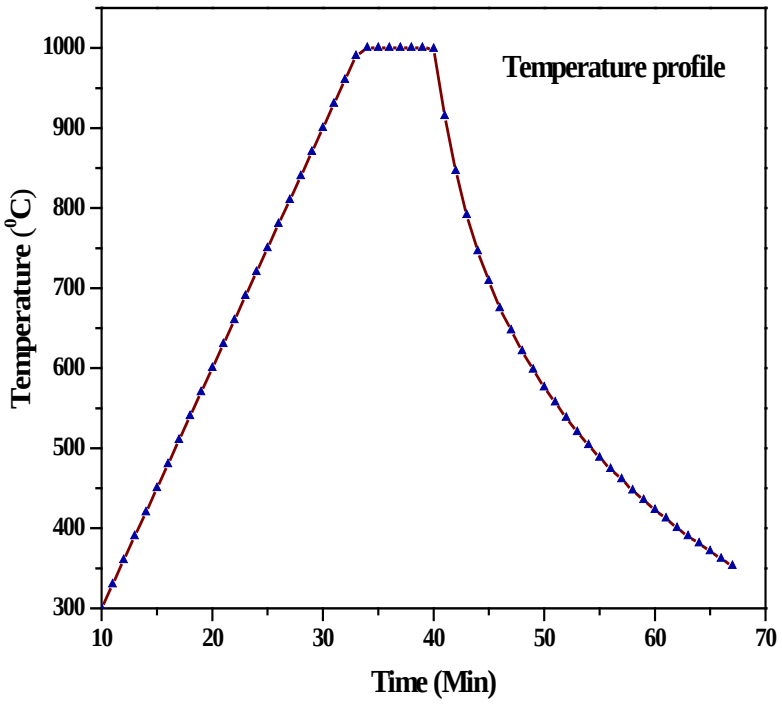

Fig. 4.2 The typical temperature profile of microwave annealing

4.3.3 X-ray diffraction:

The as-deposited films were annealed at 800 and 900^0C and characterized by using XRD. Fig. 4.3 shows the XRD spectra of set B as deposited and annealed films at 800 and 900^0C. As deposited film shows amorphous nature whereas annealed films show crystalline nature with three peaks of Ge (1 1 1), (2 2 0) and (3 1 1), which indicates the formation of nc-Ge. It is also observed that with the increase of annealing temperature, the XRD peaks become sharper and the full width at half-maximum (FWHM) of each peak decreases. This means that the average size of nc-Ge increases. Peak positions, d spacing, lattice parameter and crystallite size values have been compiled in table 1.

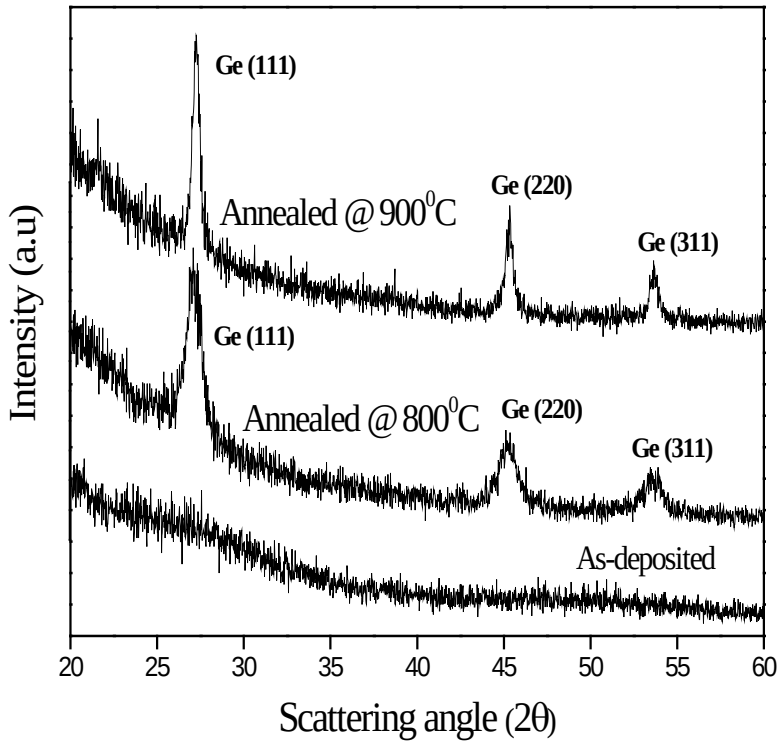

Fig.4.3: GIXRD spectra of Set B as deposited and annealed at 800 and 900^{0}C

Table 1: Peak positions, d spacing, lattice constant and nanocrystals size values of annealed samples at 800 & 900^0 C

Annealing Temp T (^{0}C)	Peak position	hkl	D spacing (nm)	Lattice parameter (nm)	Crystallite Size from Scherrer formula (nm)	Crystallite Size from WH plot (nm)
800	27.1	111	0.328	0.568	11	16
	45.2	220	0.200	0.565		
	53.6	311	0.170	0.565		
900	27.2	111	0.327	0.566	23	36
	45.3	220	0.199	0.565		
	53.6	311	0.170	0.565		

Fig.4.4 shows the XRD spectra of different Ge composition samples annealed at fixed temperature at 800^0C. The three main diffraction planes (111), (220) and (311) are present in the samples.

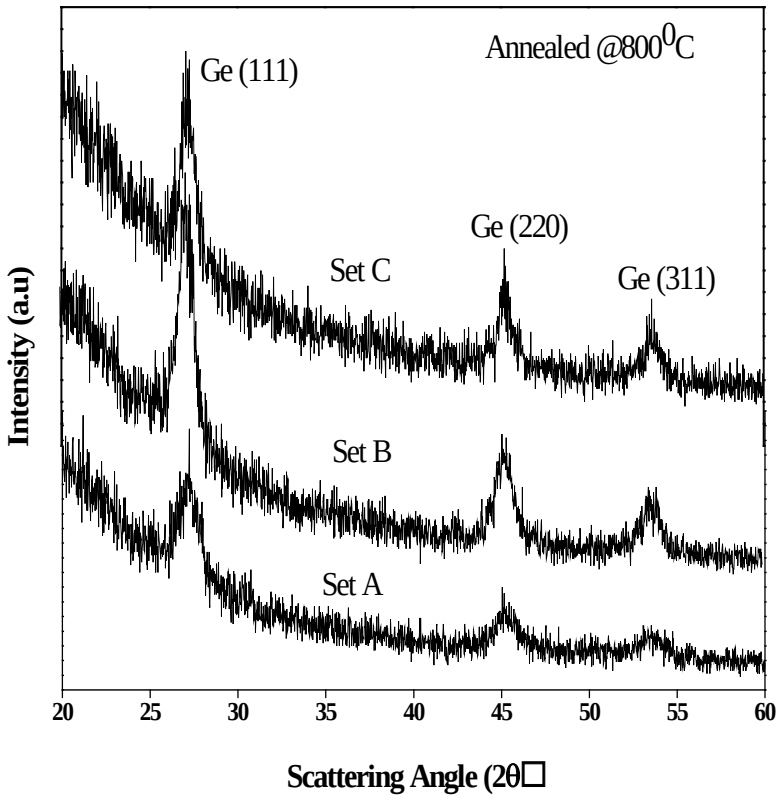

Fig.4.4: GIXRD spectra of Set A, Set B and Set C samples annealed at 800^0C

It is observed that the crystallite size increases with increase in Ge composition. Peak position and d spacing values are listed in table 2. For higher Ge composition more number of Ge atoms are available to nucleate and lead to bigger nanocrystals as compared to lower composition. This is evident from XRD spectrum. The amorphous Ge fraction becomes undetectable when the annealing temperature increases to 800^0C and we can obtain maximum crystallized nc-Ge embedded thin film samples. Therefore, to obtain better crystallization, we need to anneal the samples at higher temperature.

The crystallite size was calculated by using Scherrer formula as well as with Williamson-Hall (WH) method. In WH method [13, 28], it is assumed that the line broadening β_t of a Bragg reflection (h k l) originating from the small crystallite size follows Scherrer equation $\beta_t = K\lambda / D \cos\theta_{hkl}$. Here K is the shape factor, λ is the wavelength of X-rays, θ_{hkl} is the Brag angle and D is the effective crystallite size. Similarly, according to Wilson [29], the broadening due to lattice strain can be expressed by the relation, $\beta_\varepsilon = 4\varepsilon \tan\theta_{hkl}$. Thus, the observed peak broadening (β_{hkl}) may be represented as sum of broadening due to crystallite size and lattice strain, in addition to broadening due to instrumental factors.

i.e. $\beta_{hkl} = \beta_t + \beta_\varepsilon = [K\lambda/D \cos\theta_{hkl}] + [4\varepsilon \tan\theta_{hkl}]$

$$\beta_{hkl} \cos\theta_{hkl} = [K\lambda/D] + [4\varepsilon \sin\theta_{hkl}] \quad \text{…….(1)}$$

The micro-strain ε may be estimated from the slope of the line by plotting the value of $\beta_{hkl} \cos\theta_{hkl}$ as a function of $4 \sin\theta_{hkl}$ and crystallite size from the intersection with the vertical axis. The size of the nanocrystals calculated using Scherrer formula varies from 11 nm to 23nm when the annealing temperature increases from 800 to 900^0C. The effective crystallite size was also estimated by using WH method and plotting $\beta\cos\theta_{hkl}$ versus $4\sin\theta_{hkl}$ as shown in figure 4.5 for set B samples annealed at various temperatures. Here the crystallite size varies from 16 nm to 36nm when the annealing temperature increases from 800 to 900^0C. The difference in the crystallite size obtained by the two methods is due the fact that the Scherrer equation does not take into account the effect of lattice strain and instrumental peak broadening. These parameters do affect the overall broadening of XRD peaks. Hence, the crystallite size obtained using Scherrer equation is smaller than that estimated by Williamson-Hall method.

Similarly, the effective crystallite size was also estimated by using WH method for set A, set B and set C samples annealed at fixed temperature. The variation of crystallite size with annealing temperature and with Ge composition is shown in Fig 4.6.

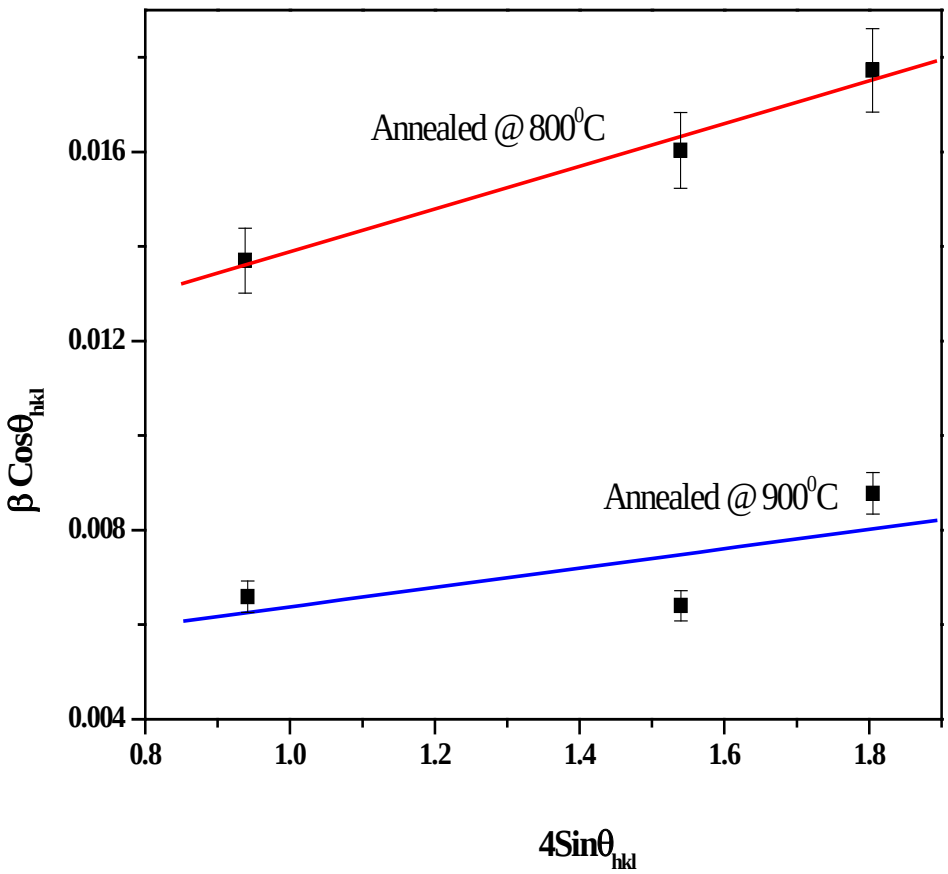

Fig.4.5: Plot of $\beta Cos\theta_{hkl}$ versus $4Sin\theta_{hkl}$ for as deposited and annealed samples

Table 2: Peak positions and d spacing of Set A, Set B and Set C samples annealed at 800^{0}C

Annealing @ 800^{0}C	Peak position	hkl	D spacing	Crystallite Size (nm)	Size from W-H plot
SET A	27.1	111	0.328	9	11
	45.2	220	0.200		
SET B	27.1	111	0.328	11	16
	45.2	220	0.200		
	53.6	311	0.170		
SET C	27.1	111	0.328	13	22
	45.2	220	0.200		
	53.6	311	0.170		

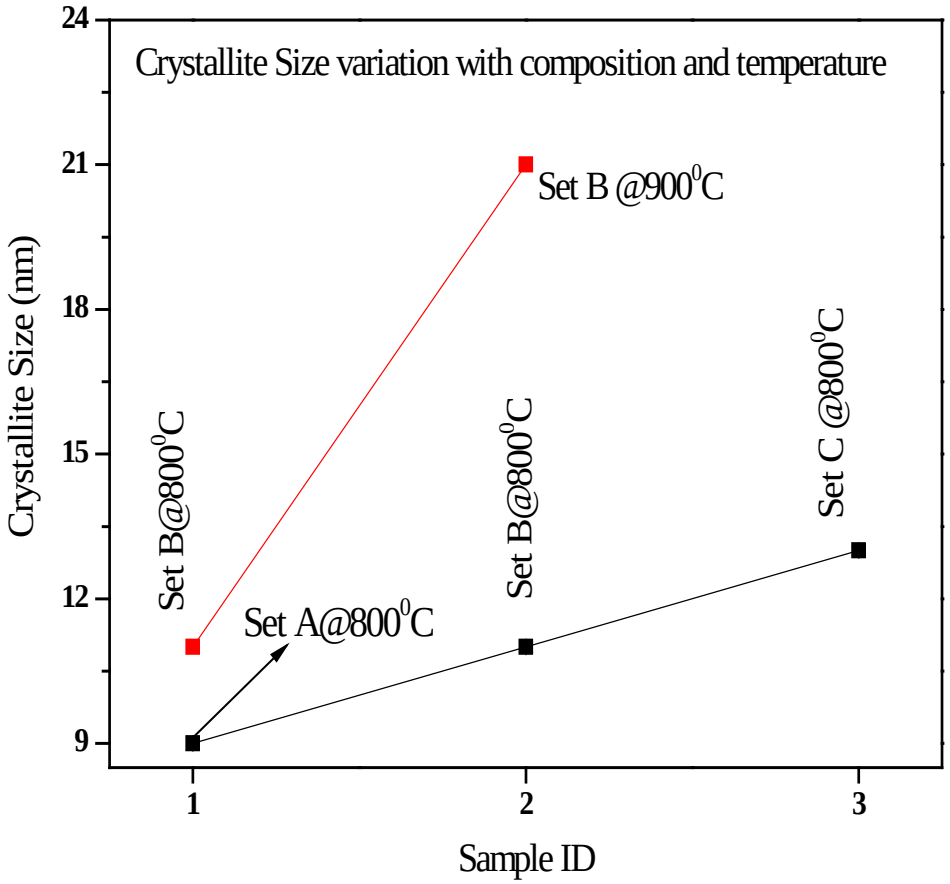

Fig.4.6: Plot of Crystallite size as a function of annealing temperature and Ge composition.

4.3.4 Raman spectroscopy:

Raman scattering is expected to be sensitive not only to quantum confinement, but also to disorder, strain and structural characteristics of the system. Figure 4.7 shows Raman spectra of the set B as-deposited and the annealed samples. Figure 4.8 shows the Raman spectra of annealed samples at 800^{0}C with different Ge composition. It can be seen that the as-deposited sample exhibits a broad band which is the characteristic feature of amorphous Ge [30]. However, for the annealed sample, a sharp Raman peak was observed at around 299 cm^{-1}, which is different in comparison with that of the bulk Ge, indicating Ge crystallization [31]. For bulk crystalline Ge, the Raman spectrum exhibits a Lorentzian line at 300 cm^{-1} with an intrinsic width of around 3 cm^{-1}. The origin of the shift and asymmetrical broadening of the Raman spectra is due to the confinement of phonons and is also characteristic of nanocrystals [32-33].

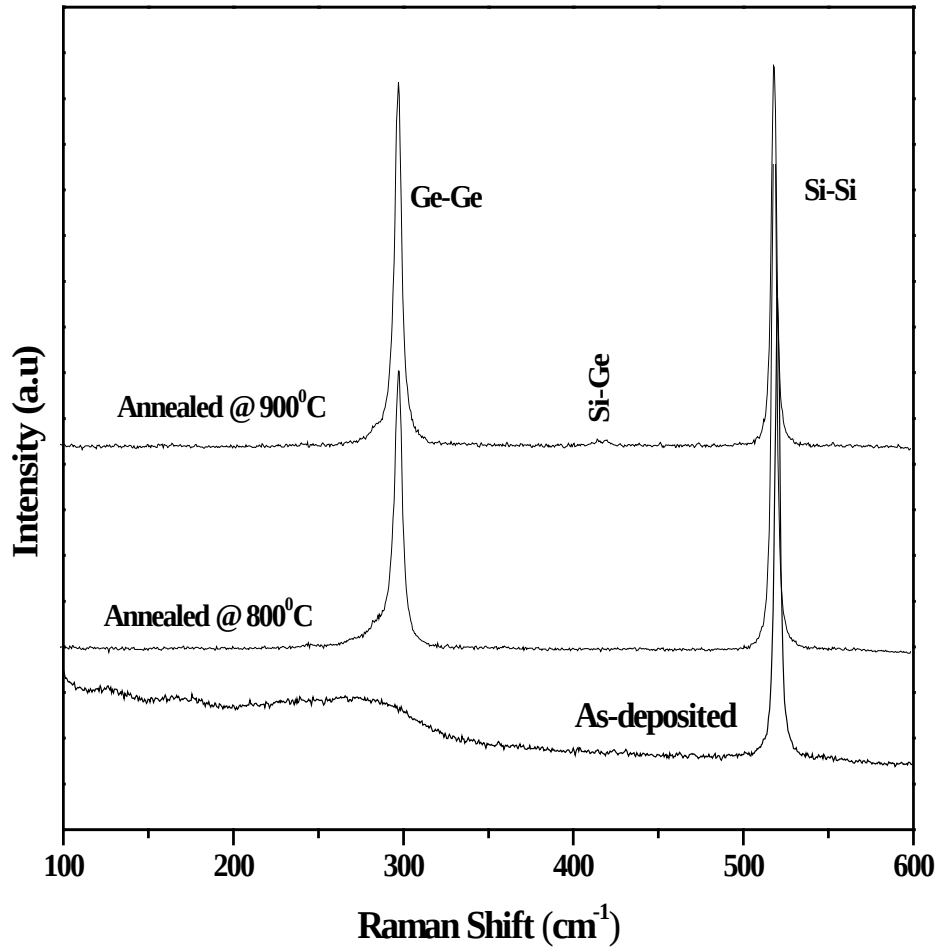

Fig.4.7: Raman spectra of Set B as deposited and annealed at 800 and 900^{0}C

One can calculate the size of the nanocrystal by using the detailed formula for first order Raman spectrum,

$$I(\omega) \cong \int \frac{|C(0,\vec{q})|^2}{[\omega - \omega(\vec{q})]^2 + \left(\frac{\Gamma_0}{2}\right)^2} d^3\vec{q}$$

where ω (q) is the phonon dispersion relation and Γ_0 is the natural line width (FWHM) of the scattered signal, and C (0, $\vec{q}$) is the Fourier transform of the phonon confinement. However, a simpler formula has been used in our case to calculate nanocrystal size. The mean grain size of Ge can be roughly estimated using the following equation,

$$D = 2\pi \sqrt{B/\Delta\omega}$$

where $\Delta\omega$ is the shift of the Raman peak for crystals compared to that of the bulk Ge value (300.5 cm^{-1}) and B is a constant (2.0 nm^2 cm^{-1}) [34-36]. The FWHM values of the peaks around 299 cm^{-1} of samples annealed at 800 and 900^0C are 5.2 and 4.8 cm^{-1} respectively. The calculated crystallite size for the sample annealed at 800^0C is about 8 nm. We did not observe much variation in crystallite size from the Raman spectra with annealing temperature. The feature located around 420 cm^{-1} in annealed sample at 900^0C is due to Ge-Si vibrations. This Ge-Si signal is due to alloying of Ge with Si at the surface as a result of annealing. Generally, when the annealing temperature increases and reaches a threshold level then the partial structure of the as deposited film transforms from amorphous to crystalline. In other words, the amorphous and crystalline phases coexist. But, when the annealing temperature increases further, then more of the amorphous structure in the as-deposited film will be transformed into crystalline structure which is reflected in the intensity of the Raman peak.

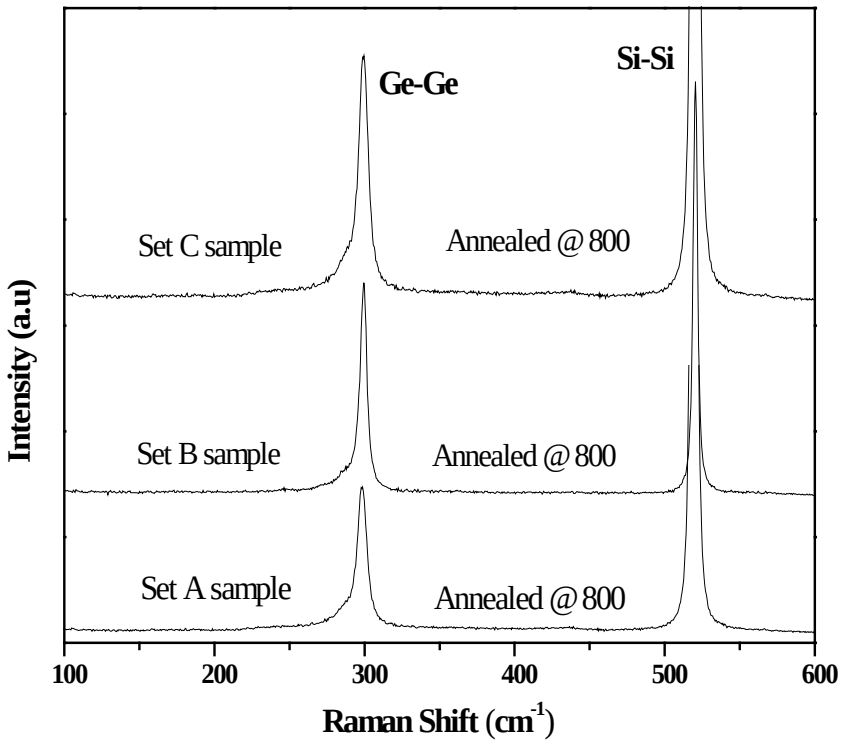

Fig.4.8: Raman spectra of Set A, B and C samples annealed at 800^0C

4.3.5 Atomic force microscopy:

Surface morphology of the as-deposited and annealed samples has been studied using AFM. Topography of composite films covering an area of 1µm x 1 µm of as deposited samples have been shown in Figs. 4.9 and 4.10 and 4.11 for Set A, Set B, and Set C samples respectively. The dark pixel in image reveals the valley and we observed smooth surface in these samples. Surface morphology of the pristine samples has been studied using AFM. The surface roughness increases with increase in Ge composition. Nonetheless films have smooth surface.

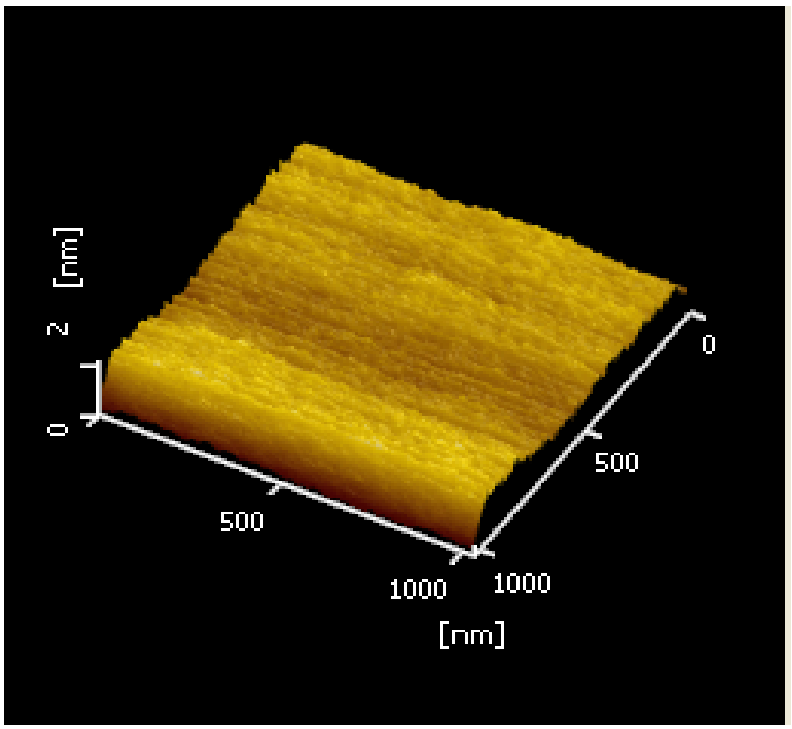

Fig 4.9 AFM image of Set A sample as deposited

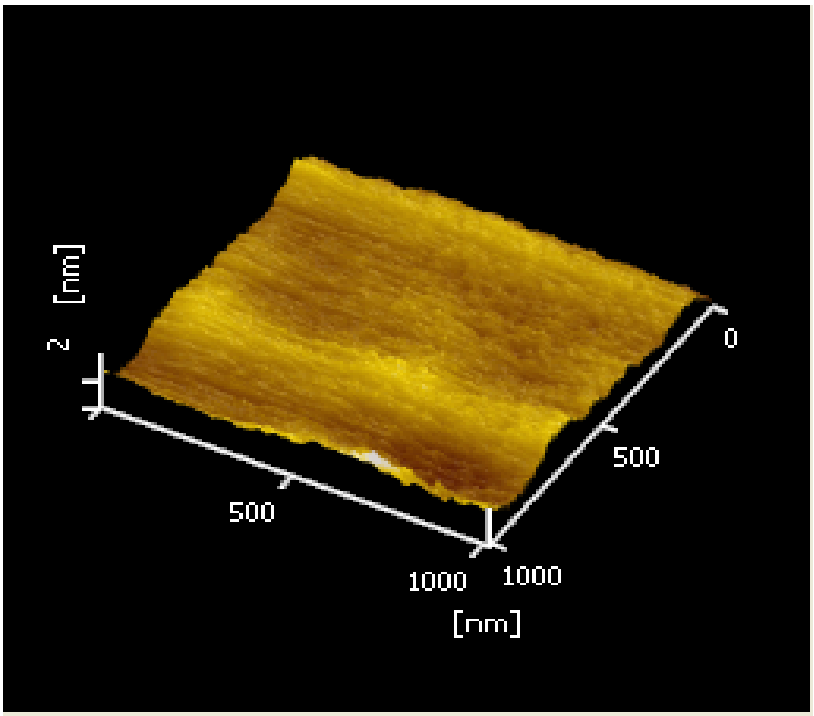

Fig 4.10 AFM image of Set B sample as deposited

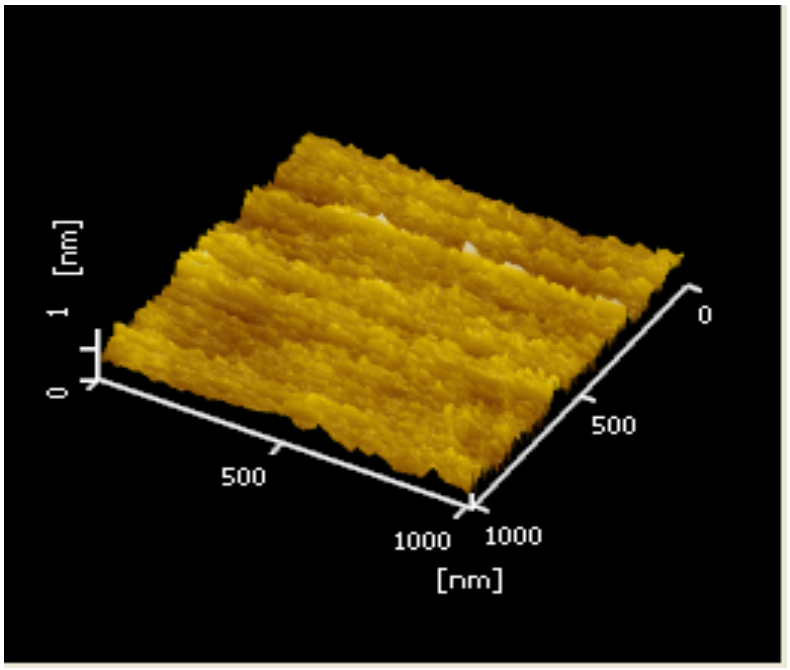

Fig 4.11 AFM image of Set C sample as deposited

Growth of the nanocrystals can be explained in different ways like nucleation and growth, Ostwald ripening and agglomeration etc. Ostwald ripening is the processes where small crystals form in a system initially but slowly disappear except for a few that grow larger, at the expense of other smaller crystals. In as-deposited sample, there is no signature of nanoparticles but annealing results in formation and growth of nanoparticles. Due to high temperature annealing the diffusivity of Ge atoms and small nanocrystals increases such that the nucleation rate is enhanced leading to a higher density of nanocrystals. When the composition of atoms or ions in a particular spatial region of a solid becomes sufficiently high, they aggregate into small nanocrystals or clusters through homogeneous nucleation. These clusters tend to coalesce and grow to form larger nanocrystals. These nanoparticles exhibit a high reactivity and strong tendency towards agglomeration due to their large surface area. Moreover, rapid grain growth is likely to occur during processing at high temperatures. Since nc-Ge crystallization temperature is lower than Ge melting point temperature, Ge clusters and nanocrystals were formed by diffusion of Ge atoms or clusters inside silicon oxide matrix.

Various annealing methods have been used to prepare nanocrystals such as furnace annealing, RTA, and Laser Annealing. But, each of these methods has their own limitations. It is well known that furnace annealing takes few hours to complete the material processing. To avoid surface deterioration caused by slow heating and cooling rates of conventional resistive heating furnaces, new ultrafast annealing techniques need to be explored. Similarly, in Laser Annealing method, the spot size is very small. Hence, it requires lot of time to cover entire surface area of wafer. In this process there is high probability for overlapping or missing some part of the wafer. Halogen lamp and laser-based rapid thermal processing techniques suffer from problems such as a possible limitation on the maximum achievable annealing temperature, surface melting, a large residual defect density, and redistribution of the implants [37-38]. But microwave heating may solve many of these problems. One can tune the structural, optical and electrical properties of nanocrstals by varying the microwave annealing parameters like annealing time, temperature, and RF deposition parameters for various applications.

4.4 Irradiation Results:

4.4.1 X-ray diffraction:

XRD spectra of as-deposited and irradiated samples have been shown in Fig.4.12. It is clear from the spectra that the pristine sample shows amorphous nature where as irradiation leads to crystallization of these films. The average size of the nanoparticles is calculated using Scherrer's formula given by

$$D = \frac{0.9\,\lambda}{\beta\, Cos\theta_B}$$

where λ is the wavelength of the X-ray source (*i.e*, 1.5406A^0 for CuKα), β = FWHM (in radians) and θ_B is Bragg angle and D is the diameter of the nanocrystal. The size of the nanocrystal was estimated to be around 31 nm.

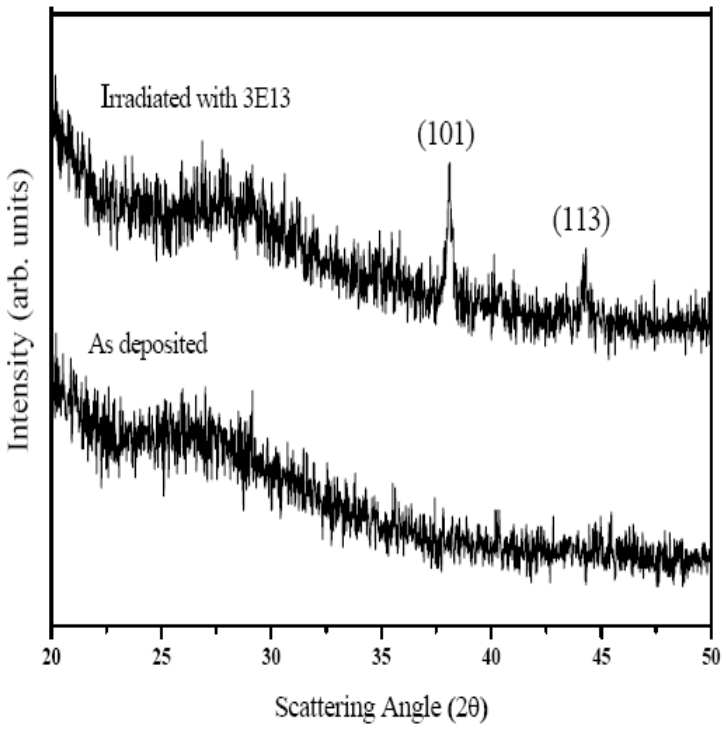

Fig.4.12: GIXRD spectra of as deposited and irradiated samples

4.4.2 Raman spectroscopy:

The Raman spectra of as-deposited and irradiated sample have been shown in Fig.4.13. The as-deposited sample shows a broad Raman peak centered at 270cm^{-1} which corresponds to amorphous Ge [39]. The appearance of peak around 290 cm^{-1} for the irradiated sample indicates the crystallization of the film. The broad feature in the irradiated Raman spectrum along with the peak at ~290 cm^{-1} indicates partial amorphous nature of the film.

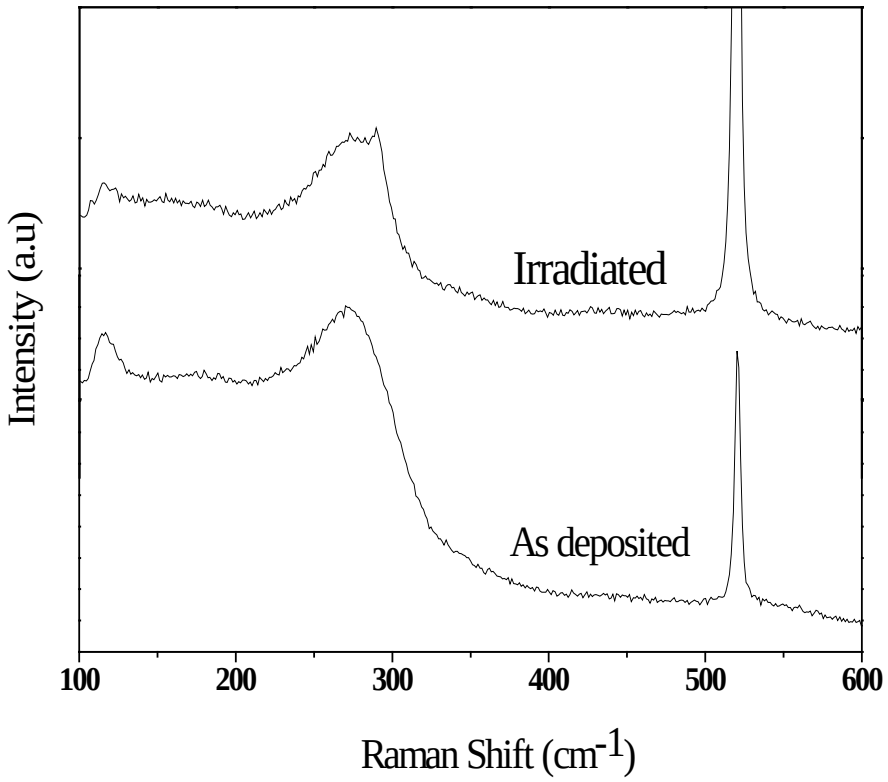

Fig.4.13: Raman spectra of as deposited and irradiated samples

It is known that mechanical compressions can lead to an increase in the frequency of Ge–Ge bond vibrations. Due to the 4% mismatch in the lattice constants, the shift for transverse optical modes can reach 10cm^{-1} [40]. The effect of mechanical stresses would lead to a shift of peaks toward the high-frequency region. It is also possible that the structural change of the Ge nanocrystals or stress in the high Ge concentration films will also result the peak position to be lower than the bulk Ge value. Raman spectra of the samples show a shift in the peak position and an asymmetrical broadening indicates the existence of crystalline Ge.

4.4.3 Transmission Electron spectroscopy:

Figure 4.14a shows TEM image of typical Ge nanocrystals obtained from the irradiated sample. Here the formation of nanocrystallites is clearly seen in the TEM micrographs of the Ag ion irradiated sample. The average size of the nanocrystal is found to be around 20 nm. The size distribution of Ge nanocrystals has been shown in Fig 4.14b.

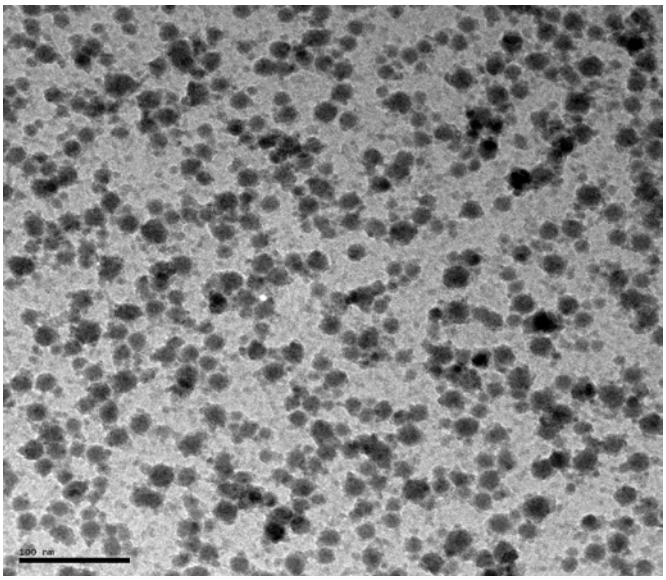

Fig.4.14a: TEM image of 150 MeV Ag irradiated sample at a fluence of 3 x 10^{13} ions/cm^2

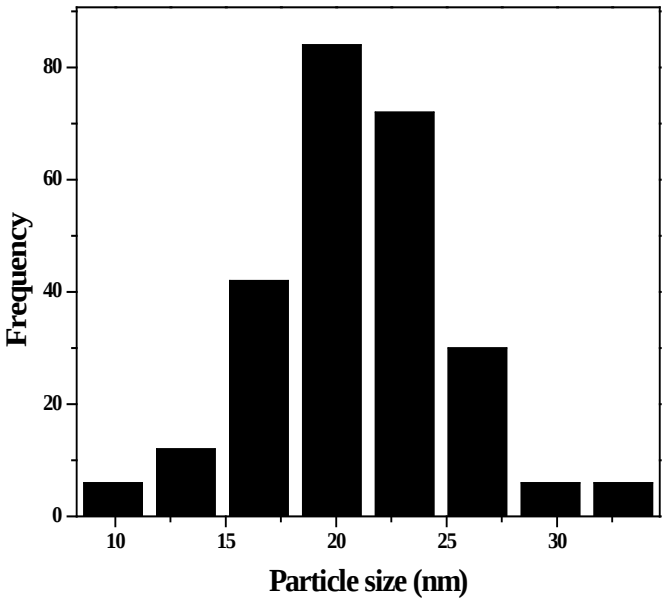

Fig.4.14b: The size distribution of Ge nanocrystals

It is possible that Ge nanocrystals with different average nanocrystal sizes and size distributions can be synthesized by varying ion fluence and energy.

4.4.4 Atomic force microscopy:

The surface topography of Ge+SiO_2 films was investigated with AFM. It shows that the as-deposited films have less surface roughness than the irradiated ones, the roughness of films increased and a grain-like morphology was exhibited. The 3D AFM images of the as-deposited and irradiated samples are shown in Fig. 4.15a and 4.15b respectively. The rms roughness values of as-deposited and annealed films are 0.1 to 2.2 nm. Surface Morphological changes in the irradiated films can be observed clearly from the figures. While the as deposited film is more or less flat and featureless, the irradiated film shows an evolution of nano-sized grains.

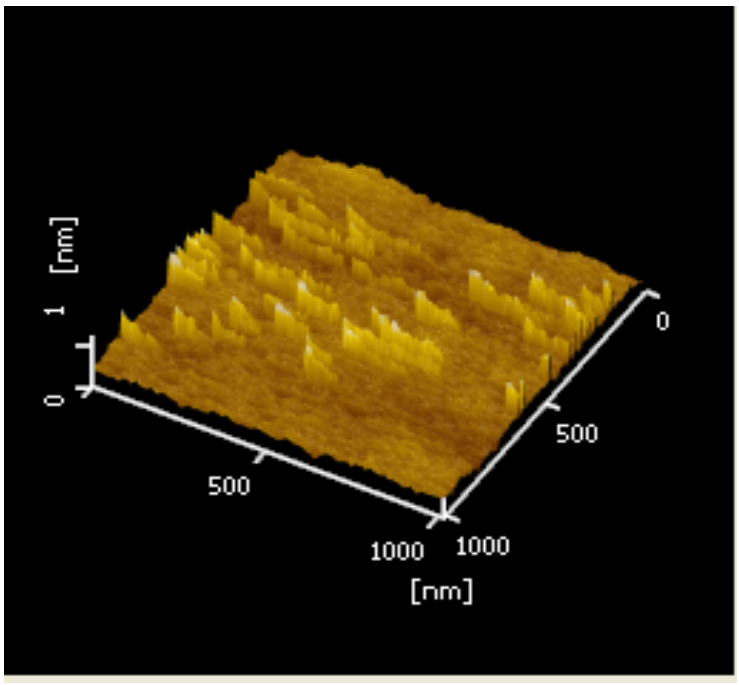

Fig. 4.15a: Atomic force microscope image of as-deposited sample

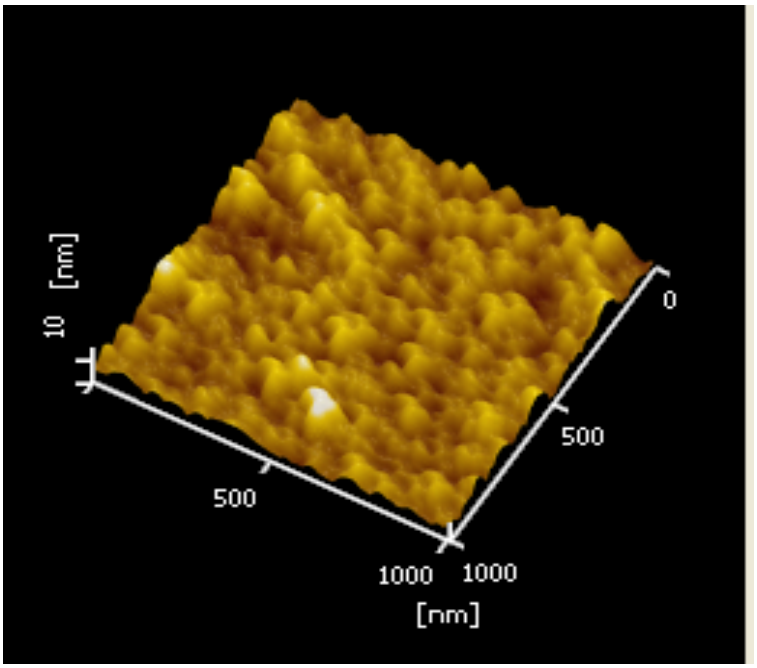

Fig. 4.15b: Atomic force microscope images of irradiated sample

When an energetic ion interacts with a solid, it undergoes a series of collisions with the atoms and electrons in the target. In these collision processes incident ion loses energy ranging from few to 100 keV/ nm depending upon the energy, mass, and density of the target. The energy loss rate dE/dx of an energetic ion moving through a solid is determined by screened Coulomb interactions with the substrate atoms and electrons. Ion loses its energy through two major processes i.e. nuclear or elastic collisions, in which energy is transferred to a target atom as whole and electronic collisions, in which the moving particle energy is used in exciting or ejecting the atomic electrons of the target. Electronic collisions involve negligible deflection of the ion trajectory, and lattice disorder. When the projectile velocity v is much greater than that of an orbital electron, the influence of the incident particle on an atom (as a whole) may be considered as a sudden, small external perturbation. But the collision produces a sudden transfer of energy from the projectile to the target electrons. The stopping cross section increases with decreasing velocity because the particle spends more time in the vicinity of the atom, with slowing down. The deposition of energy into the film is predominantly through electronic energy loss. This energy deposition leads to crystallization similar to that of thermal crystallization and can be considered as

the crystallization induced by thermal spikes. One can explain the basic mechanism of recrystallization and formation of nanocrystals in these samples, under ion-irradiation with the help of thermal spike theory [41]. When the swift heavy ion passes through the material the energy is transferred to the target lattice via electron–phonon coupling. It is known from the work of Meftah *et al.* [42] and Toulemonde *et al.* [43] that a track diameter of about 10 nm is created for a *Se* value of ~11 keV/nm in silica. This large amount of energy is transferred to the target electrons in very short time, of the order of $\sim 10^{-12}$ seconds which leads to an increase of the lattice temperature above its melting point along the ion track. The temperature along the ion path goes to very high value which is sufficient to crystallize the Ge, which is embedded in Silica. This results in a modification of structure of films around the cylindrical zone and crystallization of the films.

4.5 Conclusions:

In conclusion, we have synthesized Ge nanocrystals embedded in SiO_2 matrix films by using microwave annealing process. The films were first deposited by RF magnetron sputtering and subjected to microwave annealing at 800 and 900^0C. The structural properties of the nanocrystals were characterized by XRD and Raman spectroscopy. XRD spectra reveal that as-deposited film shows amorphous nature and annealing results in crystallization. The Ge modes in the Raman spectra of annealed samples indicate the existence of crystalline Ge. The estimated nanocrystal size is found to vary with annealing temperature and Ge composition. The variation of crystallite size as a function of annealing temperature and advantages of microwave annealing have been discussed. Synthesis of Ge nanocrystals by using RF sputtering followed by ion irradiation has been investigated. The composite films were irradiated with 150 MeV Ag ions at a fixed fluence of $3x10^{13}$ ions/cm^2. As deposited films show amorphous nature but irradiation leads to formation of nanocrystals, which is clear from XRD and Raman spectroscopy. Surface morphology of the samples is studied by AFM. TEM image shows clearly the formation of nanocrystals and the average crystallite size of these Ge nanocrystals is found to be around 20 nm. The mechanism of ion beam induced Ge recrystallization has been discussed.

4.6 References

1. S. Takeoka, Phys. Rev. B 58 (1998) 12
2. L. Brus, Appl. Phys. A 53 (1991) 465
3. Y.X. Jie, Y.N. Xiong, A.T.S. Wee, C.H.A. Huan, W. Ji, Appl. Phys. Lett. 77 (2000) 3926
4. R J Walters, G I Bourianoff and H A Atwater, Nat. Mater. 4 (2005)143
5. G Conibeer G et al Thin Solid Films 511/512 (2006) 654
6. W K Choi, W K Chim , C L Heng, L W Teo, V Ho, V Ng, D A Antoniadis and E A Fitzgerald , Appl. Phys. Lett. 80 (2002) 2014
7. Y Maeda, N Tsukamoto, Y Yazawa, Y Kanemitsu and Y Masumoto , Appl. Phys. Lett. 59 (1991) 3168
8. A G Cullis, L T Canham and P D J Calcott, J. Appl. Phys. 82 (1997) 909
9. Y. Kanemitsu, K. Masuda, M. Yamamoto, K. Kajiyama, T. Kushida, Journal of Luminescence 87-89 (2000) 457
10. X.M. Wu, M.J. Lu, W.G. Yao, Surface and Coatings Technology 161 (2002) 92
11. W.K. Choi , S. Kanakaraju , Z.X. Shen, W.S. Li , Applied Surface Science 144–145 (1999) 697
12. O. Adeoya, M. Hage Ali, J.C. Muller, P. Siffert, Appl. Phys. Lett. 50 (1987) 1736
13. J. Nakata, Phys. Rev. B 43 (1991) 14643.
14. J. Nakata, J. Appl. Phys. 79 (1996) 682.
15. T.Som, B. Satpati, O. P. Sinha, and D. Kanjilal, J. Appl. Phys. 98 (2005) 13532.
16. J. Linnros, G. Holmen and B. Sevensson, Phys. Rev. B 32 (1985) 2770.
17. P. Songsiriritthigul and G. Holmén, Nucl. Instr. and Meth. B 120 (1996) 207.
18. T. Mohanty, Mishra N C, Pradhan Asima and Kanjilal D, Surf. Coat. Technol. 196 (2005) 34
19. Prajakta S. Chaudhari, Tejashree M. Bhave, D. Kanjilal and S.V. Bhoraskar, J. Appl. Phys. 93 (2003) 3486.
20. G.A. Kachurin, S.G. Cherkova, D.V. Marin, A.G. Cherkov, V.A. Skuratov, Appl Phys A 98 (2010) 873

21. Shyama Rath, D. Kabiraj, D.K. Avasthi, A. Tripathi, K.P. Jain, Manoj Kumar, H.S. Mavi, A.K. Shukla, Nuclear Instruments and Methods in Physics Research B 263 (2007) 419
22. N. Srinivasa Rao, S. Dhamodaran, A.P. Pathak, P.K. Kulriya, Y.K.Mishra, F. Singh, D. Kabiraj, J.C. Pivin, D.K. Avasthi. Nucl. Inst. Meth B 264 (2007) 249.
23. N Srinivasa Rao, S Dhamodaran, A P Pathak, D Kabiraj, S A Khan, B K Panigrahi, K G M Nair, B Sundaravel, J C Pivin and D K Avasthi, Radiation Effects and Defects in Solids, 164 (2009) 452.
24. D. K. Avasthi, Y. K. Mishra, D. Kabiraj, N. P. Lalla and J. C. Pivin, Nanotechnology 18 (2007) 125604.
25. Y. K. Mishra, S. Mohapatra, Rahul Singhal, D. K. Avasthi, D. C. Agarwal, S. B. Ogale, Appl. Phys. Lett. 92 (2008) 043107
26. N. Srinivasa Rao, A.P. Pathak, N. Sathish, G. Devaraju, S.A. Khan, K. Saravanan, B.K. Panigrahi, K.G.M. Nair, D.K. Avasthi, Nuclear Instru. and Methods in Physics Research B 268 (2010) 1741.
27. M. C. Ridgway, G. de M. Azevedo, R. G. Elliman, C. J. Glover, D. J. Llewellyn, R. Miller, and W. Wesch, G. J. Foran, J. Hansen and A. Nylandsted-Larsen, Phys. Rev. B 71 (2005) 094107
28. G K Williamson and W H Hall Acta Metall. 1 (1953) 22
29. A.J.C. Wilson, X-ray Optics (Methuen, London) 1949.
& A.R. Stokes and A.J.C. Wilson. Proc. Phys. Soc. London 56 (1944) 174
30. Y Sasaki and C Horie , Phys. Rev. B 47 (1993) 3811
31. W.K. Choi, Y.W. Ho, S. P. Ng, and V. Ng, J. Appl. Phys. 89 (2001) 2168.
32. P. Tognini, L.C. Andreani, M. Geddo, A. Stella, P. Cheyssac, R. Kofman, A. Migliori, Phys. Rev. B 53 (11) (1996) 6992.
33. M.I. Vasilevskiy, A.G. Rolo, M.J.M. Gomes, Solid State Commun., 104 (1997) 381.
34. M. Cardona, G. Güntherodt, Light Scattering in Solids (Springer, Berlin, 1982)
35. L.P. Yue, Y.Z. He, Acta Phys. Sin. 45 (1996) 1756
36. X.L.Wu, S.J. Xiong, G.G. Siu, G.S. Huang, Y.F. Mei, Z.Y. Zhang, S.S. Deng, C. Tan, Phys. Rev. Lett. 91 (2003) 157402
37. Y. Tanaka, H. Tanoue, and K. Arai, J. Appl. Phys. 93 (2003) 5934.

38. S.D. Ruksell and A.D. Ramirez, Appl. Phys. Lett. 74 (2002) 3368.
39. Y. Sasaki and C. Horie, Phys. Rev. B 47 (1993) 3811
40. D. A. Orekhov, V. A. Volodin, M. D. Efremov, A. I. Nikiforov, V. V. Ul'yanov, and O. P. Pchelyakov, Journal of Experimental and Theoretical Physics Letters, 81 (2005) 331
41. M. Toulemonde, C. Dufour, E. Paumier, Phys. Rev. B 46 (1992) 14362
42. A. Meftah, F. Brisard, M. Costantini et al., Phys. Rev. B 49 (1994) 12457
43. M. Toulemonde, J.M. Costantini, Ch. Dufour et al., Nucl. Instrum. Methods B (1996) 11637.

Chapter – V

SHI induced effects on Ge implanted SiO_2/ Si films

5.1 Introduction

Synthesis, characterization and processing of nanostructured materials are part of an emerging and rapidly growing field. Research and development in this field emphasizes scientific discoveries in the generation of materials with controlled microstructural characteristics. Particularly, semiconductor nanocrystals exhibit significant size dependant electronic properties generally ascribed due to quantum confinement effects. The properties of a material containing semiconductor nanocrystals strongly depend on the size and spatial distributions of the nanocrystals within the material.

In recent years, nanocrystalline silicon (Si) and germanium (Ge) have attracted much interest because of their visible photoluminescence at room temperature [1–4], and possible applications in devices such as electronics and optoelectronics [5, 6]. Various methods have been reported on the preparation of Ge nanoparticles, including gas evaporation [7], gas condensation [8], RF sputtering [9, 10], thermal evaporation [11], molecular beam expitaxy [12], pulsed laser ablation [13–14] and sol–gel [15].

Ion beam synthesis of semiconductor nanoparticles in thermally grown SiO_2 films has recently drawn considerable interest because of its ease and simplicity in growing particles of varying size. Both Si [l6] and Ge [17] nanoparticles have been grown by ion-implanting either Si^+ or Ge^+ ions into thermally grown SiO_2, films and subsequent annealing at temperatures 800^0 C or higher in a nitrogen environment.

However, the growth of these nanoparticles with a uniform size distribution is a challenge to the material scientists. A narrow uniform size distribution of these nanoparticles would enhance the physical properties of these materials which would eventually lead to their successful applications to optoelectronic devices. On the other

hand, the ion implantation is considered as one of the promising formation methods of the nanocrystals since the ion implantation can precisely control the projectile depth profile. One of the most versatile techniques for nanocrystal fabrication involves high-dose ion implantation followed by thermal annealing, because the size and structure of nanocrystal can be controlled by changing the ion dose, the kinetic energy of ions, and the annealing temperature [18-22]. Ion implantation and thermal annealing have been used to create element [19, 20] and compound semiconductor nanocrystals [20-22] in amorphous matrices such as SiO_2 films. SHI irradiation is a well established tool for modification of the properties of nanomaterials [23]. The properties and modification of target material depend upon the energy and fluence of the incident ions. In the present work, we report the synthesis of Ge nanoparticles in silica and silicon matrices using the ion implantation technique followed by subsequent swift heavy ion (SHI) irradiation.

5.2. Experimental Details

We have grown 1µm thick SiO_2 films on the Si wafers by thermal oxidation. 400 keV Ge^+ ions were implanted into the thermal SiO_2 films with a dose of 3×10^{16} ions/cm^2 at room temperature. The chamber vacuum during ion implantation was better than $6x10^{-7}$ mbar. The range of penetration of 400 keV Ge^+ ions in SiO_2 is found to be 271 nm with a straggling of 58 nm using Monte-Carlo simulation code SRIM-2008. The Ge implanted SiO_2/Si sample was analyzed by RBS measurement. For RBS, 2 MeV He^+ beam was used as a projectile and the scattered He^+ particles were detected by a surface barrier Si detector with scattering angle of 165° from the incident beam direction. The HV make 1.7 MV Tandetron accelerators present at IGCAR, Kalpakkam was used for Ge implantation and RBS analysis. Subsequently, the as-implanted samples were irradiated using the 15UD Pelletron accelerator at the Inter University Accelerator Centre (IUAC), New Delhi at room temperature by 150 MeV Ag^{12+} ions with the ion fluence of 5×10^{12} and 2×10^{13} ions/cm^2. The ion beam current was maintained low as 0.5 pnA to avoid heating of the samples. The samples were kept at an angle of 5^0 with respect to the beam axis to avoid the channeling effect. On the other hand 400keV Ge^+ ions were implanted with a fluence of 5×10^{16} ions/cm^2 into an ultrasonically cleaned p-type Si (001) substrate. During implantation the substrate temperature was maintained at 573 K to reduce the amorphization of

surface Si layer. The as-implanted sample of Si was irradiated at room temperature with 100 MeV Au^{8+} ions at IUAC, New Delhi with a fluence of 1×10^{13} ions/cm^2 to investigate the behavior of high fluence Ge implanted Si. The Raman measurements were carried out on these samples at room temperature using the 514.5 nm line of an Ar ion laser as an excitation source in backscattering configuration. X-ray diffraction spectra were recorded by Bruker D8 Advance diffractometer, using a CuKα x-ray (wavelength is 1.5406 Å) at IUAC, New Delhi. All the measurements were carried out at room temperature.

5.3 Results and Discussion

RBS spectrum of the Ge implanted SiO_2 pristine sample has been shown in Fig.5.1. The spectrum indicates the presence of Si, O and Ge in the sample. The estimated concentration of Ge from the RBS spectrum is around 2.3%.

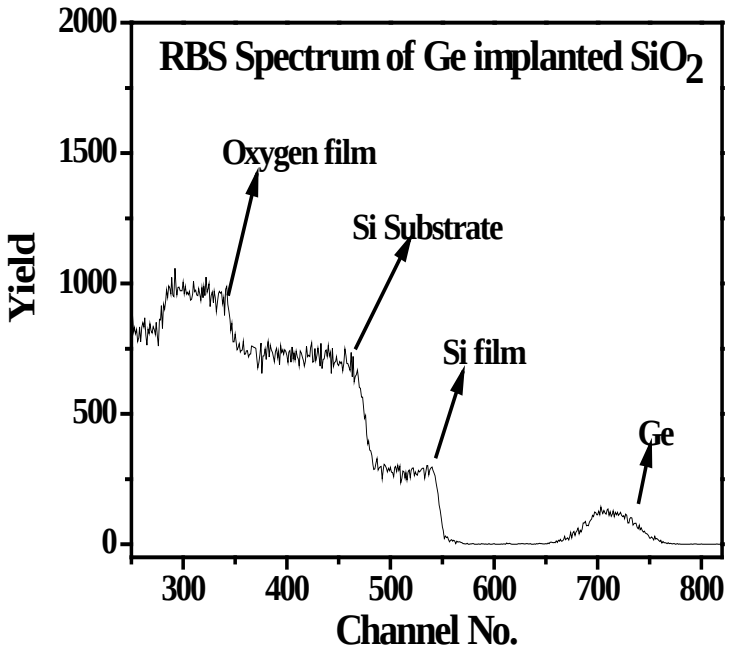

Fig.5.1: RBS spectrum of Ge implanted SiO_2 film

Fig.5.2 shows the GIXRD spectra of 150 MeV Ag^{+12} ion irradiated Ge implanted SiO_2 samples. The full width at half maximum is reduced when the films are irradiated with higher fluence. This increase in particle size happens due to higher diffusivity of Ge atoms and small nanocrystals with increase of irradiation ion fluence. This mechanism of higher diffusivity results in nucleation of smaller nanocrystals to form bigger NC's.

.

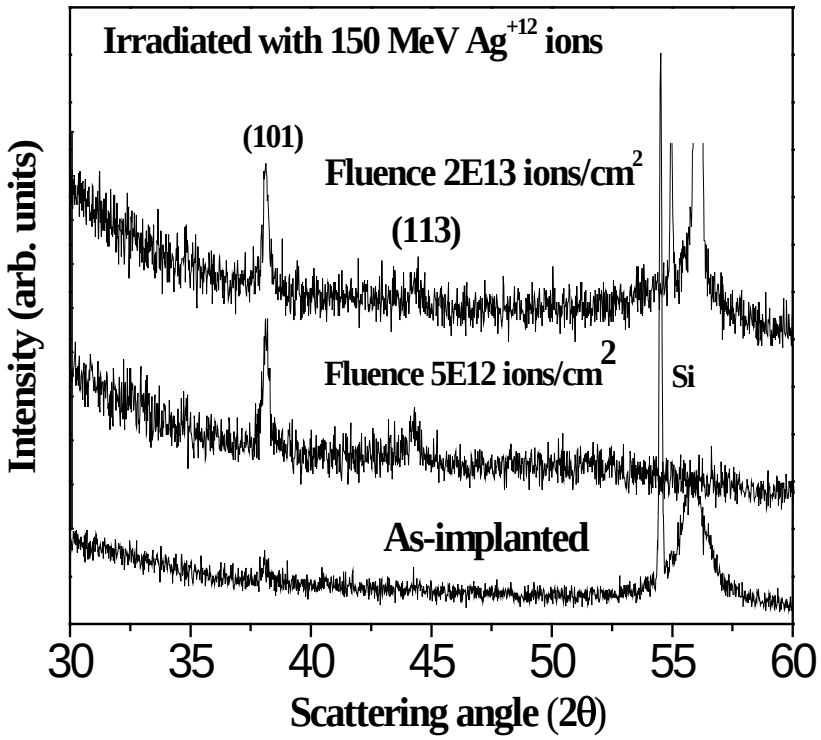

Fig.5.2: GIXRD of irradiated Ge implanted SiO_2 films.

X-ray diffraction spectra of pristine and 100 MeV Au^{+8} ions irradiated Ge implanted Si with a dose of 5×10^{16} ions/cm^2 sample are shown in Fig. 5.3. These Ge implanted Si sample was irradiated at fixed fluence of $3x10^{13}$ ions/cm^2. In Ge implanted Si due to high fluence the as-implanted sample shows the amorphous nature whereas Au ion irradiation results in crystallization as visible from the Ge (311) at 53.74^0 and Si (311) at 55.84^0 peaks in the spectra. This is comparable with the results obtained by implantation of Ge into thermally grown SiO_2 layer [24].

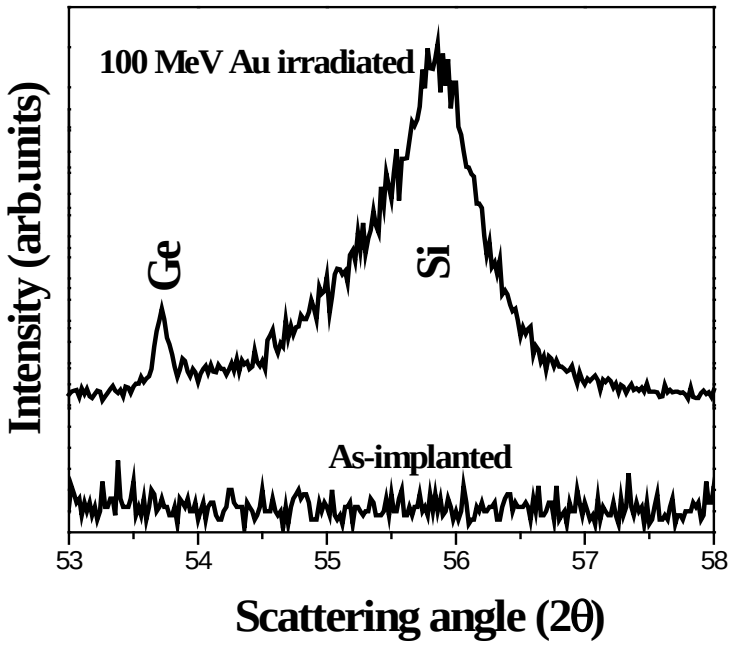

Fig. 5.3: GIXRD of Ge implanted Si as-implanted and 100 MeV irradiated.

The appearance of Si peak would indicate the crystallized top layer. The large width of the Si peak would indicate the existence of defects in the layer. The Raman spectrum of the Au ion irradiated sample is shown in Fig.5.4. Here the appearance of Ge mode along with Si-Ge mode indicates the re-crystallization of the amorphized layer. Similar results have been reported for the annealed sample implanted with Ge ions [25]. The mode around 150 cm^{-1} may be attributed to residual damages in the top Si layer.

Surface morphology of the irradiated implanted film has been studied by AFM. The AFM image after Au ion irradiation as shown in Fig. 5.5 that indicates a smooth surface with an rms roughness of about 0.3 nm. This shows that the roughness of the sample is not increased greatly by ion irradiation.

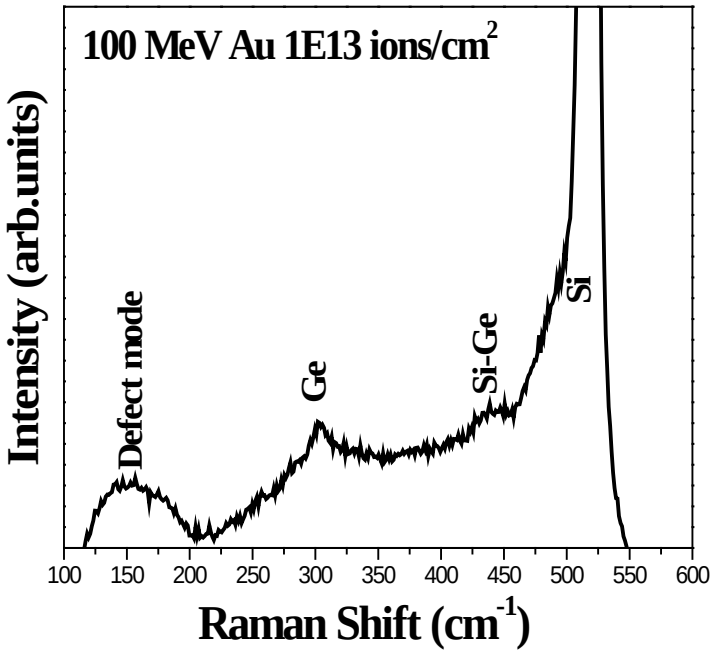

Fig. 5.4: Raman spectrum of irradiated Ge implanted Si sample with Au ions.

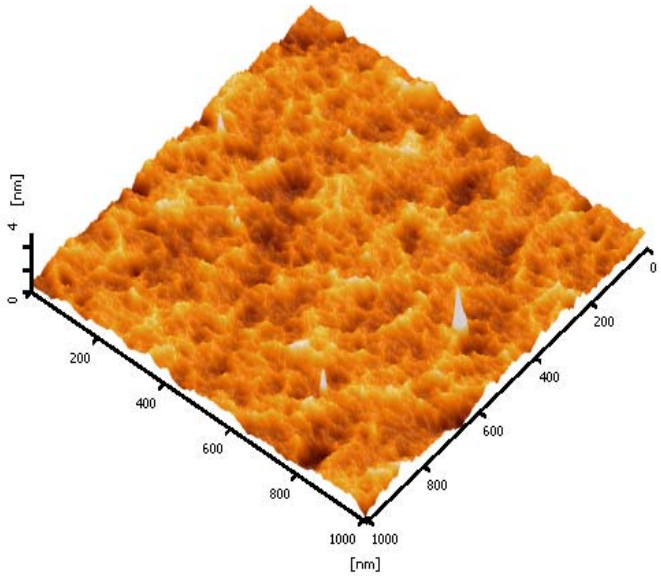

Fig. 5.5: AFM image of irradiated Ge implanted Si sample with Au ions.

One can explain the basic mechanism of re-crystallization and formation of nanocrystals in these samples, under ion-irradiation with the help of thermal spike model [26]. When the swift heavy ion passes through the matter, it loses energy via electronic energy loss *(Se)* and nuclear energy loss *(Sn)*. The swift energy transfer makes the system particularly excited and the region around the ion track gets suddenly heated to a very high temperature and the material inside the ion track

transforms to the molten state for a short duration. Thus a large amount of energy is transferred to the target and leads to an increase of the lattice temperature above its melting point along the ion path. Eventually, the energy is transferred to the target lattice via electron–phonon coupling. The resulting modification of silica matrix creates tracks in a cylindrical region. The passage of swift heavy ions deposits the electronic energy (*Se)* of the order of 17 keV/nm in these samples which may help to release the strain between the grains in the films and results in crystallization. The diffusion of Ge atoms in these track regions results in agglomeration leading to formation of Ge NC's. It has been observed that the size of these Ge NC's increases with an increase in ion fluence. It may be possible to tune the size and properties of Ge NC's by choosing the appropriate irradiation energy and ion fluence.

5.4 Conclusions

In summary, the effects of SHI irradiation on Ge implanted into SiO_2 and Si matrices have been studied. The results show that swift heavy ion irradiation leads to crystallization of these films. XRD reveals that the average diameter of the crystallites increases with irradiation ion fluence. Due to high fluence the as-implanted sample shows amorphous nature whereas ion irradiation results in recrystallization, which is evident from the Ge peak in Raman and XRD. The increase of size of NC's with ion fluence takes place due to increase of diffusivity and resulting agglomeration of Ge atoms and small nanocrystals. In the Raman spectrum of the Au ion irradiated sample, the appearance of Ge mode along with Si-Ge mode indicates the recrystallization of the amorphized layer. The basic mechanism of crystallization has been discussed.

5.5 References

1. K A Littau , P J Szajowski, A J Muller and L E Brus J. Phys. Chem. 97 (1993) 1224
2. J P Wilcoxon and G A Samara, Appl. Phys. Lett. 74 (1999) 3164
3. Y Maeda, N Tsukamoto, Y Yazawa, Y Kanemitsu and Y Masumoto, Appl. Phys. Lett. 59 (1991) 3168
4. D C Paine, C Caragianics, T Shigesato and T Ishikawa, Appl. Phys. Lett. 62 (1993) 2842
5. P Bettotti, M Cazzanelli, L Dal Negro, B Danese, Z Gaburro, C J Oton, G V Prakash and L Pavesi, J. Phys.: Condens. Matter 14 (2002) 8253
6. M She and T King, J. IEEE Trans. Electron Dev. 50 (2003) 1934
7. C Bostedt , T Van Buuren , J M Plitzko, T Moller and L J Terminello J. Phys.: Condens. Matter 15 (2003) 1017
8. T Oku , T Nakayama, M Kuno, Y Nozue, L R Wallenberg, K Niihara and K Suganuma Mater. Sci. Eng. B 74 (2000) 242
9. F Gao, M A Green, G Conibeer, E-C Cho, Y Huang, I Pere-Wurfl and C Flynn, Nanotechnology 19 (2008) 455611
10. K Das, M L N Goswami, A Dhar, B K Mathur and S K Ray Nanotechnology 18 (2007) 175301
11. C W Lin, S Y Lin, S C Lee and C T Chia, J. Appl. Phys. 91 (2002) 1525
12. A K Das, J Kamila and B N Dev, Appl. Phys. Lett. 77 (2002) 951
13. S T Ngiam, K F Jensen and K D Kolenbrander J. Appl. Phys. 76 (1994) 8201
14. Y Zhu, C L Yuan and P P Ong J. Appl. Phys. 93 (2003) 6029
15. H Q Yang, X Yao, X J Wang, S H Xie, Y Fang, S X Liu and X X Gu J. Phys. Chem. B 107 (2003) 13319
16. S. Guha, M. D. Pace, D. N. Dunn, and I. L. Singer, Appl. Phys. Lett. 70 (1997) 1207.
17. J. Von Borany, R. Grotzschel, K. H. Heinig, A. Markwitz, W. Matz, B. Schmidt, and W. Skorupa, Appl. Phys. Lett. 71 (1997) 3215.
18. T. Shimizu-Iwayama, S. Nakao, K. Saitoh, Appl. Phys. Lett. 65 (1994) 1814.

19. Y. Kanemitsu, N. Shimizu, T. Komoda, P.L. Hemment, B.J. Sealy, Phys. Rev. B 54 (1996) R14329.
20. C.W. White, J.D. Budai, S.P. Withrow, J.G. Zhu, E. Sonder, R.A. Zuhr, A. Meldrum, D.M. Hembree Jr., D.O. Henderson, S. Prawer, Nucl. Instr. Meth. Phys. Res. B 141 (1998) 228.
21. Y. Kanemitsu, H. Tanaka, T. Kushida, K.S. Min, H.A. Atwater, J. Appl. Phys. 86 (1999) 1762.
22. S. Okamoto, Y. Kanemitsu, K.S. Min, H.A. Atwater, Appl. Phys. Lett. 73 (1998) 1829.
23. Y. K. Mishra, D. K. Avasthi, P. K. Kulriya, F. Singh, D. Kabiraj, and A. Tripathi, J C Pivin, I. S. Bayer and A. Biswas, Appl. Phys. Lett 90 (2007) 073110.
24. P.K. Giri, R. Kesavamoorthy, S. Bhattacharya, B.K. Panigrahi, K.G.M. Nair. Materials Science and Engineering B 128 (2006) 201.
25. P K Giri, R Keasavamoorthy, B K Panigrahi and K G M Nair Nucl. Inst. and Meth. B 244 (2006) 56.
26. M. Toulemonde, C. Dufour, E. Paumier, Phys. Rev. B 46 (1992) 14362

Chapter - VI

Conclusions and Outlook

6.1 Synthesis of Ge nanocrystals by Atom Beam Sputtering

In this thesis, the work on synthesis of Ge nanocrystals using various methods has been reported. Ge+SiO_2 composite films were prepared by ABS method where small pieces of high purity Ge were placed on a SiO_2 target and co-sputtered by an Argon atom source. Thin films were deposited on Si substrates. Ge and SiO_2 composite films with various Ge compositions were prepared by co-sputtering of Ge and silica using 1.5 keV Ar atoms. The Ar atom source was mounted at an angle of 45^0 facing the sputtering target inside a vacuum chamber. The effects of Ge composition and annealing temperature have been studied and discussed in detail.

On the other hand, these composite films were also annealed at various temperatures using Rapid Thermal annealing (RTA). The high energy irradiations were also carried out using the accelerator facility at IUAC, New Delhi. We have used various energies and fluencies to see the effects of electronic energy loss and fluencies dependence on nanocrystal synthesis. To avoid heating of samples a low beam current (0.5 – 2 pnA) was maintained during ion irradiation. The samples were oriented at an angle of $5 – 7^o$ with respect to the beam axis to minimize channeling. These films were characterized by RBS, XRD, TEM, Raman, FTIR and AFM. Advantages of ABS over other techniques have been discussed.

Ge nanocrystals embedded in SiO_2 matrix were prepared by ABS method followed by RTA [1]. The as-deposited films were rapid thermally annealed at the temperatures 700^0 and 800^0C in nitrogen ambience. The structure of the films was evaluated by using XRD and Raman spectroscopy. XRD results reveal that as-deposited films are amorphous in nature whereas annealed samples show crystalline nature. Raman scattering spectra showed a peak of Ge–Ge vibrational mode shifted downwards to

297cm^{-1}, presumably caused by quantum confinement of phonons in the Ge nanocrystals. Rutherford backscattering spectrometry has been used to measure the thickness and Ge composition of the composite films. Size variation of Ge nanocrystals with annealing temperature has been discussed. Experimental results of thermally annealed and rapid thermally annealed thin film samples have been compared and discussed. Advantages of ABS over other methods are highlighted.

In the second part, the as-deposited films were annealed at the temperatures 700 and 800^0 C under Ar+H_2 atmosphere [2]. RBS was used to quantify the composition of Ge in SiO_2 matrix of the composite thin films. The formation of Ge nanoparticles were observed from the Ge mode in the Raman spectra as a function of annealing, appearance of Ge (311) peaks in the X-ray and the Ge vibrational mode in the FTIR spectra.

Finally, we have prepared Ge nanoparticles embedded in SiO_2 matrix by ABS of Ge+SiO_2 on Si substrate [3]. The as-deposited films were irradiated with various energies at fixed fluence. The pristine and irradiated samples were characterized by Raman, XRD and AFM. RBS was used to quantify the concentration of Ge in the SiO_2 matrix and the film thickness. Raman studies of the films indicate the formation of Ge crystallites as a result of swift heavy ion irradiation (SHI). The basic mechanism for re-crystallization induced by SHI in these films has been discussed.

A comparative look at the results presented here indicates that RTA is better than normal furnace annealing for nanocrystal synthesis. We have observed better crystallization due RTA effects which is evident from XRD and Raman. Quantum confinement effects were also more prominent in RTA results when compared to furnace annealing ones. GeO_2 formation is also observed besides Ge nanocrystals in furnace annealing sample which is clear from XRD spectra. Currently, swift heavy ions are being used to tune the size and shape of the nanocrystals which were obtained by the annealing ones. It is very useful to alter the properties of nanomaterials by varying the ion beam parameters.

6.2 Synthesis of Ge nanocrystals by RF magnetron sputtering

Ge nanocrystals embedded in Silicon oxide matrix have been synthesized on Si substrate by co-sputtering of SiO_2 and Ge using RF magnetron sputtering technique. The as-deposited films were subjected to microwave annealing at 800 and 900^0C [4]. As deposited film shows amorphous nature whereas annealed films show crystalline nature with three peaks of Ge (1 1 1), (2 2 0) and (3 1 1), which indicates the formation of nc-Ge. It is also observed that the average size of nc-Ge increases with the increase of annealing temperature. The crystallite size was calculated by using Scherrer formula [5] as well as with Williamson-Hall (WH) method [6-8]. Raman scattering spectra showed a peak of Ge-Ge vibrational mode around 299 cm^{-1}, which was caused by quantum confinement of phonons in the Ge nanocrystals. Surface morphology of the as-deposited and annealed samples has been studied using AFM. Variation of the nanocrystal size with annealing temperature has been discussed. Advantages of microwave annealing are explained in detail.

Similarly, the as-deposited samples were also irradiated with 150 MeV Ag^{+12} ions at a fixed fluence of $3x10^{13}$ ions/cm^2. The as-deposited sample shows a broad Raman peak centered at 270 cm^{-1} which corresponds to amorphous Ge. The appearance of peak around 290 cm^{-1} of the irradiated sample indicates the crystallization of the film [9].

The broad feature in the irradiated Raman spectrum along with the peak at ~290 cm^{-1} indicates partial amorphous nature of the film. It is known that mechanical compressions can lead to change in the frequency of Ge–Ge bond vibrations. Due to the 4% mismatch in the lattice constants of Ge and Si, the shift for transverse optical modes can reach 10 cm^{-1}. The average size of the Ge nanocrystals was estimated from the TEM image. The surface topography of these films was investigated with AFM. It was found that the as-deposited films have a less surface roughness than the irradiated ones, the roughness of films was increased and a grain-like morphology was exhibited. Results, mechanism of crystallization and formation of nanocrystals in these samples under ion irradiation are explained with the help of thermal spike model [10] and works of Meftah et al. [11] and Toulemonde et al. [12].

6.3 Swift heavy ion irradiation effects on Ge implanted SiO_2/Si films

Ge nanocrystals embedded in SiO_2 matrix have been synthesized by swift heavy ion irradiation of Ge implanted SiO_2 films. In the present study, 400 keV Ge^+ ions were implanted into SiO_2 films at dose of $3x10^{16}$ ions/cm^2 at room temperature. The as-deposited films were irradiated with 150 MeV Ag^{+12} ions with various fluences. Similarly, 400 keV Ge^+ ions implanted into Silicon substrate at higher fluence at 573K (300^0C) have been irradiated with 100 MeV Au^{8+} ions at room temperature. The RBS spectrum indicates the presence of Si, O, Ge in the sample. The composition of Ge is estimated from the RBS spectrum. X-ray diffraction spectra of 100 MeV Au^{+8} ions irradiated Ge implanted Si with a dose of 5×10^{16} ions/cm^2 sample clearly indicates the formation of Ge nanoparticles. In Ge implanted Si due to high fluence, the as-implanted sample shows the amorphous nature where as Au ion irradiation results in crystallization as visible from the Ge (311) and Si peaks in the spectra [13]. This is comparable with the results obtained by implantation of Ge into thermally grown SiO_2 layer. The appearance of Si peak would indicate the crystallized top layer. The large width of the Si peak would indicate existence of defects in the layer. The Raman spectrum of the Au ion irradiated sample shows the Ge mode along with SiGe mode, which indicates the re-crystallization of the amorphized layer. Similar results have been reported for the annealed sample implanted with Ge ions. The mode around 150 cm^{-1} may be attributed to residual damages in the top Si layer. The irradiation results were compared with the ones obtained by thermal annealing.

6.4 Future prospects

The present study throws light on the synthesis of Ge nanocrystals by different methods. In this direction several issues need further experimental and theoretical investigations. Additional work is also needed to make complete **comparative study** of all these methods that were used to prepare Ge nanocrystals.

Ge nanocrystals are very useful in memory devices and infrared detectors. The charge storage property of semiconductor nanocrystals embedded in a silicon oxide matrix is currently under extensive investigation due to their potential applications in future nonvolatile memory applications. Preliminary application related experiments are

being initiated and those are in progress. The work has also been started on GeO_2 [14] nanocrystals due to their applications in various fields.

We would like to study the effects of high temperature Ge implantation into SiO_2 matrix. Ge ions with different doses with different energies will be implanted into SiO_2 and subsequently irradiated with swift heavy ions. Formation of Ge nanocrystals as a result ion beam irradiation will studied systematically. Eventually, high temperature annealing effects on irradiated samples will be investigated and characterized by various techniques. We also plan to make memory devices using MOS structure. We will vary the input parameters and increase the efficiency. This work is in progress.

Modification of nanocrystals by ion beams attracted great interest due to tunability of properties of nanocrystals by changing their shape and size. We plan to irradiate the nanocrystalline Ge embedded SiO_2 films using swift heavy ions with various energies and fluencies and tune the bandgap and optical, structural properties of the nanocrystals for a variety of applications.

We also plan to extend this work to Ge and GeO_2 nanowires due to their applications in diverse fields. RTA and Microwave annealing effects on these samples will be studied. Results will be compared with the ones obtained from other techniques.

6.5 References

1. **N Srinivasa Rao**, A P Pathak, N Sathish, G Devaraju, V Saikiran, P K Kulriya, D C Agarwal, G Sai Saravanan and D K Avasthi Solid State Communications 150 (2010) 2122
2. **N. Srinivasa Rao**, S. Dhamodaran, A.P. Pathak, P.K. Kulriya, Y.K.Mishra, F. Singh, D. Kabiraj, J.C. Pivin, D.K. Avasthi. Nucl. Inst. Meth B 264 (2007) 249**.**
3. **N Srinivasa Rao**, S Dhamodaran, A P Pathak, D Kabiraj, S A Khan, B K Panigrahi, K G M Nair, B Sundaravel, J C Pivin and D K Avasthi**,**

Radiation Effects and Defects in Solids**.** Vol. 164, Nos. 7–8, July 2009, 452.

4. **N Srinivasa Rao**, A P Pathak, G Devaraju and V Saikiran (Communicated)
5. B. D. Cullity, Elements of X-ray Diffraction, 2nd. Ed., Addison-Wesley, reading, MA, p.102. (1978)
6. G K Williamson and W H Hall Acta Metall. **1 (**1953) 22
7. A J C Wilson, X-ray Optics (Methuen, London) 1949.
8. A.R. Stokes and A.J.C. Wilson. Proc. Phys. Soc. London **56** (1944) 174
9. **N Srinivasa Rao**, A P Pathak, et al (Accepted for AIP proceedings).
10. M Toulemonde, C. Dufour, E. Paumier, Phys. Rev. B 46 (1992) 14362
11. A Meftah, F. Brisard, M. Costantini et al., Phys. Rev. B **49** (1994) 12457.
12. M. Toulemonde, J.M. Costantini, Ch. Dufour et al., Nucl. Instrum. Methods B 116 (1996) 37.
13. **N Srinivasa Rao**, A P Pathak, N Sathish, G Devaraju, S A Khan, K Saravanan, B K Panigrahi, K G M Nair, and D K Avasthi. Nucl. Inst. Meth B 268 (2010) 1741.
14. V Saikiran, **N Srinivasa Rao**, G Devaraju and A P Pathak (Accepted for AIP proceedings).